University of Birmingham

Randeep Riyat

Pauli-paramagnetic effects in unconventional superconductors

May 2017

PAULI-PARAMAGNETIC EFFECTS IN UNCONVENTIONAL SUPERCONDUCTORS

by

RANDEEP RIYAT

A thesis submitted to
The University of Birmingham
for the degree of
DOCTOR OF PHILOSOPHY

School of Physics & Astronomy
College of Engineering and Physical Sciences
The University of Birmingham
May 2017

Abstract

Paramagnetism describes a type of magnetism whereby a material is weakly attracted by an external magnetic field. The material forms induced magnetic fields in the direction of the external magnetic field. Pauli-paramagnetism is a weak form of paramagnetism. It arises in a conductor when a magnetic field is applied and its conduction band is split into a spin-up and a spin-down band due to the differences in magnetic potential energy for spin-up and spin-down electrons. As the Fermi level must be the same for each band, there is inevitably a surplus of the type of spin in the band that shifted downwards. In a regular (non-Pauli paramagnetic) superconductor, the superconductivity is destroyed due to the orbital supercurrents. However, in a Pauli-paramagnetic superconductor, the normal state is induced by the coupling of the magnetic field to the spin of the electrons (i.e. in materials with significant Pauli paramagnetism). The effects of the Pauli-paramagnetism are visible in the magnetic vortices of the superconductor as this is where the electron pairs have been "broken up", and the nature of these vortices can be probed by small-angle neutron scattering.

In this thesis we present studies of the vortex lattice in $YBa_2Cu_3O_7$ (YBCO), which was the first known superconductor to have a superconducting transition temperature above the boiling point of liquid nitrogen (77 K). YBCO was discovered (Wu *et al.*, 1987) shortly after the discovery of the cuprate family of superconductors (Bednorz & Muller, 1986). The cuprates consist of copper-oxide (CuO_2) layers and have been intensively studied for over 30 years. This study looks at the low-temperature structure and form factor of the vortex lattice at the highest fields ever used to study the vortex lattice in a superconductor by neutrons to date. Our results indicate that Pauli-paramagnetic effects become increasingly important as the applied field is increased up to the maximum available field of 25 T.

We also present studies of the vortex lattice in the heavy fermion compound $CeCu_2Si_2$ which was the first so-called “unconventional” superconductor to be discovered. $CeCu_2Si_2$ was also the first heavy fermion compound to exhibit superconducting properties (Steglich *et al.*, 1979), however even after many years of being heavily studied; the mechanism responsible for its superconductivity is still under debate. This study provides the first direct evidence of Pauli-paramagnetic effects in this system, and contributes to the elucidation of the nature of the superconductivity in this material.

This thesis demonstrates the importance of considering Pauli-paramagnetic effects when trying to understand the vortex lattice behaviour of an unconventional superconductor.

Acknowledgements

Firstly, I would like to thank Elizabeth Blackburn for her excellent supervision throughout my PhD. She has always provided me with clear advice when I needed it, but I especially appreciate that I was given the freedom to decide on the direction of my research in many respects. Secondly, I would like to thank Ted Forgan for always being thorough in answering my many questions, and also for his extensive catalogue of (mostly amusing) jokes which proved to be a great source of motivation at 1 a.m. on the beamline!

I have worked with many scientists who have been imperative to my own growth as a physicist. These include Alistair Cameron, Jon White, Steve Kuhn, Stephen Pollard, Philippa Jefferies, Toshi Loew, Hazuki Furukawa and Natalia Parzyk. I also had the pleasure of working alongside many instrument scientists at the large facilities where I carried out experiments. These include Bob Cubitt, Charles Dewhurst, Jorge Gavilano, Oleksandr Prokhnenko, Maciej Bartkowiak, Wolf-Dieter Stein, Sebastian Muhlbauer, Andre Heinemann, Tommy Reimann, Adrian Hillier, Didier Wermeille and Steve Collins. None of the experiments that make up this thesis would have been possible without the high quality samples provided by Andreas Erb and Oliver Stockert. I would also like to thank Jon Perrins for making the sample holders, Gary for his help on various technical matters and Michael for providing us with liquid helium for the SQUID and 17 T magnet.

During my time in Birmingham, I was very fortunate to work with other members of the Quantum Matter group. I would like to thank (in no particular order): Lingjia for being a brilliant tour guide in China and also for introducing me to the NBA, Alex for always knowing the best restaurant nearby any neutron source in Europe, Bindu for telling me to start writing my thesis as early as possible and Louis for inadvertently serving as a reminder that some people are rather odd. I would also like to thank Erik, Ellen, Arvid and Filippo for many interesting discussions.

Finally, I cannot express my gratitude enough for my family and the support they have provided throughout my education. I especially thank my parents, and will never forget what they have done for me.

CONTENTS

LIST OF FIGURES

Chapter 1

Superconductivity

This chapter is written with the intention of giving a brief overview of the relevant parts of the theory of superconductivity required to interpret the results arising from this thesis. It begins with a concise outline of the London equations followed by a more in-depth description of Ginzburg-Landau theory and how this theory can be used to determine the characteristic lengths of superconductors. An overview is given of the BCS theory of superconductivity prior to explaining the role of the vortex lattice in a superconductor. Finally, an examination of Pauli-paramagnetic effects is given to better understand its role in the superconducting compounds studied in later chapters of this thesis. Most of this chapter follows the treatment by Tinkham [97] unless otherwise stated.

Superconductivity was first observed by Heike Kamerlingh Onnes in 1911, [71], when the electrical resistance of mercury completely disappeared below a critical temperature T_C. It has since been observed in many other materials. Another property of superconductors, discovered later by Meissner and Ochsenfeld [68], is the expulsion of all internal magnetic fields below a critical field H_C. Superconductors can fall into two categories depending on the behaviour of their magnetisation with applied magnetic field. Type-I superconductors exhibit the so-called Meissner effect whereby the magnetisation $\mathbf{M}$ = -H below H_C and $\mathbf{M} = 0$ above H_C. Type-II superconductors have both a lower and an upper critical field, H_{C1} and H_{C2}, respectively. For fields below the lower critical field H_{C1}, the type-II superconductor is in the Meissner state, however for $H_{C1} < H < H_{C2}$ the

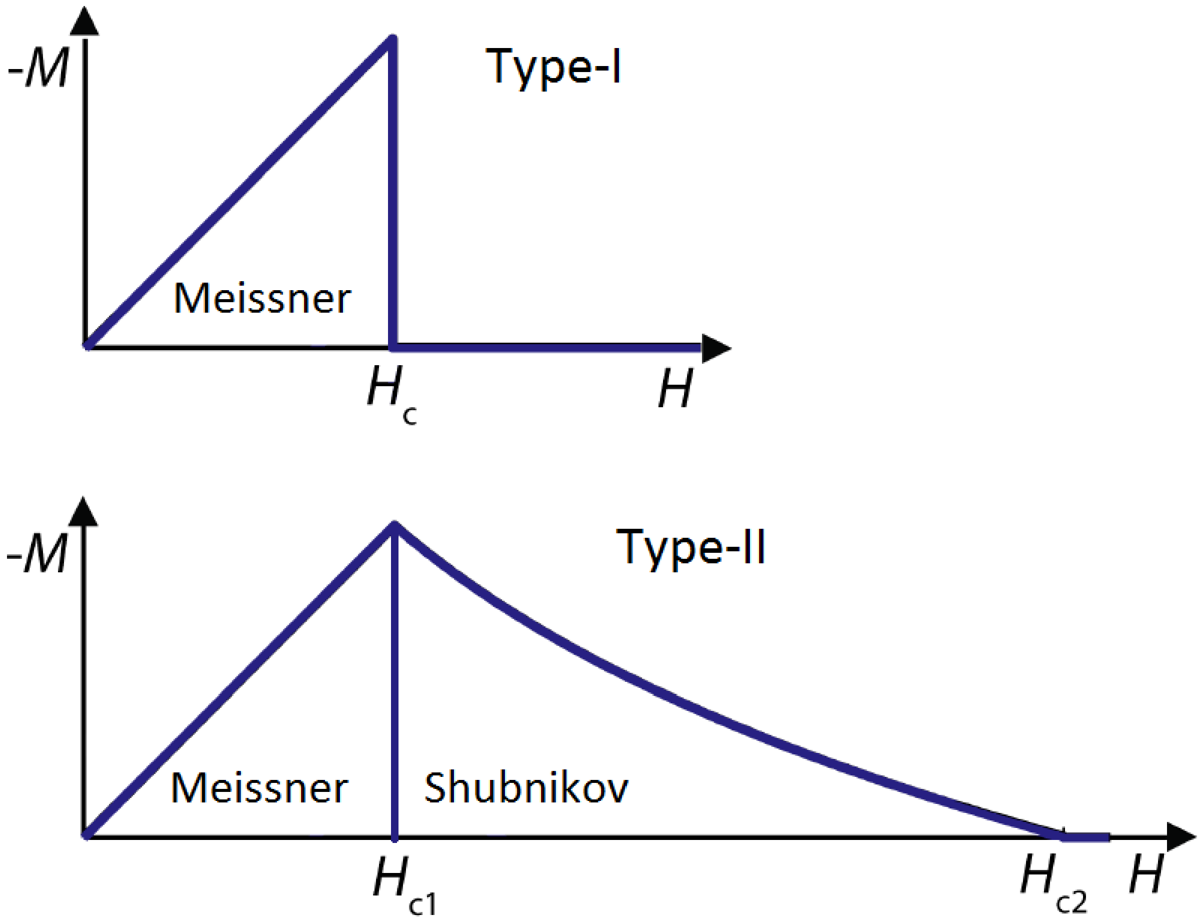

Figure 1.1: The magnetisation, **M**, vs applied magnetic field, **H**, for type-I and type-II superconductors. Figure adapted from [25].

superconductor is in the “Shubnikov” phase whereby magnetic flux does start to enter the superconductor and **M** tends to zero as H_{C2} is approached, as shown in Fig 1.1. The critical fields vary as a function of the temperature.

1.1 The London Equations

The brothers F. London and H. London developed the first theory [66] which could account for the Meissner effect. They proposed two equations:

$$\mathbf{E} = \frac{\delta}{\delta t}(\Lambda \mathbf{J}_s) \tag{1.1}$$

$$\mathbf{B} = -c \text{ curl } (\Lambda \mathbf{J}_s) \tag{1.2}$$

where

$$\Lambda = \frac{4\pi\lambda^2}{c^2} = \frac{m}{n_s e^2}. \tag{1.3}$$

Here Λ is a phenomenological parameter associated with the number density of superconducting electrons, $\mathbf{J_s}$ is the electrical current density inside a superconductor, n_s is the number density of superconducting electrons, m is the electron mass, e is the electron charge, c is the speed of light in a vacuum, and λ is the London penetration depth,

$$\lambda = \sqrt{\frac{mc^2}{4\pi n_s e^2}}. \tag{1.4}$$

Equation 1.1 describes perfect conductivity since any electric field causes the superconducting electrons to accelerate rather than maintain their velocity against resistance as they would in a regular conductor. Equation 1.2 can be combined with the Maxwell equation curl $\mathbf{B} = 4\pi\mathbf{J}/c$ to give

$$\nabla^2 \mathbf{B} = \frac{\mathbf{B}}{\boldsymbol{\lambda^2}} \tag{1.5}$$

which describes the exponential internal screening of a magnetic field in a sample with penetration depth λ; the Meissner effect. The penetration depth is temperature dependent and its dependence with temperature can be described by

$$\lambda(T) \approx \lambda(0)[1 - (T/T_C)^4]^{-1/2}. \tag{1.6}$$

A quantum approach can also be taken which makes use of the vector potential $\mathbf{A}$. Following the treatment by Tinkham [97], taking the canonical momentum $\mathbf{p} = (m\mathbf{v} + e\mathbf{A}/c)$

(= 0 in the absence of an applied field) leads us to the following relation

$$\langle \mathbf{v} \rangle = \frac{-e\mathbf{A}}{mc} \tag{1.7}$$

which describes the local average velocity in the presence of the field. Assuming that the wavefunction of the superconducting electrons retains its property that in the ground state $\langle \mathbf{p} \rangle = 0$, this relationship holds. It follows that

$$\mathbf{J_s} = n_s e \langle \mathbf{v} \rangle = \frac{-n_s e^2 \mathbf{A}}{mc} \tag{1.8}$$

which is equivalent to equation 1.1 by taking the time derivative of both sides and equivalent to equation 1.2 by taking the curl of both sides. From this we can obtain the following term to describe the penetration depth:

$$\lambda = \sqrt{\frac{mc^2}{4\pi n_s e^2}}. \tag{1.9}$$

1.2 The London Vortex

In the aforementioned type-II superconductors, an applied magnetic field can enter the superconductor in the form of magnetic vortices. The London equation can be used to provide a brief mathematical description of the superconducting vortex. The cylindrical vortex will be in the normal state and has a radius approximately equal to a characteristic length, ξ_0, known as the coherence length. The core has a finite magnetic field, B_0 (the magnetic flux is in fact quantized, resulting in $h/2e$ of flux per vortex line). This finite magnetic field inside the vortex core, where the radius is less than the coherence length, then decreases logarithmically between $\xi_0 <$ r $< \lambda$ and then exponentially decreases to zero outside of the vortex on a length scale of order λ.

1.3 Ginzburg-Landau Theory

The Ginzburg-Landau (GL) theory is useful because it is able to describe systems in which n_s varies spatially and also deals with the non-linear response to fields that are strong enough to cause n_s to change. GL theory is based on a series expansion of $|\psi|^2$, so it is limited to regions close to the critical temperature T_C where this quantity is small. I have followed the treatment by Tinkham [97] and Eskildsen [31] in this section. GL theory reduces to the London equations if n_s is assumed to be constant in space.

GL theory argues that the free energy, f_s, of a superconductor can be expressed in terms of a complex order parameter ψ, which is non-zero in the superconducting state. This gives the free energy of the superconducting state as

$$f_s = f_{n0} + \frac{\hbar^2}{4m}|(\nabla - \frac{2ie}{\hbar c}\mathbf{A})|^2 + \alpha|\psi|^2 + \frac{\beta}{2}|\psi|^4 + \frac{\mathbf{B}^2}{8\pi} \tag{1.10}$$

where f_{n0} is the free energy in the normal phase, the α and β terms, whereby α and β are coefficients, are the series expansion in $|\psi|\ ^2$, $\mathbf{A}$ is the magnetic vector potential, $\mathbf{B}$ is the magnetic field, m is the effective mass of an electron and e is the charge of an electron. The mass and charge are double the single electron values as ψ describes a condensate of electron pairs (known as Cooper pairs). By minimising f_s - f_n we find $|\psi|^2$ = ψ^2_∞ = -$\frac{\alpha}{\beta}$ in the absence of magnetic field. ψ^2_∞ is used because ψ approaches this value infinitely deep in the superconductor. Using this value of ψ, one finds f_s - f_n = $\frac{-H_C^2}{8\pi}$ = $\frac{-\alpha^2}{2\beta}$. The superconducting transition occurs as α changes from positive to negative, since β has to be positive if the theory is to be useful, otherwise the lowest free energy would occur for arbitrarily large values of $|\psi|^2$, where expansion is inadequate. The temperature dependence of α is linear in the lowest order approximation,

$$\alpha \propto \left(\frac{T}{T_c} - 1\right). \tag{1.11}$$

The Meissner effect, whereby the flux is expelled from the bulk of the material, may be described by the fact that the superconducting state is thermodynamically stable as it has a lower energy than the normal state. The difference in energy between the two states in the absence of field defines the thermodynamic critical field, $H_c^2 = 4\pi\frac{\alpha^2}{\beta}$, which was mentioned above in terms of f_s and f_n.

We can now also consider the final term in equation 1.10, i.e. the term dealing with fields and gradients. If we write $\psi = |\psi|e^{i\phi}$, it is:

$$\frac{1}{4m}\left[\hbar^2(\nabla|\psi|)^2 + \left(\hbar\nabla\phi - \frac{2e\mathbf{A}}{c}\right)^2 |\psi|^2\right]. \tag{1.12}$$

The first term is for the extra energy associated with gradients in the magnitude of the order parameter, i.e. a domain wall, and the second term is for the kinetic energy associated with the supercurrents.

1.3.1 Ginzburg-Landau Equations

The following three equations are known as the GL equations which are derived from equation 1.10 by minimising the free energy with respect to variations in the order parameter, ψ, and the magnetic vector potential, $\mathbf{A}$.

$$\frac{1}{4m}\left(-i\hbar\nabla - \frac{2e}{c}\mathbf{A}\right)^2 \psi + \alpha\psi + \beta|\psi|^2\psi = 0 \tag{1.13}$$

and

$$\nabla \times \mathbf{B} = \frac{4\pi}{c}\mathbf{J} \tag{1.14}$$

where $\mathbf{J}$ is the superconducting screening current given by the expression

$$\mathbf{J} = -\frac{ie\hbar}{2m}\left(\psi^*\nabla\psi - \psi\nabla\psi^*\right) - \frac{2e^2}{mc}|\psi|^2\mathbf{A}. \tag{1.15}$$

1.3.2 Characteristic Lengths of Superconductors

The two characteristic lengths which describe the superconducting state are the penetration depth λ and the coherence length ξ. The values of these two characteristic lengths can be extracted from the GL equations. The coherence length corresponds to the size of the non-superconducting vortex core that the super-current circulates around in Type-II superconductors. To help understand equation 1.10, we should consider the simplified case where no fields are present, $\mathbf{A} = 0$, and take ψ to be real since the differential equation 1.10 has only real coefficients. By normalising ψ to the bulk value ($\overline{\psi} = \psi/\psi_\infty$) one gets

$$\frac{\hbar^2}{4m\alpha}\nabla^2\overline{\psi} - \overline{\psi} + \overline{\psi}^3 = 0. \tag{1.16}$$

From this equation, the coherence length is defined as

$$\xi^2 = \frac{\hbar^2}{4m|\alpha|}. \tag{1.17}$$

The penetration depth is derived from equations 1.12 and 1.13 in a weak magnetic field so that we can take ψ as the bulk value ψ_∞ which gives

$$\nabla^2\mathbf{B} = \frac{1}{\lambda^2}\mathbf{B} \tag{1.18}$$

which gives

$$\lambda^2 = \frac{mc^2\beta}{8\pi e^2|\alpha|}. \tag{1.19}$$

The penetration depth describes how far a magnetic field can penetrate into the superconducting state before being screened by superconducting currents. The temperature dependence of the penetration depth is given by $\lambda^2 \propto$ (1 - T/T$_c$)$^{-1}$. If $\frac{|\alpha|}{\beta}$ is replaced by $n_s/2$, which is assumed to be spatially constant, λ becomes the London penetration depth given by

$$\lambda_L^2 = \frac{mc^2}{4\pi n_s e^2}. \tag{1.20}$$

The GL parameter κ is defined as the ratio between the penetration depth and the coherence length,

$$\kappa = \frac{\lambda}{\xi}, \tag{1.21}$$

which is not temperature dependent. Landau proposed that type-I superconductors are those with $0 < \kappa < \frac{1}{\sqrt{2}}$ and type-II superconductors are those with $\kappa > \frac{1}{\sqrt{2}}$.

1.3.3 Domain Wall Energy

The domain wall energy is defined as the extra free energy cost of imposing a domain wall, over that of the state without a domain wall. As long as the normal and superconducting phases have the same free energy, the system's total free energy will be unaffected by translations of the wall. In figure 1.2, the variations of ψ and of $h(x)$ in the domain wall are shown, contrasting the type-I and the type-II scenarios. It can be seen that for the type-I scenario the surface energy is positive as there is a thickness (approximately equal to the difference between the penetration depth and the coherence length) from which the field is contributing to the positive diamagnetic energy rather than the full condensation energy associated with ψ_∞. The opposite is true of the type-II scenario. This argument can also be made quantitatively using Ginzburg-Landau theory.

γ is the energy associated with the interface between the normal and superconducting states (NS interface). It determines the response of the material to a magnetic field equal to H_C. As $\mathbf{H} = \mathbf{B}$ - $4\pi\mathbf{M}$ is constant, the thermodynamic potential that needs to be used for the calculation is the Gibbs free energy - this differs from the Helmholtz free energy by a factor of -$\mathbf{H}.\mathbf{B}/4\pi$.

$$\gamma = \int dV \left(f_{sH_C} - \frac{H_C B}{4\pi} - f_{nH_C} + \frac{H_C^2}{4\pi} \right) \tag{1.22}$$

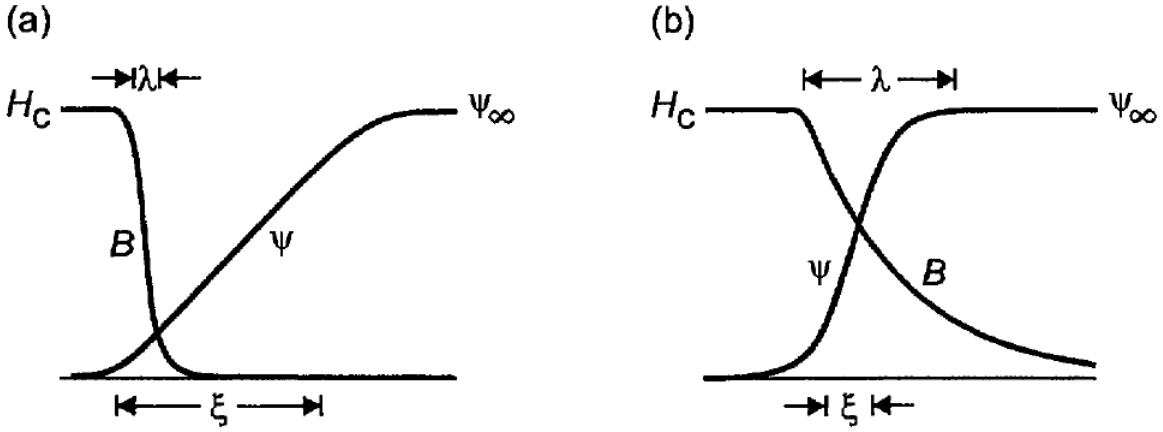

Figure 1.2: Schematic diagram of the domain wall in Type-I and Type-II superconductors. Figure reproduced from [31].

$$= \int dV \left(f_{sH_C} - f_{n0} - \frac{H_C B}{4\pi} + \frac{H_C^2}{8\pi} \right). \tag{1.23}$$

The simplest case is that of an infinite medium with the NS interface in the yz-plane and $\mathbf{B} \parallel c$ - for this it is possible to solve the GL equations. Introducing the dimensionless variables by $\overline{A} = \mathrm{A}/\mathrm{H}_c\lambda$ and $\overline{\psi} = \psi/\psi_\infty$, and using the gauge $\mathbf{A} = (0, \mathrm{A(x)}, 0)$, one gets

$$\overline{\psi}'' = \kappa \left(\left(\frac{\overline{A}^2}{2} - 1 \right) \overline{\psi} + \overline{\psi}^3 \right) \tag{1.24}$$

and

$$\overline{A}'' = \overline{\psi}^2 \overline{A}, \tag{1.25}$$

where the primes denote differentiation with respect to $\overline{x} = x/\lambda$. We may then reduce the expression for the surface energy to

$$\gamma = \frac{\lambda H_c^2}{8\pi} \int_{-\infty}^{\infty} d\overline{x} ((\overline{A}' - 1)^2 - \overline{\psi}^4). \tag{1.26}$$

By taking $\overline{\psi}^2$ = 1 - $\overline{A'}$ to ensure that $\gamma = 0$ one finds that the GL equations are satisfied if $\kappa = \frac{1}{\sqrt{2}}$, this is where the exact crossover from positive surface energy to negative surface energy occurs. In materials where $\kappa < \frac{1}{\sqrt{2}}$ (Type-I), $\gamma > 0$ so the most favourable configuration is the total expulsion of the magnetic field - the Meissner effect. In the type-

II scenario whereby $\kappa > \frac{1}{\sqrt{2}}$, $\gamma < 0$ and the magnetic field is confined to microscopic normal domains with a size determined by the coherence length ξ [31]. The negative surface energy causes the normal regions (which contain flux) to subdivide until a quantum limit is reached in which each quantum of flux passes through the sample as a distinct flux tube, and these flux tubes form an array (i.e. the vortex lattice), and the order parameter tends to zero along the axis of each one. Unlike the type-I superconductors, the vortex lattice occurs in the Shubnikov phase of type-II superconductors even if the sample demagnetising factor is zero.

1.3.4 The Flux Quantum

When considering a closed normal region, the magnetic flux is given by

$$\Phi = \int_S d\mathbf{S} \cdot \mathbf{B} = \oint_C d\mathbf{l} \cdot \mathbf{A} \tag{1.27}$$

where the left integral is over any surface S and the right line integral is over any loop C. This is known as the flux quantum and can be defined qualitatively as the ordinary magnetic flux through the integration loop [31]. By taking the contour distances to be much greater than λ and ξ where the superconducting screening current is zero and $\psi = \psi_\infty \mathrm{e}^{i\phi}$, one gets

$$\mathbf{A} = \frac{hc}{2e} \nabla \phi, \tag{1.28}$$

which yields

$$\Phi = \frac{\hbar c}{2e} 2\pi n = n\Phi_0. \tag{1.29}$$

under the condition that ψ is single valued. Φ_0 is the flux quantum,

$$\Phi_0 = \frac{hc}{2e} = 2.07 \times 10^{-15} \text{ Wb}. \tag{1.30}$$

1.3.5 Upper and Lower Critical Fields

Type-II superconductor behaviour is governed by two critical fields as mentioned in the introduction. When decreasing the field from the normal state to below the upper critical field, the material becomes superconducting as it is energetically favourable to create superconducting inclusions. As we can assume ψ is small, and therefore neglect it, we can use a linearised GL equation as follows

$$\frac{1}{4m}\left(-i\hbar\nabla - \frac{2e}{c}\mathbf{A}\right) = -\alpha\psi \tag{1.31}$$

with a uniform field equal to the upper critical field, H_{C2}. The lowest possible energy of a solution to this equation is $E = 1/2\ \hbar\omega_H$ where $\omega_H = eH/mc$ such that

$$-\alpha > \frac{e\hbar H}{2mc}, \tag{1.32}$$

which leads to

$$H_{c2} = -\frac{2mc\alpha}{e\hbar}. \tag{1.33}$$

By using all of the expressions for H$_C$, λ, ξ and κ, the following can be yielded:

$$H_{C2} = \sqrt{2}\kappa H_C = \frac{\Phi_0}{2\pi\xi^2}. \tag{1.34}$$

One can use the above reasoning to show that by increasing the field from zero it becomes favourable to create a normal inclusion above the lower critical field. The NS interface area is maximised as the domain wall energy is negative so the system will tend to create maximum fragmentation of the magnetic field. As the magnetic field is quantised each normal inclusion will carry one flux quantum. At H$_{C1}$ the surface energy gain must equal the cost in magnetic energy of the normal region. Therefore the surface energy per unit length, ϵ, may be written as

$$\epsilon L = H_{C1} \int dV \frac{B}{4\pi} = \frac{H_{C1}\Phi_0}{4\pi} L \rightarrow H_{C1} = \frac{4\pi\epsilon}{\Phi_0}. \tag{1.35}$$

The limit whereby $\kappa >> 1$ is known as the extreme type-II limit and corresponds to having an infinitesimally small core. In this limit it is possible to solve the GL equations which yield the field distribution necessary to calculate the surface energy per unit length. This gives

$$\epsilon = \left(\frac{\Phi_0}{4\pi\lambda}\right)^2 \ln\kappa, \tag{1.36}$$

and the lower critical field is

$$H_{C1} = \frac{\Phi_0}{4\pi\lambda} \ln\kappa, \tag{1.37}$$

1.4 BCS Theory

A microscopic theory of superconductivity was developed by Bardeen, Cooper and Schreiffer now known as BCS theory [7]. This brief section follows the treatment by Egetenmeyer [25]; a more comprehensive treatment can be found in Tinkham [97]. Two electrons forming a bound state above the filled Fermi sea are known as a Cooper pair, and can be described using the pair wavefunction

$$\psi(\mathbf{r}_1, \mathbf{r}_2) = \phi_{\mathbf{q}}(\rho) e^{i\mathbf{q}\cdot\mathbf{R}} \chi(\sigma_1, \sigma_2) \tag{1.38}$$

where the center of mass of the two electrons is at $\mathbf{R} = (\mathbf{r}_1 + \mathbf{r}_2)/2$, $\mathbf{q} = (\mathbf{r}_1 - \mathbf{r}_2)$, and σ_1 and σ_2 are the electron spins. χ is the spin part of the wavefunction and $\phi_{\mathbf{q}}$ is the spatial part of the wavefunction. The wavefunctions are chosen such that the overall wavefunction is antisymmetric and therefore satisfies Pauli's principle. If the spin wavefunction of the two electrons is a singlet, the spatial wavefunction must be symmetric. In the weak interaction limit of $N(\epsilon_F)V << 1$ where $N(\epsilon_F)$ is the density of states at the Fermi level and V is the interaction potential, two such particles have energy

$$\epsilon \approx 2\epsilon_F - 2\hbar\omega_c e^{-\frac{2}{N(\epsilon_F)V}} \tag{1.39}$$

where $\hbar\omega_c$ is an energy cut-off term to make the following approximation

$$V_{\mathbf{kk'}} = \begin{array}{cc} \text{-}V & E_F < \epsilon\left(\mathbf{k}\right) < E_F + \hbar\,\omega_c \\ 0 & \text{otherwise} \end{array} \tag{1.40}$$

where the matrix elements $V_{kk'}$ are given by

$$V_{\mathbf{kk'}} = \Omega' \int V(\mathbf{r}) e^{i(\mathbf{k'}-\mathbf{k})\cdot\mathbf{r}} d\mathbf{r} \tag{1.41}$$

which explains how the electron pair of momentum ($\mathbf{k'}$,$-\mathbf{k'}$) is scattered to the momentum ($\mathbf{k}$,$-\mathbf{k}$). $\mathbf{r}$ is the distance between the two electrons and Ω is the normalisation volume. Equation 1.39 implies that the Fermi sea is unstable against the formation of a bound pair. Pairs will condense until adding another pair is no longer energetically favourable. The following theory is for such a system of condensed Cooper pairs. The pairing Hamiltonian is given by

$$\mathcal{H} = \sum_{k\sigma} \epsilon_k n_{k\sigma} + \sum_{kl} V_{kl} c^*_{k\uparrow} c^*_{-k\downarrow} c_{-l\downarrow} c_{l\uparrow} \tag{1.42}$$

where

$$\epsilon_k = \frac{\hbar^2 k^2}{2m_e} - \mu \tag{1.43}$$

where μ is the chemical potential and $k = |\boldsymbol{k}|$.

The particle number operator is defined by $n_{k\sigma}$ = $\mathrm{c}_{k\sigma}{}^*$ $\mathrm{c}_{k\sigma}$ where σ stands for the up or down spin states, $\mathrm{c}_{k\sigma}{}^*$ is the creation operator of an electron of momentum $\boldsymbol{k}$ and spin σ, and $\mathrm{c}_{k\sigma}$ is the annihilation operator. Equation 1.42 describes the Coulomb interaction and the electron-phonon interaction of the Cooper pairs.

A mean field approximation to describe N electrons of an energy band where electrons appear in pairs is provided by BCS theory. The wavefunction in this approximation is given by the product of wavefunctions which each describe the simultaneous occupancy of the states -$\boldsymbol{k}\downarrow$ and $\boldsymbol{k}\uparrow$ by

$$\psi(\boldsymbol{k}) = u_k \mid 0,0\rangle_k + v_k \mid 1,1\rangle_k \tag{1.44}$$

where ${u_k}^2 + {v_k}^2 = 1$. $|u_k|^2$ is the probability that the pair state ($\boldsymbol{k}\uparrow$, -$\boldsymbol{k}\downarrow$) is not occupied and $|v_k|^2$ is the probability that the pair state ($\boldsymbol{k}\uparrow$, -$\boldsymbol{k}\downarrow$) is occupied. The wavefunction is

$$\mid \psi_{BCS}\rangle = \prod_k [u_k + v_k c^*_{k\uparrow} c^*_{-k\downarrow}] \mid \phi\rangle \tag{1.45}$$

where $|\phi\rangle$ is the vacuum state. A variational method is used to find parameters u_k and v_k, this requires that the u_k and v_ks are adjusted such that $u_k^2 + v_k^2 = 1$:

$$\delta\langle\psi_{BCS} \mid \mathcal{H} - \mu N_{op} \mid \psi\rangle = 0 \tag{1.46}$$

where

$$N_{op} = \sum_k (n_{k\uparrow} + n_{-k\downarrow}). \tag{1.47}$$

Calculations of the expression in equation 1.46 yields the result of the energy gap in the limit of weak coupling,

$$\Delta \approx 2\hbar\omega_c e^{-1/N(E_F)V}, \tag{1.48}$$

which also appears in the quasiparticle excitation energy,

$$E_{k_0} = \sqrt{\left(\Delta^2_{\boldsymbol{k}_0} + \left(\frac{\hbar^2 \boldsymbol{k}_0}{2m_e} - \mu\right)^2\right)}. \tag{1.49}$$

This describes the energy to excite a quasiparticle ($\boldsymbol{k}_0\uparrow$) from the BCS ground state. The excitation energy of a quasiparticle, $E_{\boldsymbol{k}0}$, must be a positive quantity $\geq \Delta$. The probability of an excitation in thermal equilibrium is the usual Fermi function

$$f(E_k) = \left(e^{\frac{E_k}{k_B T}} + 1 \right)^{-1} . \tag{1.50}$$

Therefore, the transition temperature T_C of the superconductor can be given by the expression

$$k_B T_C = 1.13 \hbar \omega_c e^{-1/N(E_F)V} . \tag{1.51}$$

Dividing equation 1.48 by equation 1.51,

$$\frac{\Delta}{k_B T_C} = \frac{2 \hbar \omega_c e^{-1/N(E_F)V}}{1.13 \hbar \omega_c e^{-1/N(E_F)V}}, \tag{1.52}$$

which gives the following expression for the gap at zero temperature

$$2\Delta(0) = 3.53 k_B T_C \tag{1.53}$$

which is obeyed in a wide range of different superconductors.

1.5 The Vortex Lattice

In a type-II superconductor, the magnetic field exists only in the normal inclusions which form vortices (and the penetration depth around them) that carry one flux quantum and are arranged in a periodic lattice. This section on the periodic lattice, known as the vortex lattice, follows the treatment by Eskildsen [31].

The symmetry of the vortex lattice is found by minimising $<f_s - f_n>$. Abrikosov [1] found that at H_{C2}

$$<f_s - f_n> = -\frac{\alpha^2}{\beta} \beta_A^{-1} \tag{1.54}$$

where $\beta_A = \frac{<\psi^4>}{<\psi^2>}$. In isotropic systems, one finds $\beta_A = 1.18$ for the square vortex lattice which monotonically decreases for the hexagonal (triangular) vortex lattice to $\beta_A = 1.16$.

Therefore the stable symmetry is the hexagonal vortex lattice, but this can be changed by even small anistropies as the energy difference is so small.

Each unit cell contains exactly one flux quantum, $B = \mathit{\Phi}_0/A_0$. We can calculate the unit cell area as we know the field, and therefore how many flux quanta must be present. For the square vortex lattice, the lattice parameters are given as

$$a_{square} = \sqrt{\frac{\Phi_0}{B}} \tag{1.55}$$

and for the hexagonal vortex lattice, the lattice parameters are given as

$$a_{hexagonal} = \sqrt{\frac{2}{\sqrt{3}}}\sqrt{\frac{\Phi_0}{B}} = 1.075\sqrt{\frac{\Phi_0}{B}}. \tag{1.56}$$

1.5.1 Distorted Vortex Lattice

Some materials have two-fold anisotropy. In these materials, a distorted vortex lattice is seen in the plane perpendicular to the direction that the field is applied [31]. This distortion, Γ, can tell us about the in-plane effective mass anisotropy (this mass refers to the effective electron mass, the in-plane effective masses are similar for cuprates, so typically $\approx$ 4 - 5 m_e) by

$$\Gamma = \frac{\lambda_a}{\lambda_b} = \frac{\xi_b}{\xi_a} = \sqrt{\frac{m_a}{m_b}}. \tag{1.57}$$

This two-fold anisotropy can be seen in some superconductors by rotating the applied field away from parallel to the c-axis. It is observed in $\mathrm{YBa_2Cu_3O_8}$ where the basal symmetry is broken by the direction of the CuO chains. The vortex lattice does not always have the high symmetry of the square and hexagonal scenarios but the vortex lattice is spanned by two vectors in the general case,

$$\mathbf{a} = a_0 \begin{pmatrix} \Gamma\cos\phi_0 \\ \sin\phi_0 \end{pmatrix} \tag{1.58}$$

$$\mathbf{b} = a_0 \begin{pmatrix} \Gamma\cos(\phi_0 + \Delta\phi) \\ \sin(\phi_0 + \Delta\phi) \end{pmatrix}. \tag{1.59}$$

ϕ_0 gives the orientation with respect to the anisotropy and $\Delta\phi$ is the opening angle, so for a square lattice this would be 90^o. We can derive expressions for ϕ_0 and $\Delta\phi$ as shown:

$$\Delta\phi = \arccos\left(\frac{a_\mathrm{x} a_\mathrm{y} + b_\mathrm{x} b_\mathrm{y}}{a_\mathrm{x} b_\mathrm{y} + a_\mathrm{y} b_\mathrm{x}}\right) \tag{1.60}$$

$$\phi_0 = \arctan\left(\frac{-b_\mathrm{x}/a_\mathrm{x} + \cos\Delta\phi}{\sin\Delta\phi}\right) \tag{1.61}$$

and there are related to the measure of anisotropy, Γ, by the following expression:

$$\Gamma = \frac{a_y}{a_x \tan\phi_0} = \frac{b_y}{b_x \tan(\phi_0 + \Delta\phi)}. \tag{1.62}$$

1.6 Vortex Pinning

In superconductors at small current densities, the vortices are pinned by inhomogeneities in the material. Vortex pinning is desirable in some materials such as high-temperature superconductors as it prevents “flux creep”. Flux creep can decrease the critical current density $\mathbf{J}_c$. This section will briefly describe how vortex pinning is caused in type-II superconductors.

In the presence of a transport current, the vortices in a Type-II superconductor experience a *Lorentz force* $\mathbf{J}$ x Φ_0/c per unit length, where Φ_0 is the flux quantum $= \frac{hc}{2e}$ and $\mathbf{J}$ is the current density. The Lorentz force causes a ‘resistive’ voltage as the Lorentz force tends to move the vortices sideways. Above H_{C1}, the superconductor cannot sustain a persistent current unless a mechanism known as a *pinning* force prevents the Lorentz force from moving the vortices. The pinning force *pins* vortices to fixed locations, this is a result of any spacial inhomogeneity of the material as local variations of the either the characteristic lengths or the critical field (due to impurities or grain boundaries) will cause local variations of ϵ_1, the free energy per unit length of the vortice, which causes some vortex positions to be more favourable. These inhomogeneities need to be of a similar scale to the characteristic lengths to be effective. Strong pinning can result in minimal vortex motion so that the superconductor behaves as a perfect conductor. [97]

There are several pinning mechanisms that exist in the case of high temperature superconductors, such as $YBa_2Cu_3O_7$ (YBCO). This section will briefly outline two of them: (i) points defects and (ii) twin planes.

1.6.1 Point Defects

The high temperature superconductors, which are strongly type-II (and therefore have a large κ), have a very small coherence length ξ. Therefore, any deviation from the stoichiometric compound at a single atomic site can locally suppress the superconducting order parameter. In YBCO, for example, a 10% change of oxygen in the CuO_2 planes (the structure of YBCO is explained in more detail in chapter 3), is enough to completely destroy the superconductivity. It is worth noting that even "high-quality" crystals are usually slightly off stoichiometry. This means that there are likely a large number of oxygen vacancies and each vacancy forms a point defect weak pinning centre [97].

1.6.2 Twin Planes

YBCO has an orthorhombic structure, i.e. $a \neq b$, therefore making twin planes prominent. The creation of twin planes are explained in more detail in chapter 3. A twin boundary exists between the twin planes where point defects accumulate. This suppresses the superconductivity and therefore attracts vortices. Due to the planar nature of the YBCO structure, the pinning has a very strong effect as the pinning acts in a coherent way unlike the random way it would act on a vortex lying in the plane. In high quality crystals, the pinning effects due to twin planes are only effective in a small range of orientations [97].

1.7 Unconventional Superconductivity

The BCS theory section assumes electron-phonon coupling and an isotropic system, so that $\Delta_{\mathbf{k}}$ is independent of $\mathbf{k}$, and due to the spherical symmetry it is referred to as s-wave pairing. The Cooper pairs here form a singlet pairing state with angular momentum $\ell = 0$. When dealing with an anisotropic material, then it is no longer expected that $\Delta_{\mathbf{k}}$ is isotropic but that it's dependence on $\mathbf{k}$ will match the symmetry of the underlying crystal symmetry [97]. An example of this is a tetragonal crystal, it will typically have a different gap for $\mathbf{k}$ along c than for $\mathbf{k}$ along a or b. The symmetry of the gap at intermediate directions between c and a-b cannot be lower than tetragonal. This can be described as anisotropic s-wave pairing whereby it shares it's symmetry with the underlying crystal but does not possess the spherical symmetry of isotropic s-wave pairing. A superconductor is considered to be unconventional if the superconducting gap $\Delta_{\mathbf{k}}$ is of lower symmetry than that of the underlying crystal. In this case the Cooper pairs may have angular momentum and pairing states exist where $\ell \neq 0$. A lower symmetry may imply an alternative pairing mechanism to the electron-phonon mechanism of BCS theory, and also strong electron correlations [13].

Figure 1.3 shows the different gap functions. The unconventional pairing states, unlike the s-wave gap, do not have a spherical symmetry. Many of the cuprate superconductors are known to have $d_{x^2-y^2}$ (or similar) gap symmetry. They often have a tetragonal crystal structure, and the gap symmetry is lower than this. Angle-resolved photoemission spectroscopy (ARPES) measurements [99] on BSCCO found a gap-like feature along the $\mathbf{k}_x$ and $\mathbf{k}_y$ but not in the directions rotated by 90° from them in the a-b plane. The gap functions shown in figure 1.4 have the same symmetry properties as atomic orbital functions, with the s-wave state and d-wave state having $\ell = 0$ and $\ell = 2$, respectively.

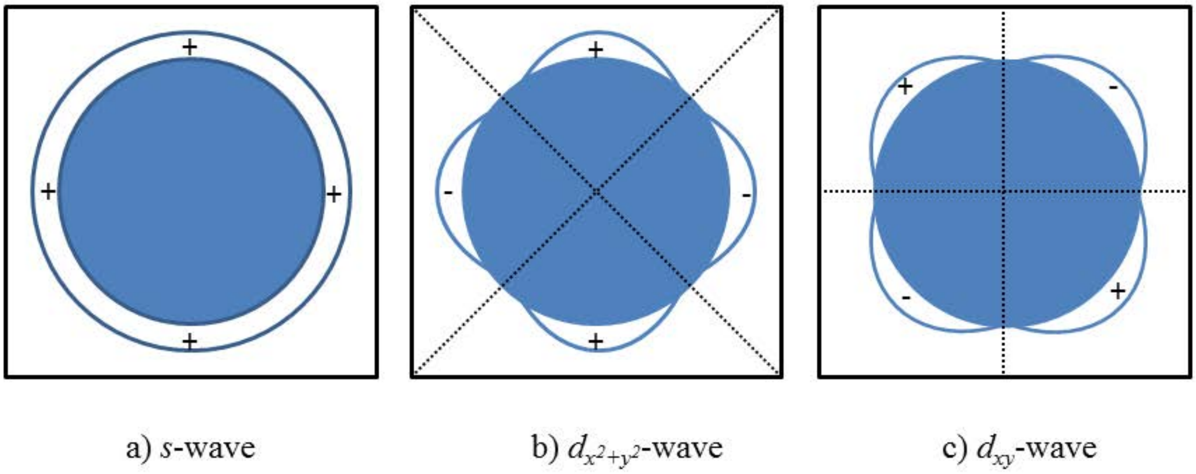

a) s-wave

b) $d_{x^2+y^2}$-wave

c) d_{xy}-wave

Figure 1.3: (a) s-waves superconducting gap, (b) $d_{x^2+y^2}$-wave superconducting gap, and (c) d_{xy}-wave superconducting gap represented over a 2-dimensional representation of the Fermi surface in reciprocal space. The '+' and '-' signs represent the phase of the order parameter, and the dotted lines represent planes of broken symmetry.

1.8 Pauli-limited Superconductivity

1.8.1 Coexistence of superconductivity and magnetism

It is known that magnetism and superconductivity compete in many materials, and that magnetic ordering can lead to the altering of the phase coherence of a superconductor or break up the Cooper pairs [53]. More recently there has been evidence of the coexistence of superconductivity and magnetism. The first superconductors found to feature magnetic order were the molybdenum borides and the rare-earth rhodium borides which were conventional superconductors with antiferromagnetic order. Here the internal magnetic fields produced by the antiferromagnetic ordering is much shorter than the coherence length, therefore the *s*-wave Cooper pairs are not broken up by the magneto-static effect [6, 18].

In 1979, the first heavy fermion superconductor was discovered - $CeCu_2Si_2$ [85]. The main aspect of this new class of superconductor that substantially differentiated it from previous superconductors was the presence of strong electron-electron interactions. Strongly correlated metals can result in both the magnetic and electronic fluctuations being intertwined and being contributory factors in the onset of superconductivity. On a microscopic scale, magnetic order and superconductivity coexist in several heavy fermion compounds [101].

The *p*-wave superconductors also exhibit the coexistence of superconducting and magnetic order. Here the superconductivity results from triplet Cooper pairs which can have magnetic moments. The magnetic moments of the Cooper pair couple to other magnetic degrees of freedom in the material. A possible example of this behaviour is in the ferromagnetic superconductor UGe_2 [43]. The superconductivity arises in the critical regions when the ferromagnetism is suppressed by a non-thermal parameter (such as pressure). The superconductivity arises only whilst ferromagnetic ordering is present indicating that there is a coupling between the superconductivity and the magnetic order.

1.8.2 Exotic Magnetism in Superconductors

A relatively new idea is magnetic order which is caused by superconductivity rather than simply coexisting with superconductivity. FFLO theory by Fulde & Ferrell [36] and Larkin & Ovchinnikov [62] predicted, for s-wave superconductors, that superconducting pair-density waves can drive *exotic* magnetism - this is where the Cooper pair density modulates spatially. They are predicted for Pauli-limited superconductors at high fields. Here the orbital effects are weak and H_{C2} does not depend on the orbital supercurrents of the flux lines. In superconductors with a short coherence length, the Pauli-limiting effects are enhanced which leads to high orbital limiting fields. In superconductors with a low-dimensional electronic structure the orbital supercurrents are weak due to the restricted motion of the electrons perpendicular to the field. Therefore heavy-fermion superconductors and low-dimensional superconductors are likely to follow pair density wave superconductivity at high fields.

Pair density wave superconductivity, which is described by a spatially modulated superconducting order parameter, requires a field that splits the conducting bands, leading to mismatched energies for spin-up and spin-down electron bands. This results in the spin-up and spin-down electron bands having different Fermi wavevectors in the normal state. In the superconducting state the momentum of the spin-up and spin-down electrons does not equal zero so the Cooper pairs have a finite momentum. The superconducting condensate is described by a singlet wave function and is modulated with a wave vector that is incommensurate with the (underlying) structural lattice. This is a special case of pair density wave superconductivity known as FFLO superconductivity [36, 62]. The FFLO state arises if the mechanism to suppress superconductivity is Pauli pair breaking, so it cannot arise in conventional superconductors where the orbital pair breaking is stronger. In heavy fermion superconductors, however, the f-electrons hybridise with the normal conduction electrons leading to enhanced mass quasiparticles, which suppress the effect of orbital pair breaking.

There are two fundamental mechanisms at the core of the FFLO state; the interaction of the spin of electrons with the magnetic fields, and the condensation energy. In the normal state, the electrons align to the direction of the magnetic field so as to minimise their energy which, in turn, leads to a T-dependent Pauli susceptibility. In the superconducting singlet state, the Cooper pairs are broken when the Pauli energy becomes greater than the superconducting condensate energy. Therefore, the Pauli mechanism favours the normal state over the superconducting singlet state which, therefore, lowers the upper critical field and suppresses the superconductivity. This mechanism is known as Pauli-limiting and the upper limit of the Pauli limited field is given as H_P. Orbital limiting will also lead to the suppression of superconductivity. The kinetic energy of the supercurrent around the core of the superconducting vortices will decrease the condensate energy, and the critical field for superconductivity susceptibility due to the effect of the orbital movement of the supercurrent (not including the Pauli effect) is defined as H_{c2}^{orb}. The relative strength of the Pauli and orbital limiting is called the Maki parameter, $\alpha = \sqrt{2}\,\frac{H_{c2}^{orb}}{H_P}$.

It is also argued that charge density wave or spin density wave order can lead to the modulation of the superconducting condensate and thus give rise to pair density wave superconductivity.

The formation of triplet Cooper pairs with finite momentum is also possible if the electrons paired have momenta that are not equal and opposite. This is different to the singlet superconductivity of FFLO. It was argued by Shimihara [81] that although singlet superconductivity is dominant at zero field, triplet superconductivity is dominant in Pauli-limited systems at high fields as the singlet pairing is suppressed by the Pauli paramagnetic pair-breaking effect.

Conduction electrons can mediate the exchange interaction between magnetic ions. The conduction electrons are spin-polarised by a localised magnetic moment, and this polarisation couples to a neighbouring localised magnetic moment a distance r away. This exchange interaction does not involve any direct coupling between the magnetic moments, and is therefore an indirect interaction. This is known as the RKKY interaction. The exchange interaction is given by

$$J_{RKKY}(r) \propto \frac{cos(2k_F r)}{r^3} \tag{1.63}$$

at large r (where k_F is the radius of the spherical Fermi surface) [11].

A conventional superconductor, whereby a uniform gap is induced in the Fermi surface, cannot form any magnetic ordering due to the absence of low-energy quasiparticles. Unconventional superconductors, on the other hand, have low-energy quasiparticles as they have point or line nodes in the superconducting state, and can therefore form magnetic order. In order for the coexistence of magnetic order and superconductivity, the nesting vector and the line nodes have to coincide. However, in $\mathrm{CeCu_2Si_2}$, the wave vector is $\mathbf{Q} = (0.21,\ 0.21,\ 0.47)$ - this is not along the nodal direction of the d_{xy}-wave order parameter in the *ab* plane. However, superconductivity and spin density wave order do not microscopically coexist in this compound [87]. This agrees with the prediction that in order to form a coexistence of superconductivity and magnetic order, the spin density wave ordering wave vector must lie in the nodal direction.

When a field is applied the electronic structure of a type-II superconductor is changed because of the presence of vortices. The presence of bound fermion states in the vortex line of a type-II superconductor (whose energy is lower than than the gap Δ) was found by Caroli, De Gennes and Matricon [16].

Fulde & Ferrell and Larkin & Ovchinnikov (FFLO) [36, 62] found that in the case of an *s*-wave superconductor in the presence of magnetic fields, modulated singlet superconductivity is possible. This is stabilised by either an external field or possible exchange fields. Figure 1.4 schematically shows that this leads to a modulated singlet pair density wave phase [53, 67].

A study by Psaltakis & Fenton [76] looked at the case where the emergence of spin density wave order and superconductivity comes from the same electrons. They were able to show that both spin-singlet and spin-triplet Cooper pairing must occur at the same

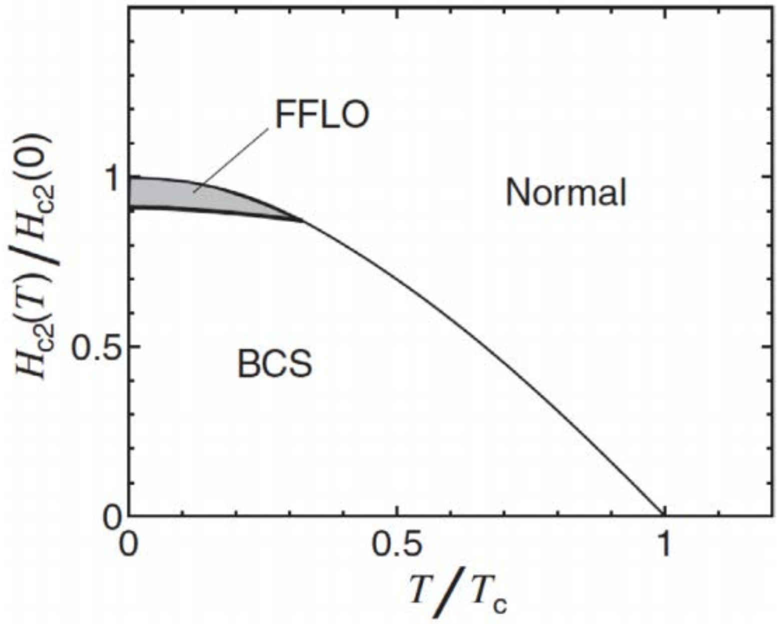

Figure 1.4: $H - T$ phase diagram of a conventional Pauli-limited superconductor with an FFLO phase at low T and close to H_{C2} [67].

time. Shimihara [81] argued that spin fluctuations are the driving force for superconducting pairing interactions, and they include an attractive potential for both singlet Cooper pairs and triplet Cooper pairs. It was shown that singlet pairing is realised in the absence of field but Pauli-paramagnetic effects suppress the singlet superconductivity and triplet superconductivity is favoured.

A singlet d-wave superconductor was studied by Lebed [63], and he argued that the parity and spin-rotational symmetry of the superconductivity order is broken if the triplet pairing is active. He also claimed that the coexistence of singlet Cooper pairs and triplet Cooper pairs is enhanced when the orbital critical field is approximately equal to the Pauli-limiting field.

Aperis *et al*. [4] studied the phases of a mean-field model Hamiltonian that exhibits spin density wave order, d-wave superconductivity and modulated triplet superconductivity. The authors showed that an asymmetry of the particles and holes leads to the coexistence of all three order parameters. It was shown that a phase consisting of both spin density wave order and triplet superconductivity emerges near H_{C2} - this is shown in figure 1.5 [3]. The pair density wave superconductivity found by Aperis *et al*. is a

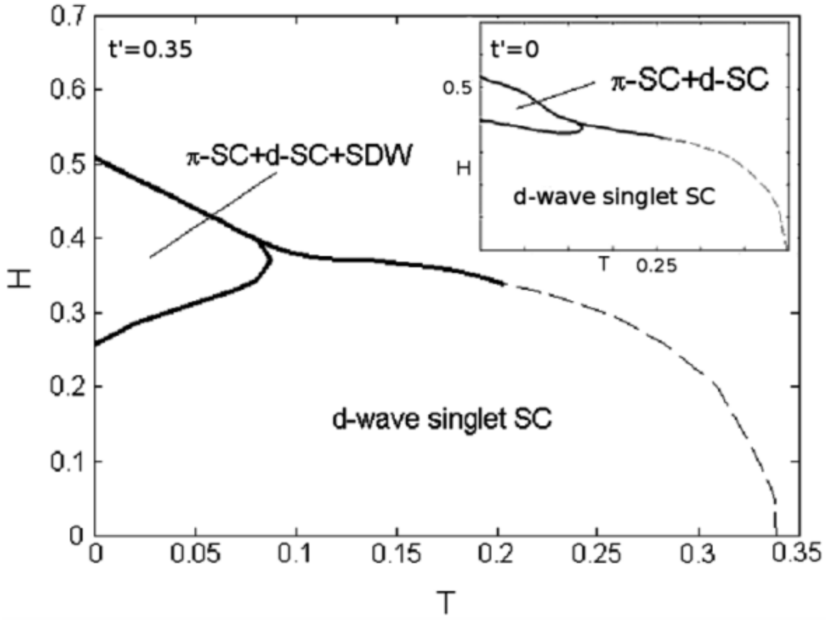

Figure 1.5: $H-T$ phase diagram of a d-wave Pauli-limited superconductor with an instability to spin density wave order and triplet pair density wave order. π-SC is modulated triplet superconductivity [3].

triplet pair density wave whereas the modulated superconductivity of the FFLO phase is singlet superconductivity. The modulated vector q is proportional to the field in the FFLO phase, but the modulation of the triplet superconductivity is due to the electronic nesting properties of the material [53].

Ikeda *et al.* [48] showed that the spin density wave order close to H_{C2} is due to Pauli depairing effects. They found that the triplet pair density wave order or FFLO are not required for the spin density wave order to arise, however the magnetic order is stronger if the FFLO phase is present. Suzuki *et al.* [89] studied how the electronic structure in vortices can be affected by Pauli depairing using a quasiclassical microscopic Eilenberger theory (described later) for a $d_{x^2-y^2}$-wave superconductor giving direct information regarding the quasiparticles in the vortices themselves. Suzuki *et al.* claim that the DOS is enhanced along the direction of the nodes and can lead to spin density wave instabilities. This is in stark contrast to the claim of Michal & Mineev [69], who consider a Pauli-limited $d_{x^2-y^2}$-wave superconductor, as they find that $d_{x^2-y^2}$-wave spin excitons are condensed into the ground state at high magnetic fields which results in the coexistence of superconducting and magnetic order [53].

1.8.3 Influence of paramagnetic effects on the vortex lattice

One of the two mechanisms for magnetic field induced pair-breaking of superconductivity is diamagnetic pair-breaking due to the screening current around the vortices from the contribution of the vector potential. The other mechanism is Pauli-paramagnetic pair-breaking - this is due to the Zeeman energy leading to different Fermi surfaces for spin-up and spin-down electrons [46]. In the presence of strong paramagnetic effects, the behaviour of the vortex lattice is different to the conventional vortex state. For example, in CeCoIn_5 the vortex lattice form factor (which describes the spatial variation of the magnetic field within the vortices themselves) increases as a function of applied magnetic field which is in stark contrast to the exponential decrease of the form factor which is expected in other superconductors. The purpose of this section is to understand how paramagnetic contributions are made on the vortex lattice, and how they affect the vortex lattice form factor. A more comprehensive description on how the vortex lattice form factor is derived is given in chapter 2. The paramagnetic effect on the field dependence of low temperature magnetisation, Knight shift and specific heat has been quantitatively studied [45, 113], and each of these quantities showed sharp increases near the upper critical field by the paramagnetic pair breaking. Ichioka & Machida [45] also showed that the vortex lattice form factor does not decay exponentially with increasing field, and it can in fact increase as a function of field (at fields well below H_{C2}).

This section, following the treatment by Ichioka & Machida [46], will evaluate the paramagnetic contributions on the vortex lattice form factor based on quasiclassical Eilenberger theory. The paramagnetic effects are not the same for both *d*-wave and *s*-wave superconductors, and the differences between the two will also be highlighted in this section. The Eilenberger equations [26], combined with some Green's function methods, can provide a complete quasiclassical description of a superconductor. First we calculate the spatial structure of the vortex lattice state by the quasiclassical Eilenberger theory. This

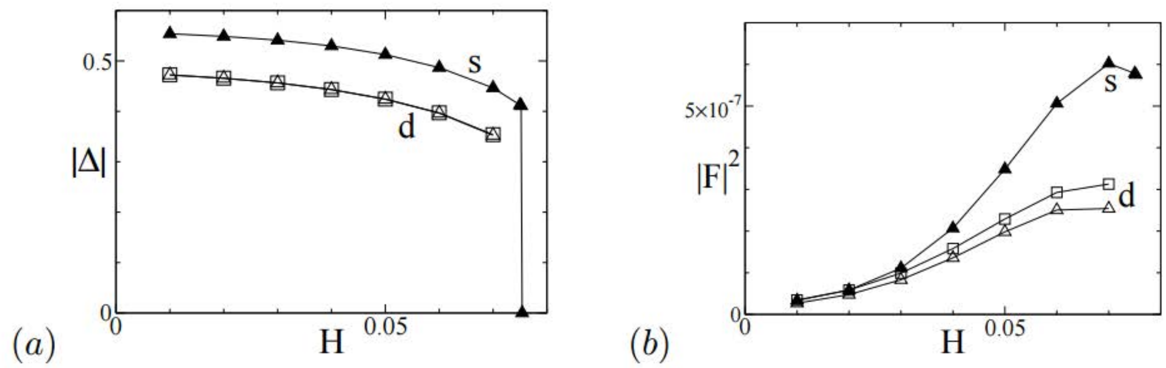

Figure 1.6: (a) The spatial averaged $|\Delta|$ as a function of applied field. (b) The vortex lattice form factor as a function of applied field. Both (a) and (b) are at $T = 0.2T_c$. The s-wave pairing is is shown as the filled triangle, and the d-wave pairing cases are shown as an unfilled triangle and an unfilled square. The triangles and squares are to indicate the vortex lattice structure. Figure is reproduced from [46].

includes the paramagnetic effects $\mu_B B(\mathbf{r})$, where $B(\mathbf{r})$ is the flux density of the internal magnetic field and μ_B is the Bohr magneton [45]. $g(\omega_n + \mathrm{i}\mu B,\mathbf{k},\mathbf{r})$, $f(\omega_n + \mathrm{i}\mu B,\mathbf{k},\mathbf{r})$ and $f^\dagger(\omega_n + \mathrm{i}\mu B,\mathbf{k},\mathbf{r})$, the quasiclassical Green's functions, are calculated in the vortex lattice by the Eilenberger equation

$$\{\omega_n + \mathrm{i}\mu B + \mathbf{v}\cdot(\nabla + \mathrm{i}\mathbf{A})\}f = \Delta\phi \mathrm{g}, \tag{1.64}$$

$$\{\omega_n + \mathrm{i}\mu B - \mathbf{v}\cdot(\nabla - \mathrm{i}\mathbf{A})\}f^\dagger = \Delta^*\phi^* \mathrm{g}, \tag{1.65}$$

where $\mu = \mu_B B_0/\pi k_B T_C$, $g = (1 - ff^\dagger)^{1/2}$ and Re $g > 0$. Two cases are considered: s-wave pairing ($\phi(\mathbf{k}) = 1$) and d-wave pairing ($\phi(\mathbf{k}) \propto \cos 2\psi$) where $\mathbf{k}$ is the relative momentum of the Cooper pair on the spherical Fermi surface. $\mathbf{r}$ is the center of mass position of the Cooper pair. $\mathbf{v}$ ($= \sin\theta \cos\psi, \sin\theta \sin\psi, \cos\theta$) is the normalised Fermi velocity, and is $\propto \mathbf{k}$. The length is scaled by $R_0 = \hbar v_{F0}/2\pi k_B T_c$, and the field is scaled by $B_0 = \hbar c/2|e|R_0^2$ [45, 46]. In the symmetric gauge, since the field is along the z-direction, the vector potential $\mathbf{A}(\mathbf{r}) = \frac{1}{2}\bar{\mathbf{B}} \times \mathbf{r} + \mathbf{a}(\mathbf{r})$ where $\bar{\mathbf{B}}$ ($= (0, 0, H)$) is a uniform flux density and $\mathbf{a}(\mathbf{r})$ is related to the internal field $\mathbf{B}(\mathbf{r}) = \bar{\mathbf{B}} + \nabla \times \mathbf{a}(\mathbf{r})$. The unit cell of a vortex lattice for $\Delta\mathbf{r}$ is $\mathbf{r} = s_1(\mathbf{u}_1 - \mathbf{u}_2) + s_2\mathbf{u}_2$ where $-\frac{1}{2} \leqslant s_1, s_2 \leqslant \frac{1}{2}$, $\mathbf{u}_1 = (\mathrm{a}, 0, 0)$ and $\mathbf{u}_2 = (\frac{a}{2}, a_y, 0)$. For a triangular vortex lattice $\frac{a_y}{a} = \frac{\sqrt{3}}{2}$ and for a square vortex lattice $\frac{a_y}{a}$

$= \frac{1}{2}$ [46]. The pair potential is

$$\Delta(\mathbf{r}) = g_0 N_0 T \sum_{0<\omega_n \leqslant \omega_{cut}} \langle \phi^*(\mathbf{k})(f + f^{\dagger *}) \rangle_{\mathbf{k}}, \tag{1.66}$$

where

$$(g_0 N_0)^{-1} = \ln T + 2T \sum_{0<\omega_\mathrm{n} \leqslant \omega_\mathrm{cut}} \omega_\mathrm{l}^{-1} \cdot \langle \phi^*(\mathbf{k})(f + f^{\dagger *}) \rangle_{\mathbf{k}} \tag{1.67}$$

is the Fermi surface average. Ichioka & Machida [46] use $\omega_{cut} = 20 k_B T_c$. The vector potential for the internal field is calculated by

$$\nabla \times (\nabla \times \mathbf{A} = \nabla) \times \mathbf{M}_{para}(\mathbf{r}) - \frac{2T}{\kappa^2} \sum_{0<\omega_n} \langle \mathbf{v} \mathrm{Im} g \rangle_{\mathbf{k}} \tag{1.68}$$

where the last term includes the diamagnetic contribution of supercurrent and $\mathbf{M}_{para}(\mathbf{r})$ ($= (0,\ 0,\ M_{para}(\mathbf{r}))$ is the paramagnetic contribution where

$$M_{para}(\mathbf{r}) = M_0 \big(\frac{B(\mathbf{r})}{H} - \frac{2T}{\mu H} \sum_{0<\omega_n} \langle \mathrm{Im\{g\}} \rangle_{\mathbf{k}} \big). \tag{1.69}$$

M_0 ($= (\mu/\kappa)^2 H$) is the paramagnetic moment in the normal state, $\kappa = B_0/\pi k_B T \sqrt{8\pi N_0}$ where N_0 is the density of states at the Fermi energy when in the normal state [46]. κ = 17 and the paramagnetic parameter μ = 5 in the calculation by Ichioka & Machida. The field dependence of the spatial averaged $|\Delta|$ at $T = 0.2 \times T_C$ in the case of a strong paramagnetic effect (indicated from a large μ). This is shown in figure 1.6(a). The different ratio $\Delta/k_B T_c$ of the *s*-wave and *d*-wave pairings determines the difference of $|\Delta|$.

With $H = 0.05 B_0$ and in the presence of strong paramagnetic effects ($\mu = 5$), figure 1.7 shows the spatial structures of the vortex states for *s*- and *d*-wave pairings. At r = 0 (the normal vortex core), the paramagnetic contribution M_{para} is enhanced. At the vortex center it can be seen that the paramagnetic contribution is larger in *s*-wave pairing than in *d*-wave pairing, but because the low energy states extend outside the vortex core due to the node of the gap in *d*-wave pairing, the paramagnetic moment is larger outside

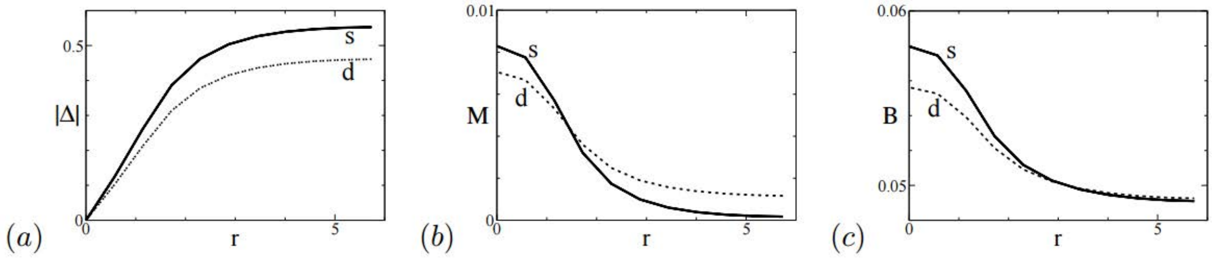

Figure 1.7: (a) Profiles of the pair potential, $|\Delta|$, the paramagnetic moment, M_{para}, and the internal field B as a function of r which is the distance from the vortex center to the midpoint of the neighbouring vortices. $T = 0.2T_c$, $\mu = 5$, $\kappa = 17$ and $H = 0.05B_0$. Figure reproduced from [46].

the core than in s-wave pairing. The internal field, as shown in figure 1.7(c), is enhanced at $r = 0$ by the paramagnetic moment at the core (the internal field $B(\mathbf{r})$ is made up of both diamagnetic and paramagnetic contributions).

One of the experimental methods employed to observe the additional paramagnetic moment around the vortex cores is to measure the vortex lattice form factor using the small-angle neutron scattering (SANS) technique which will be explained in the following chapter. The intensity of the (h,k) diffraction peak can be given as

$$I_{h,k} = \frac{\mid F_{h,k} \mid^2}{\mid \mathbf{q}_{h,k} \mid} \tag{1.70}$$

where $\mathbf{q}_{h,k}$ ($= h\mathbf{q}_1 + k\mathbf{q}_2$) is the wave vector where $\mathbf{q}_1 = (2\pi/\mathrm{a}, -\pi/\mathrm{a}_y, 0)$ and $\mathbf{q}_2 = (2\pi/\mathrm{a}, \pi/\mathrm{a}_y, 0)$. The form factor $F_{h,k}$ is the Fourier transformation of the internal field as $B(\mathbf{r}) = \sum_{h,k} F_{h,k} \exp(\mathrm{i}\mathbf{q}_{h,k} \cdot \mathbf{r})$. The form factor $|F_{h,k}|$ for the main peak at $(h,k) = (1,0)$ is shown in figure 1.6(b) as a function of magnetic field. The intensity at the main peak probes the field contrast between the vortex core and the surrounding. In materials with a weak paramagnetic effect (negligible μ), $|F_{h,k}|^2$ decreases exponentially with applied field because the internal field $B(\mathbf{r})$ decreases as H increases. In the case of a strong paramagnetic effect, the form factor increases as the upper critical field is approached because the internal field increases due to the enhanced paramagnetic moment at the core.

1.8.4 Pauli-limiting effects in $CeCu_2Si_2$ and YBCO

This thesis is based on the experimental results of two unconventional superconductors: the heavy-fermion $CeCu_2Si_2$ and the High-T_c cuprate $YBa_2Cu_3O_7$. This section will briefly outline why it is necessary to elucidate the Pauli-paramagnetic effects in these two systems.

$CeCu_2Si_2$

$CeCu_2Si_2$, along with $CeCoIn_5$ [9] and UPd_2Al_3 [90], is a known Pauli-limited superconductor at ambient pressure. It was the first unconventional superconductor to be discovered [85], and although arguments still remain about the exact gap function (thought to be d_{xy} [93] several years ago), more recent evidence indicates $s_{\pm}$ symmetry [47]. The superconductivity in $CeCu_2Si_2$ is near a magnetic quantum critical point. The exact stoichiometry can influence whether the sample is antiferromagnetic (A-type), superconducting (S-type) or both antiferromagnetic & superconducting (A/S-type). A/S samples exhibit both spin density wave order and superconductivity. The antiferromagnetic spin density wave order has the wave vector $Q = (0.28,\ 0.28,\ 0.53)$ and is in direct competition with the superconductivity [87]. The competition is consistent with d_{xy} and $s_{\pm}$ symmetry as the gap is along the $(h,\ h,\ l)$ direction.

Specific heat measurements were recently undertaken on an S-type sample [55] which provided evidence for multiband superconductivity. The results show that for fields close to the upper critical field and at low temperatures, the specific heat increases. A superconductor with strong paramagnetic effects is expected to have a first order superconducting-to-normal phase transition at low temperatures, however there is no evidence to support the idea that the transition at the upper critical field is of first order in $CeCu_2Si_2$. However, this does not discount $CeCu_2Si_2$ as a Pauli-limited superconductor as it was argued by Tsutumi *et al* [98] that the upper critical field can remain second order even at very low temperatures in a multiband superconductor (which $CeCu_2Si_2$ may well be — this is explained more thoroughly in chapter 4).

There is little direct evidence of paramagnetic effects in $CeCu_2Si_2$ prior to the work presented in this thesis.

$\mathbf{YBa_2Cu_3O_7}$

Some high T_c superconductors have been argued to be Pauli-limited. A high field study (up to 600 T) by Sekitani *et al.* [79] found that that the upper critical field of $YBa_2Cu_3O_7$ shows paramagnetic limiting effects when the field is applied parallel to the CuO_2 planes. The field-dependence of the upper critical field is expected to follow Werthamer-Helfand-Hohenberg (WHH) theory [100] (whereby the quenching of the superconductivity is explained only by the orbital effects), but this was only the case when the field was applied perpendicular to the CuO_2 planes. With the field parallel to the CuO_2 planes, there was a large discrepancy between the experimental results and the WHH model which was explained by Sekitani *et al.* to be the result of the spin-orbit effect and the Pauli limit which results in the destruction of the Cooper pair singlet when the Zeeman energy becomes greater than the gap [79]. Other high T_C superconductors have also shown paramagnetic effects. Slightly underdoped $Bi_2Sr_2CuO_{6+\delta}$ was studied by resistivity measurements as a function of field and showed a T-dependence of the upper critical field indicating the presence of paramagnetic effects [95]. Resistivity measurements on the electron-doped $Pr_{2-x}Ce_xCuO_{4-\delta}$ suggest that H_{C2} is determined by Pauli-limiting effects [64].

Pauli-paramagnetic effects are yet to be seen in any high T_C material via small-angle neutron scattering as the critical fields in high T_C superconductors are often much higher than that available at neutron beam-lines, hence mostly resistivity and magnetic susceptibility measurements having been carried out until very recently [53]. However, due to advances in magnet technology for a neutron beamline, we are able to present evidence of Pauli-paramagnetic effects via small-angle neutron scattering measurements later in this thesis.

1.8.5 Summary

Very few superconductors have been experimentally confirmed as Pauli-limited; this is for three main reasons [53]. The first is that only a few materials have Hamiltonians that place them near the Pauli limit. Experiments also require very high sample quality which is a technical challenge in many systems which are highly sensitive to the precise stoichiometry, such as $CeCu_2Si_2$. The third is that the novel phases must occur in a temperature and field range that is easily accessible, and preferably without the application of pressure. There are only a few materials which tick all of these boxes.

Chapter 2

Small-Angle Neutron Scattering

The intrinsic magnetic moment of the neutron makes it an effective probe of the magnetic vortex lattice in superconductors. Most experimental methods (such as Bitter decoration, scanning-SQUID, and magnetic force microscopy) of imaging the vortex lattice rely on measuring the modulation of the value of the magnetic field due to the vortices. The modulation decreases with field and the distance from the surface, so these surface-sensitive techniques are limited to small magnetic fields. Some other magnetic probes work on the principle of scanning rather than imaging such as scanning hall-probe microscopy which directly measures the local field profile at the sample surface. However, local probe techniques such as scanning Hall-probe microscopy are problematic as their spatial resolution is poor which means they are limited only to low field studies which implies that the more phase transitions in many unconventional superconductors are inaccessible. The fact that they also only measure the vortex lattice at the surface, rather than the bulk, and only a small region of the sample are additional reasons to favour small-angle neutron scattering. Scanning tunnelling microscopy (STM) is quite complementary to bulk techniques as it measures the local density of state of quasiparticles. In particular, STM allows a more direct measurement of the symmetry of the order parameter by its effect on the local density of states near a vortex core. However, STM can still only measure a small region of a sample unlike the sample-averaged bulk measurements provided by small-angle neutron scattering and muon spin rotation.

Muon spin rotation (μSR) is directly sensitive to the distribution of field values within the Shubnikov phase. It is also limited at high fields, but this is mainly due to the issue of getting the muon and its associated positron into and out of the sample. The μSR technique is not sensitive to vortex lattice disorder, therefore the results may be affected by local magnetic order [32]. Small-angle neutron scattering, due to its relative simplicity, would appear to be the experiment of choice for most studies of the vortex lattice structure, however, there are many occasions where μSR studies can provide complementary information to small-angle neutron scattering. For example, neutron scattering alone cannot measure the sign of the Fourier component because the intensity of the scatter is proportional to the modulus squared (as we shall see later in this chapter), but by taking the signs from theory, the real space vortex lattice can be reconstructed from which the muon lineshape may be calculated and compared with experiment. In some scenarios, μSR may be preferred to small-angle neutron scattering, such as when measuring samples with very long penetration depths.

This section provides an overview of small-angle neutron scattering and a description of the information that can be yielded from this technique when studying the vortex lattice in type-II superconductors.

2.1 Neutron Scattering Theory

Neutrons can probe the magnetic structure of crystals due to its magnetic moment (μ_n = 9.66×10^{-27} J T^{-1}). The neutron has a momentum $\boldsymbol{p} = \hbar\boldsymbol{k}$ where the wave vector $\boldsymbol{k}$ = $\frac{2\pi}{\lambda}$, and the energy associated with the neutron is $E = \frac{\hbar^2 k^2}{2m}$.

The reciprocal lattice is a useful tool when describing neutron scattering theory. The direct lattice describes the position of unit cells in terms of three basis vectors:

$$\mathbf{r} = n_1\mathbf{a} + n_2\mathbf{b} + n_3\mathbf{c}. \tag{2.1}$$

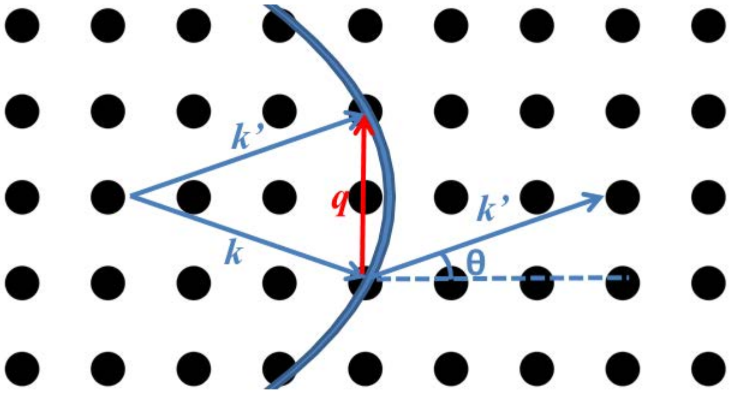

Figure 2.1: To illustrate the scattering condition, we show the Ewald construction in reciprocal space. The Ewald sphere (shown as the blue arc) has a radius k. For scattering to occur, the scattering vector $\boldsymbol{q}$ must connect two reciprocal lattice points lying on the Ewald sphere surface as shown.

Now the basis vectors of a reciprocal lattice are defined as:

$$\mathbf{a}_1^* = \frac{2\pi}{V_0}\mathbf{a}_2 \times \mathbf{a}_3 \tag{2.2}$$

$$\mathbf{a}_2^* = \frac{2\pi}{V_0}\mathbf{a}_3 \times \mathbf{a}_1 \tag{2.3}$$

$$\mathbf{a}_3^* = \frac{2\pi}{V_0}\mathbf{a}_1 \times \mathbf{a}_2 \tag{2.4}$$

where

$$V_0 = \mid \mathbf{a}_1 \cdot \mathbf{a}_2 \times \mathbf{a}_3 \mid . \tag{2.5}$$

The basis vectors of the direction and reciprocal lattice have the following two properties:

$$\mathbf{a} \cdot \mathbf{a}^* = \mathbf{b} \cdot \mathbf{b}^* = \mathbf{c} \cdot \mathbf{c}^* = 2\pi \tag{2.6}$$

and

$$\mathbf{a} \cdot \mathbf{b}^* = \mathbf{a} \cdot \mathbf{c}^* = \mathbf{b} \cdot \mathbf{a}^* = \mathbf{b} \cdot \mathbf{c}^* = \mathbf{c} \cdot \mathbf{a}^* = \mathbf{c} \cdot \mathbf{b}^* = 0. \tag{2.7}$$

Bragg's law is

$$n\lambda = 2dsin\theta \tag{2.8}$$

where λ is the neutron wavelength, 2θ is angle between $\boldsymbol{k}$ and $\boldsymbol{k}$' where $|\boldsymbol{k}| = |\boldsymbol{k}'|$ for elastic scattering. As shown in figure 2.1, the initial propagation vector $\boldsymbol{k}$ and the final propagation vector $\boldsymbol{k}$' have a difference of the scattering vector. The scattering vector is given by

$$\boldsymbol{q} = \boldsymbol{k}' - \boldsymbol{k}, \tag{2.9}$$

as shown in figure 2.1. Bragg's law in reciprocal space is given as

$$q = 2k\mathrm{sin}\theta \tag{2.10}$$

where k is the magnitude of the propagation vector,

$$k = \frac{2\pi}{\lambda} \tag{2.11}$$

and the magnitude of the scattering vector is given by

$$q = n\frac{2\pi}{d}. \tag{2.12}$$

Differential scattering cross section

This section will focus on the results by Squires [84] without the detailed derivations. λ goes to λ' and $\boldsymbol{k}$ goes to $\boldsymbol{k}$' when a neutron beam interacts with a sample. The scattered neutrons are a measure of the cross section. The differential scattering cross section describes the number of neutrons which are scattered into a solid angle, $d\Omega$, per second divided by the incident neutron flux, and is given by

$$\left(\frac{d\sigma}{d\Omega}\right)_{\lambda\rightarrow\lambda'} = \frac{1}{\phi}\frac{1}{d\Omega}\sum_{k' \text{ in } d\Omega} W_{\boldsymbol{k},\lambda\rightarrow\boldsymbol{k}',\lambda'}. \tag{2.13}$$

Here ϕ is the neutron flux and $W_{\boldsymbol{k},\lambda\rightarrow\boldsymbol{k}',\lambda'}$ is the number of transitions per second from the state $\boldsymbol{k}$, λ to $\boldsymbol{k}$', λ'. Fermi's golden rule, a fundamental result in quantum mechanics, can be used to evaluate the right hand side of the equation 2.13:

$$\sum_{k' \text{ in } d\Omega} W_{\boldsymbol{k},\lambda\to\boldsymbol{k}',\lambda'} = \frac{2\pi}{\hbar}\rho_{\boldsymbol{k'}} \mid \langle \boldsymbol{k'}\lambda' \mid V \mid \boldsymbol{k}\lambda\rangle \mid^2 \tag{2.14}$$

where $\rho_{\boldsymbol{k'}}$ is the number of momentum states in the solid angle $d\Omega$ per unit energy range for neutrons in the state $\boldsymbol{k'}$. The matrix element on the right hand side of equation 2.14 is given by

$$\langle \boldsymbol{k'}\lambda' \mid V \mid \boldsymbol{k}\lambda\rangle = \int \psi^*_{\boldsymbol{k'}}\chi^*_{\lambda'} V \psi_{\boldsymbol{k}}\chi_\lambda d\boldsymbol{R} d\boldsymbol{r}. \tag{2.15}$$

$$d\boldsymbol{R} = d\boldsymbol{R}_1 d\boldsymbol{R}_2 ... d\boldsymbol{R}_N \tag{2.16}$$

where $d\boldsymbol{R}_i$ is the elemental volume for the ith nucleus, and $d\boldsymbol{r}$ represents an element of volume for the neutron. Assuming that neutrons can be described by plane waves, we can say that

$$\langle \boldsymbol{k} \mid = e^{i\boldsymbol{k}\cdot\boldsymbol{r}}. \tag{2.17}$$

By substituting equation 2.17 into equation 2.14, and then substitute this into 2.13, we get

$$\frac{d\sigma}{d\Omega} = \left(\frac{m_n}{2\pi\hbar^2}\right)^2 \left| \int e^{-i\boldsymbol{k}'\cdot\boldsymbol{r}} V(r) e^{i\boldsymbol{k}\cdot\boldsymbol{r}} dr \right|^2 \tag{2.18}$$

where m_n is the neutron mass. As we are only considering elastic scattering, the system does not incur any changes and therefore there is only a change to the neutron wavefunction. N scattering centers at positions $\boldsymbol{R}_i$ with equal potential, V, gives a total potential of

$$V(r) = \sum_i^N V(r - \boldsymbol{R}_i). \tag{2.19}$$

Therefore we can now write the differential cross section as

$$\frac{d\sigma}{d\Omega} = \left(\frac{m_n}{2\pi\hbar^2}\right)^2 \left| \int V(\boldsymbol{r'}) e^{i\boldsymbol{q}'\cdot\boldsymbol{r}} d\boldsymbol{r} \sum_i^N e^{i\boldsymbol{q}\cdot\boldsymbol{R}_i} \right|^2 \tag{2.20}$$

where $\boldsymbol{q}$ is the scattering vector defined earlier, and $\boldsymbol{r'}$ = $\boldsymbol{r}$ - $\boldsymbol{R}_i$.

The differential scattering cross section is made up of two parts. The first is the structure factor,

$$S(\boldsymbol{q}) = \left|\sum_i^N e^{i\boldsymbol{q}\cdot\boldsymbol{R}_i}\right| \tag{2.21}$$

which describes the lattice ordering. The second part is the form factor given by

$$F(\boldsymbol{q}) = \frac{m_n}{2\pi\hbar^2}\int V(\boldsymbol{r'})e^{i\boldsymbol{q}\cdot\boldsymbol{r}}d\boldsymbol{r} \tag{2.22}$$

which is the Fourier transform of a single scattering potential. The following section will describe how small-angle neutron scattering (SANS) is used for scattering from the vortex lattice.

2.2 Small-Angle Neutron Scattering

SANS is a bulk technique where the vortex lattice is observed through the incident neutrons from the periodic array of vortices that make up the lattice. As mentioned in chapter 1, the vortices each contain one flux quantum per unit cell, so the spacing between lines is given by

$$d = \sqrt{\frac{\sigma\Phi_0}{B}} \tag{2.23}$$

where $\sigma = \frac{2}{\sqrt{3}}$ or 1 for a triangular or square lattice, respectively, as described in Chapter 1 (section 1.5). At high magnetic fields, as are often required to study the vortex lattice in many materials, this leads to a large d-spacing relative to the atomic spacing of the given crystal.

In a SANS experiment of the vortex lattice, the field is aligned parallel to the neutron beam - this defines the direction in which the vortices are formed. As mentioned, the differential scattering cross section is made up of the structure factor and the form factor:

$$\frac{d\sigma}{d\Omega} = F(\boldsymbol{q})^2 S(\boldsymbol{q}). \tag{2.24}$$

The scattering potential is given by

$$V(\boldsymbol{r}) = \mu_n \gamma B(\boldsymbol{r}), \tag{2.25}$$

where γ (=1.9) is the neutron gyromagnetic ratio and $B(\boldsymbol{r})$ is the local field distribution as a function of the radial distance $\boldsymbol{r}$. Therefore the differential scattering cross section can be written as

$$\frac{d\sigma}{d\Omega} = \left(\frac{m_n}{2\pi\hbar^2}\right)^2 \gamma^2 \mu_N^2 \frac{1}{\Phi_0} \mid \int B(\boldsymbol{r}) e^{i\boldsymbol{q}\cdot\boldsymbol{r}} d\boldsymbol{r} \mid^2 . \tag{2.26}$$

The structure factor exhibits δ functions at the locations of the vortices (assuming that the vortices behave as “ideal rods”), such that the structure factor is given by

$$S(\boldsymbol{q}) \propto \sum \delta(\boldsymbol{q} - \boldsymbol{G}) \tag{2.27}$$

where $\boldsymbol{G}$ is the reciprocal lattice vector. Equation 2.27 implies that scattering only occurs when $\boldsymbol{q} = \boldsymbol{G}$. If we express the form factor as $F_{\boldsymbol{G}}$, the differential scattering cross section becomes

$$\frac{d\sigma}{d\Omega} = \left(\frac{\gamma}{4}\right)^2 \sum_{\boldsymbol{G}} \mid F_{\boldsymbol{G}} \mid \delta(\boldsymbol{q} - \boldsymbol{G}). \tag{2.28}$$

It is worth noting that the incoherent scattering has been neglected here. Whilst the coherent scattering contains information on collective effects amongst the scattering entities such as Bragg scattering, the incoherent contribution yields information on the individual particle motion due to fluctuations, diffusion or isotope variations. Unlike coherent scattering, incoherent scattering is isotropic in $\boldsymbol{q}$. We are able to neglect the incoherent scattering because care is taken to make sure that anything that is positioned in the neutron beam is constructed from a material with low absorption and low incoherent scattering cross-section such as pure aluminium, and should be as free as possible from defects which can give rise to significant small-angle scattering. All experiments in this thesis used Cytop ® as the adhesive in the beam as it does not contain hydrogen. This is because hydrogen has a very high incoherent scattering cross-section. Therefore, neglecting the incoherent scattering in our analysis should not have a significant effect on our results.

2.3 Christen Equation

What is measured is not actually the differential scattering cross section but, instead, the integrated intensity, $I_{h,k}$, of the diffracted neutrons as the sample is "rocked" through the appropriate angular range. The relationship between the integrated intensity and the form factor is given by [19]:

$$I_{h,k} = 2\pi\phi V \left(\frac{\gamma}{4}\right)^2 \frac{\lambda_n^2}{\Phi_0 G_{h,k}} \mid F_{\boldsymbol{G}} \mid^2 \tag{2.29}$$

where ϕ is the incident neutron flux, V is the volume of the measured sample, λ_n is the wavelength of the neutron. With the Lorentz-factor correction, this becomes

$$I_{h,k} = 2\pi\phi V \left(\frac{\gamma}{4}\right)^2 \frac{\lambda_n^2}{\Phi_0 G_{h,k} cos(\zeta)} \mid F_{\boldsymbol{G}} \mid^2 \tag{2.30}$$

where $\cos(\zeta)$ is the Lorentz-factor. The Lorentz angle, ζ, is the angle between the Bragg spot at the position of the vortice and the direction normal to the direction of the angular rotation. The form factor $F_{\boldsymbol{G}}$ describes the spatial variation of the magnetic field within the vortice.

2.4 Instrumentation

Small-angle neutron scattering (SANS) can be used in a number of scientific areas, however this section will focus on SANS instrumentation for the measurement of the vortex lattice in superconductors. Neutrons are delivered from a source to the sample (vortex lattice) at which point they experience Bragg scattering and the scattered neutrons are picked up by a position sensitive detector to image the vortex lattice in reciprocal space. To

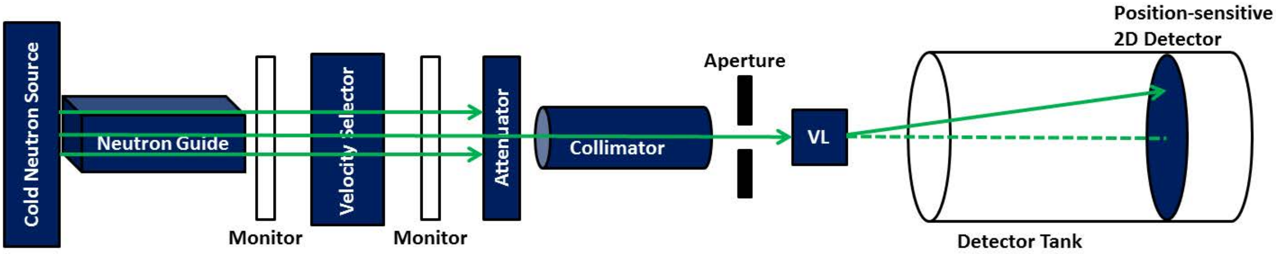

Figure 2.2: Schematic diagram of a typical SANS instrument.

envisage the vortex lattice in real space, the image can be rotated by 90°.

The neutron source can be either a reactor or a spallation source. To allow only neutrons of a particular wavelength, a velocity selector is used - this is a device to only allow neutrons of a particular velocity to pass through to produce a monochromatic beam. Typically the spread in wavelength is 10%. There are some cases where the neutron beam intensity requires damping, in this case an attenuator can be put into place via a rotatable disk with various apertures. A neutron monitor is used for normalisation as the neutron flux is often not entirely stable even at reactor sources. Neutron guides are used to lead the neutrons from the source to the collimator. The collimator length can be adjusted depending on the required flux and necessary resolution as an increased collimation reduces both the beam divergence and the neutron flux. The size of the beam on the sample is determined by an adjustable aperture that the neutrons must pass through prior to entering the sample. In order for the sample to exhibit the vortices, a suitably large magnetic field must be applied at a temperature below the superconducting transition temperature T_c. The scattered neutrons are registered by a position sensitive 2D detector within a detector tank. The distance between the sample and the detector should ideally be the same at the collimation length. A schematic of the arrangement of a typical SANS instrument is shown in figure 2.2.

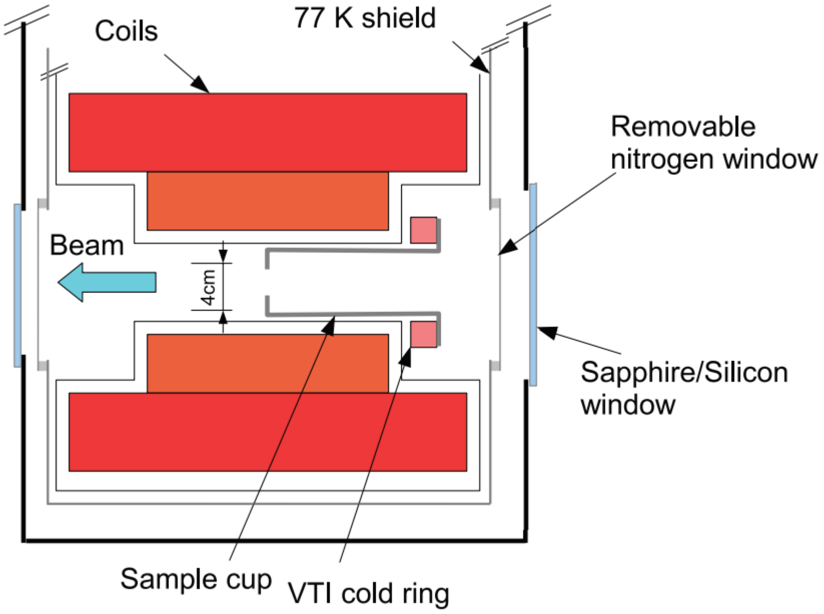

Figure 2.3: Schematic side view cross section of the 17 T magnet bore. Figure from [42].

2.5 Sample Environment

Huge advances in sample environments have allowed technically difficult experiments to be undertaken in this thesis. As mentioned in the previous section, in order to induce the vortex lattice state the sample must be below the superconducting transition temperature T_C and at a magnetic field between the lower critical field H_{C1} and the upper critical field H_{C2}. This requires the sample to be placed within a cryomagnet with windows that are transparent to neutrons.

2.5.1 17 TF

For the experiment on $CeCu_2Si_2$ the Birmingham 17 T horizontal cryomagnet [42] with a newly-built dilution insert was used. The dilution insert allows the sample to be cooled down to approximately 50 mK. An advantage of having a horizontal magnet is that there is very low background scattering due to the small amount of obstructions in the neutron beam path as shown in figure 2.3.

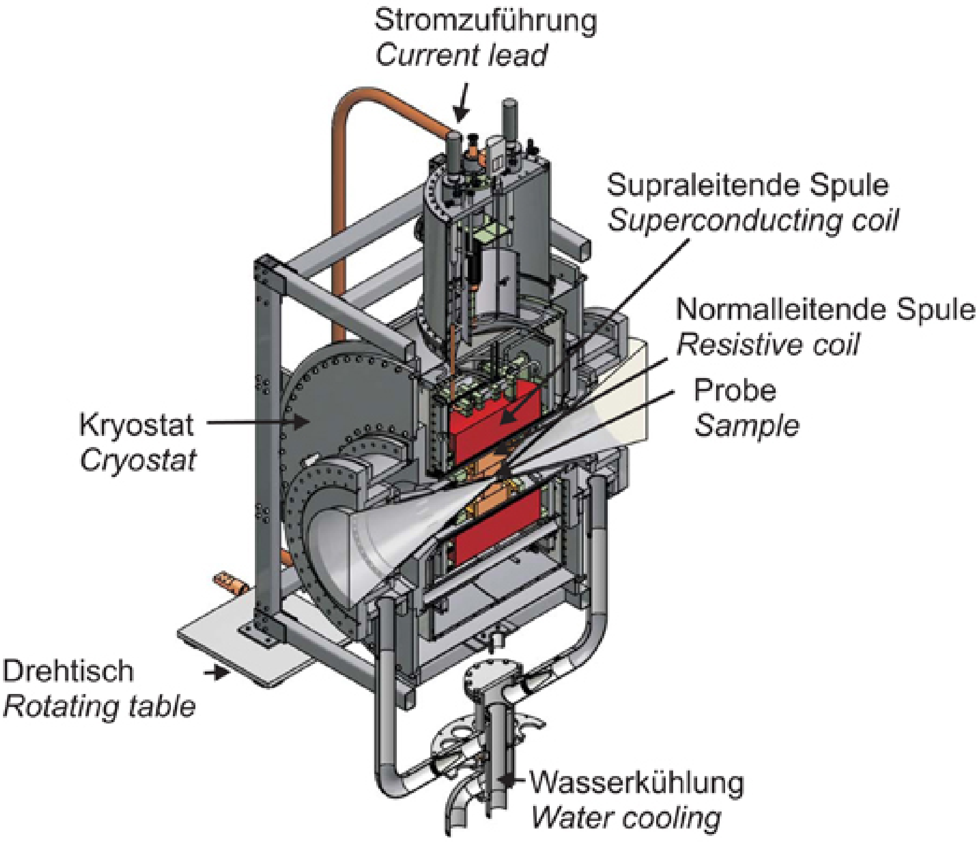

Figure 2.4: Cut-away view of the HFM at Helmholtz-Zentrum Berlin. (From *http : //www.helmholtz − berlin.de/quellen/ber/hfm/hfm/aufbau/index_en.html*).

2.5.2 High Field Magnet at HZB

For the $YBa_2Cu_3O_7$ measurements, we needed to measure the vortex lattice at the highest available continuous magnetic field available at a neutron source. This meant using the newly built High Field Magnet (HFM) at Helmholtz-Zentrum, Berlin. The magnetic field is generated by both superconducting and resistive coils. The combination of the two means that this hybrid magnet system generates a total of 26 T. The cryostat allows the sample to be cooled down to 2 K.

The magnetic field is horizontal so there are 30° conical openings at both ends for the neutron scattering access. This allows the sample to be rotated about its vertical axis by ± 15°.

2.5.3 Sample Requirements

Along with the sample environment, the sample itself needs to be suited for a SANS experiment of the vortex lattice. The sample must be aligned such that the axis to which the vortices are pinned to is parallel to the both the field and the beam direction.

Typically a sample should scatter approximately 10% of the neutron beam. If it is much less than this the count rate will likely be too small and if it is much higher multiple scattering can become an issue. Some materials which can be problematic are strong neutron absorbers due to their large absorption cross sections such as gadolinium and boron, although these make good materials for neutron detectors and for neutron shielding.

2.6 Preparation of the Vortex Lattice

The usual method of preparing the vortex lattice is by cooling the superconductor through the superconducting transition temperature, T_C, in an applied field between H_{C1} and H_{C2}. However, due to the competition between pinning and the Meissner effect (expulsion of flux), this method achieves a poor approximation to the actual equilibrium. This poses a problem as the vortex lattice must be in a well ordered periodic arrangement in order to image it via small-angle neutron scattering to result in clear Bragg peaks. A method used to overcome this is to oscillate the applied field as the superconductor is cooled below T_C which promotes the vortex lattice to arrange periodically in a way that is closer to the actual equilibrium. The optimum magnitude of the oscillation depends on the particular superconductor being cooled, although it is often between 0.1 - 5% of the final applied field based on our previous experiences measuring the vortex lattice is various superconductors.

2.7 Experimental Procedure

Firstly, the sample is mounted such that it is precisely in the centre of magnet. Then the sample can be cooled to below T_C and a field between the lower and upper critical field can be applied. The sample can be located by placing a neutron camera in the beam or by translating the cryomagnetic relative to the neutron beam, in directions perpendicular to the neutron beam. Once the sample is located, the beam stop can be adjusted to block the direct beam in order to protect the detector. Depending on the precise magnetic field applied to the sample, several beam parameters need to be adjusted such as the collimation, detector distance and the neutron wavelength. For example, at high fields you will increase the detector distance and/or decrease the neutron wavelength as the vortex lines are moving closer together, so they will appear further apart on the detector in q-space. For each set of parameters, three measurements are required: (i) direct beam whereby one has an attenuated beam with the beam stop removed to provide a measure of the neutron flux, (ii) background measurement and (iii) foreground measurement. Once the system is cooled below the superconducting transition temperature, you can begin to undertake the foreground measurement. This entails performing a rocking scan whereby one changes the direction of the magnet and sample with respect to the incident neutron beam. This change results in an optimisation of a Bragg peak for a certain angle of rotation. The background measurements are done in the same way but in the normal state. The normal state can be induced by either removing the field or warming the sample above T_C.

2.8 Time-of-Flight for Vortex Lattice Measurements

Although the neutron source at Helmholtz-Zentrum Berlin is a continuous reactor source, the EXED (EXtreme Environment Diffractometer) [96] instrument uses a polychromatic time-of-flight technique. Most reactor sources use a monochromatic neutron beam to make the most of the high time averaged neutron flux. However, due to the restricted scattering angle for EXED in conjunction with the high field magnet, it is not possible to scan over a range of scattering angles to cover the requested scattering length according to Bragg's law with a single wavelength neutron beam [96]. A polychromatic beam compensates for limited angle.

The use of time-of-flight techniques allow the optimal use of white neutron beams. From de Broglie's relationship we know that neutrons with different energies and wavelengths have different velocities, and since they are all created at the same time in a pulse the higher energy (shorter wavelength) neutrons enter the detector sooner than the lower energy (longer wavelength) neutrons. We know, from the neutron's time of arrival at the detector (and the flightpath), the velocity, and therefore, the wavelength of each scattered neutron which reaches the detector. The wavelength and time-of-flight are related by

$$\lambda_n = \frac{ht}{m_n L} \tag{2.31}$$

where t is the time taken for the neutron to reach the detector since its creation (time-of-flight), m_n is the neutron mass, and L is the distance travelled by the neutron (flight path).

In time-of-flight mode, the wavelength spread arising from the pulse and the channel widths can be negligible [73]. Also, the large wavelength range in time-of-flight experiments gives a better resolution by scattering to higher angles. An experimental benefit of using time-of-flight for studying the vortex lattice is that it that there is no requirement to rock the sample through the Bragg conditions as λ is continuously tuned. One disadvantage of the time-of-flight method is that, at longer wavelengths, the neutron flux is low due to the Maxwellian spectrum.

2.9 Data Visualisation and Analysis

The results on which this thesis is based are from small-angle neutron scattering experiments. The data is taken by measuring the intensity at particular pixels on the detector for a given time. In order to analyse the the monochromatic SANS data, a program called GRASP was used. For the time-of-flight measurements MANTID was used.

2.9.1 GRASP

GRASP is a Matlab$^{\mathrm{TM}}$ script application of the ILL, Grenoble [22]. It is designed for the analysis and reduction of data produced by single-wavelength SANS instruments. It deals with the procedures required for analysis of 2D multidetector data such as being able to quickly extract the scattered intensity as a function of the detector position. The intensity can also be extracted a function of the sample environment conditions such as temperature, field, and rocking curve.

Bayesian Method to improve SANS analysis

A new method using Bayesian statistics was developed by A. T. Holmes to analyse SANS data from vortex lattices [41]. It allows for a significant increase in the signal-to-noise ratio. By taking into account that all scattering is centered on a plane in reciprocal space the Lorentz factor correction can be incorporated naturally. The GRASP application is used to process and display the data.

2.9.2 Extracting the integrated intensity in GRASP

This section will briefly outline how GRASP is used to extract the integrated intensity from the rocking curve which results from a Bragg peak. This also serves as a manual for new users of this data analysis method.

Firstly, the foreground and background data files, known as numors, are entered, as shown in figure 2.5. The background is then subtracted from the foreground leaving only the vortex lattice signal, as shown in figure 2.6. Strictly speaking, the background subtraction is not necessary to extract the vortex lattice form factor from the rocking curves. It is only strictly necessary when studying the vortex lattice structure in detail as the relative spot positions are more difficult to determine without a background subtraction. By subtracting the background from the foreground, we are unnecessarily combining the background errors to the foreground errors, so in the case that we want only to extract the vortex lattice form factor, we need not subtract the background (assuming that we know the precise location of the vortex lattice spots). Using the "zoom-in" feature at the top of the window, a box can be drawn around any particular region of interest - here shown as a box around a vortex lattice Bragg spot. The boxes window, as shown in figure 2.7, is opened from the "Analysis" drop-down menu and allows the user to select the precise size of the box. Once this is decided, the "Do it!" button plots a graph of the box counts as a function of the rocking angle, as shown in figure 2.8. The rocking curve is fitted with a Gaussian line-shape, and the fit is shown in figure 2.9, and the parameter values can then be extracted, including the integrated intensity, the centre position of the Bragg peak and the full-with at half-maximum (FWHM).

Using the integrated intensity, we can find the vortex lattice form factor by using the Christen equation. This can be averaged for all of the first order vortex lattice spots to find the average form factor at that particular field and temperature. Each Bragg spot may not have the same intensity as the others if the magnet is not correctly aligned to the beam and/or the sample, hence the need to find the average vortex lattice form factor over all of the spots. Therefore, it is important to choose the same box size for each spot so that each spot has an approximately equal size of signal-to-background ratio. A box is generally regarded as too big if the background intensity, as a function of rocking angle, is more than 20% of that of the vortex lattice peak intensity. A box is too small if the FWHM of the peak intensity appears in only a very narrow range of rocking angles compared to the estimated FWHM given by the "FLL calculator" in GRASP.

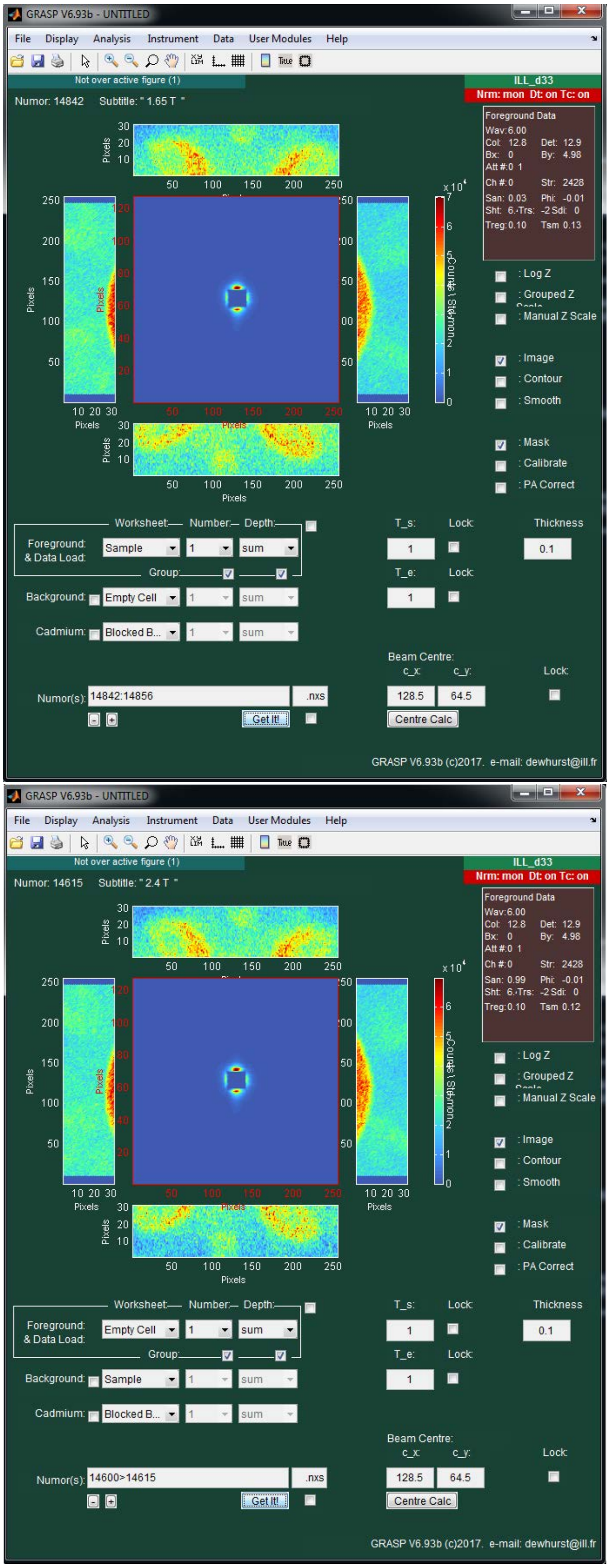

Nrm: mon Dt: on Tc: on

Numor: 14842 Subtitle: " 1.65 T "

Foreground Data
Wav: 6.00
Col: 12.8 Det: 12.9
Bx: 0 By: 4.98
Att #: 0 1
Ch #: 0 Str: 2428
San: 0.03 Phi: -0.01
Sht: 6.4 Trs: -2 Sdi: 0
Treg: 0.10 Tsm 0.13

☐ : Log Z
☐ : Grouped Z Scale
☐ : Manual Z Scale
☑ : Image
☐ : Contour
☐ : Smooth
☑ : Mask
☐ : Calibrate
☐ : PA Correct

	Worksheet	Number	Depth ☐
Foreground & Data Load:	Sample	1	sum
Group:		☑	☑
Background: ☐	Empty Cell	1	sum
Cadmium: ☐	Blocked B...	1	sum

T_s: 1 Lock: ☐
T_e: 1 Lock: ☐
Thickness: 0.1

Beam Centre: c_x: 128.5 c_y: 64.5 Lock: ☐

Numor(s): 14842:14856 .nxs

Nrm: mon Dt: on Tc: on

Numor: 14615 Subtitle: " 2.4 T "

Foreground Data
Wav: 6.00
Col: 12.8 Det: 12.9
Bx: 0 By: 4.98
Att #: 0 1
Ch #: 0 Str: 2428
San: 0.99 Phi: -0.01
Sht: 6.4 Trs: -2 Sdi: 0
Treg: 0.10 Tsm 0.12

☐ : Log Z
☐ : Grouped Z Scale
☐ : Manual Z Scale
☑ : Image
☐ : Contour
☐ : Smooth
☑ : Mask
☐ : Calibrate
☐ : PA Correct

	Worksheet	Number	Depth ☐
Foreground & Data Load:	Empty Cell	1	sum
Group:		☑	☑
Background: ☐	Sample	1	sum
Cadmium: ☐	Blocked B...	1	sum

T_s: 1 Lock: ☐
T_e: 1 Lock: ☐
Thickness: 0.1

Beam Centre: c_x: 128.5 c_y: 64.5 Lock: ☐

Numor(s): 14600>14615 .nxs

Figure 2.5: The GRASP window. The top shows the entry of the foreground data files and the bottom shows the entry of the background data files.

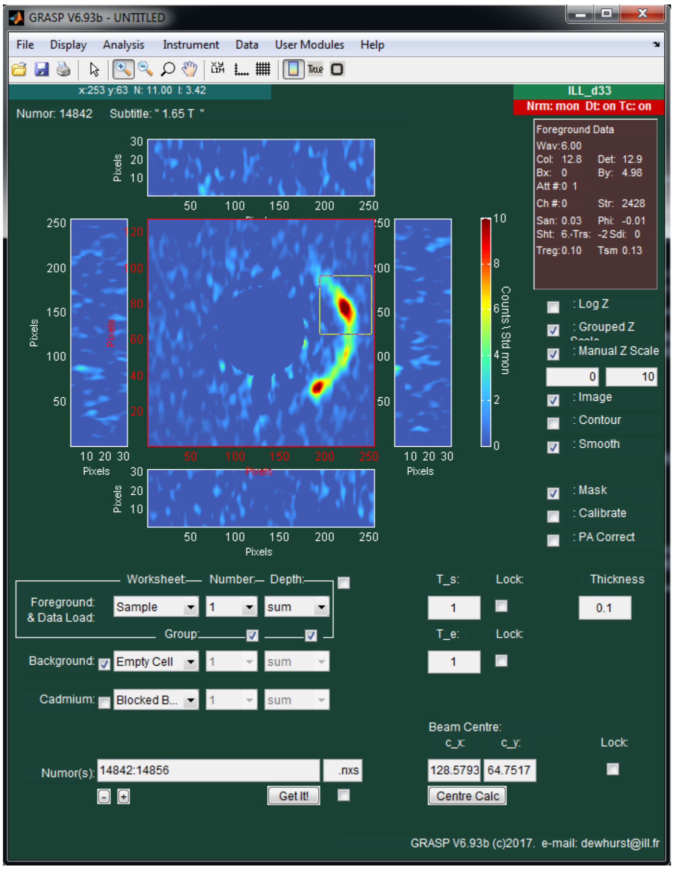

Numor: 14842 Subtitle: " 1.65 T "

Foreground Data
Wav:6.00
Col: 12.8 Det: 12.9
Bx: 0 By: 4.98
Att #:0 1
Ch #:0 Str: 2428
San: 0.03 Phi: -0.01
Sht: 6.·Trs: -2 Sdi: 0
Treg:0.10 Tsm 0.13

☐ : Log Z
☑ : Grouped Z Scale
☑ : Manual Z Scale
0 10
☑ : Image
☐ : Contour
☑ : Smooth
☑ : Mask
☐ : Calibrate
☐ : PA Correct

Foreground: & Data Load: Worksheet: Sample Number: 1 Depth: sum ☐
Group: ☑ ☑
Background: ☑ Empty Cell 1 sum
Cadmium: ☐ Blocked B... 1 sum
Numor(s): 14842:14856 .nxs
- + Get It! ☐

T_s: 1 Lock: ☐
T_e: 1 Lock: ☐
Thickness 0.1
Beam Centre: c_x: 128.5793 c_y: 64.7517 Lock: ☐
Centre Calc

GRASP V6.93b (c)2017. e-mail: dewhurst@ill.fr

Figure 2.6: The resulting vortex lattice after the background is subtracted from the foreground. A box is drawn around one of the Bragg spots to extract the intensity for this specific part of the detector as a function of rocking angle.

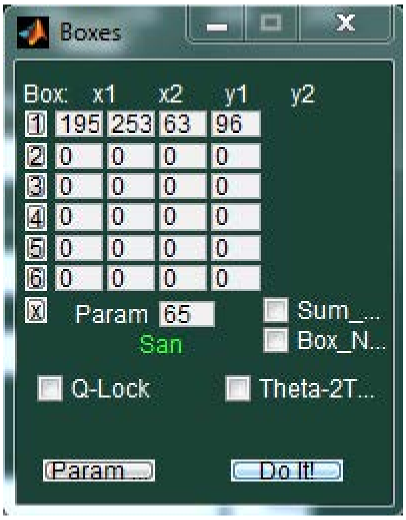

Box:	x1	x2	y1	y2
1	195	253	63	96
2	0	0	0	0
3	0	0	0	0
4	0	0	0	0
5	0	0	0	0
6	0	0	0	0

☒ Param 65 San
☐ Sum_...
☐ Box_N...
☐ Q-Lock
☐ Theta-2T...

Figure 2.7: Boxes window. This is used to select the precise box size to capture the region of interest. By pressing “Do it!” a graph of the intensity as a function of rocking angle is produced.

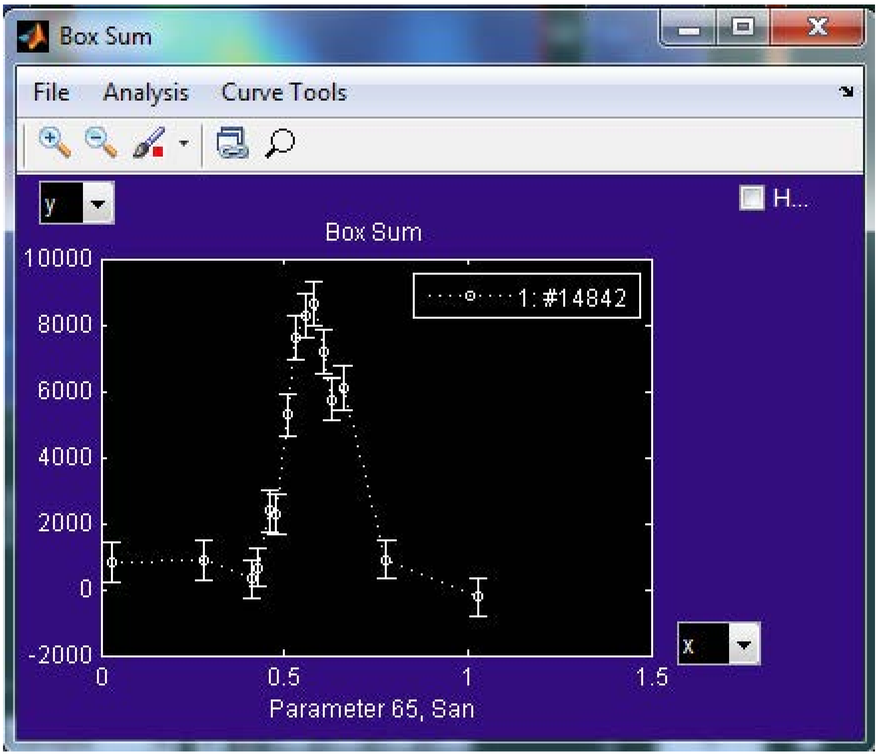

Figure 2.8: Graph showing the intensity as a function of rocking angle (San).

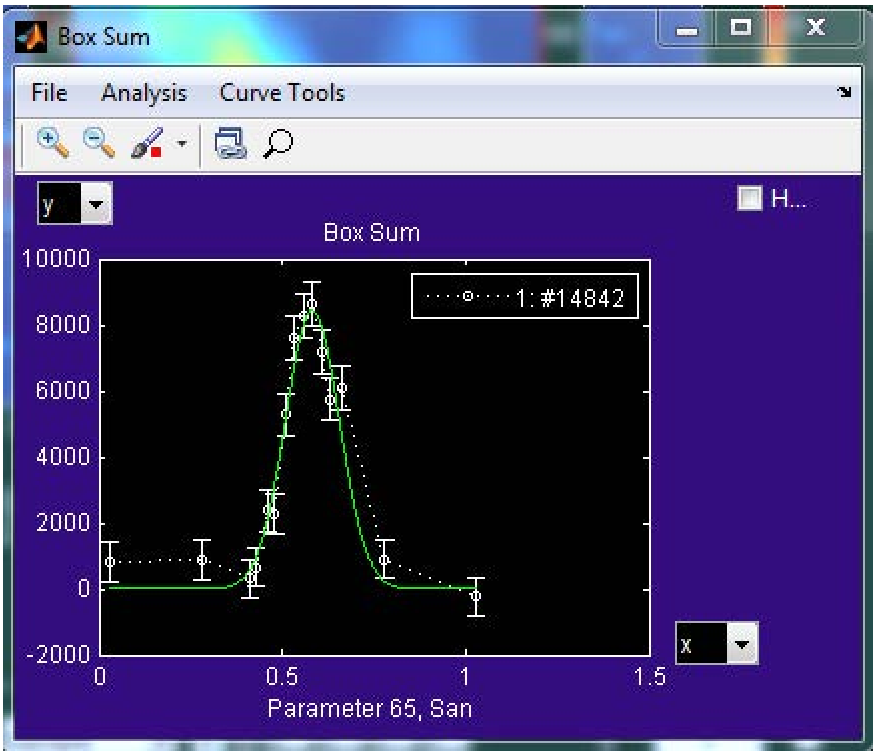

Figure 2.9: Graph showing the intensity as a function of rocking angle fitted to a Gaussian line shape to extract the integrated intensity.

2.9.3 MANTID

Mantid is a data analysis and visualisation package for neutron scattering experiments [5]. It was used for the time-of-flight data in this thesis. We normally use a monochromatic neutron beam when studying the vortex lattice, however for the experiment on YBCO we used the time-of-flight technique as this instrument (EXED) allowed us the potential of studying the vortex lattice up to 25 T. GRASP can only be used for a monochromatic neutron beam, so it could not be employed for analysing the time-of-flight data produced by EXED. Analysing the vortex lattice data produced by a time-of-flight instrument proved challenging at the initial stages of the data analysis. Mantid offers an extensible framework, through Python, for data manipulation. It is common for time-of-flight instruments to have 10^5 n cm^{-1} s^{-1} and 10^6 pixels which generates very large data files. The EXED instrument at Helmholtz-Zentrum Berlin usually collects data in "event mode" which lists every neutron with a collection time and other metadata - this makes filtering the data easier and allows us to use the metadata to create data subsets. Our experiment did not run full event mode, but instead used pre-binning.

2.9.4 Extracting the form factor in Mantid

Unlike GRASP, Mantid was not designed with measuring the vortex lattice of superconductors in mind. Therefore the procedure to extract useful information, such the vortex lattice form factor, is less obvious. The background is subtracted from the foreground in the Python script editor in Mantid. The resulting vortex lattice is shown in figure 2.10. Similarly to GRASP, a box can be drawn around the vortex lattice spots, however the integrated intensity cannot be determined at this stage. The boxes are used to determine the q_x and q_y positions of the Bragg spots, as shown in figure 2.11. Based on the values of q_x and q_y at the vortex lattice spot, we select a box encapsulating the spot in the q_{xy} plane as the region of interest where we extract the intensity as a function of q_z. This way we only measure the intensity in q_z within the region q_{x-min} to q_{x-max} and q_{y-min} to q_{y-max}.

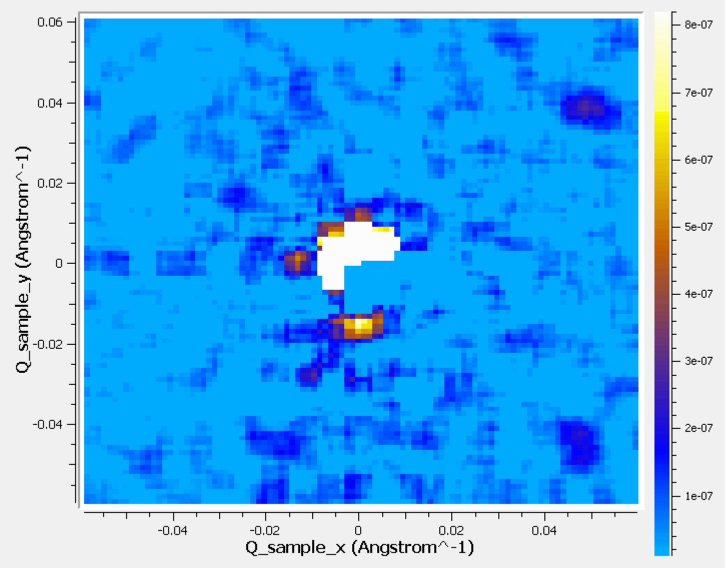

Figure 2.10: The vortex lattice shown in q-space in the Mantid slice viewer. The two Bragg spots are shown on the right. This image is generated from a user-made script in python.

Without doing this we would take the intensity of q_z across the q_{xy} plane which would make it impossible to compare the intensity, and therefore vortex lattice form factor, between the different vortex lattice spots of a single diffraction pattern. This information is input into the Python script in Mantid, and the q_z data is analysed in the selected region. The intensity as a function of q_z can then be plotted and fitted to a Gaussian or a Lorentzian to determine the integrated intensity, as shown in figure 2.12. A modified version of the Christen equation is employed to extract the vortex lattice form factor from this. The modification to the Christen equation is explained in our results in chapter 3. We initially had some issues with extracting the form factor from the time-of-flight data as we were only "summing" the intensities in the q_z direction initially. Later, as described in chapter 3, we then summed the intensity in the q_x. q_y and q_z directions.

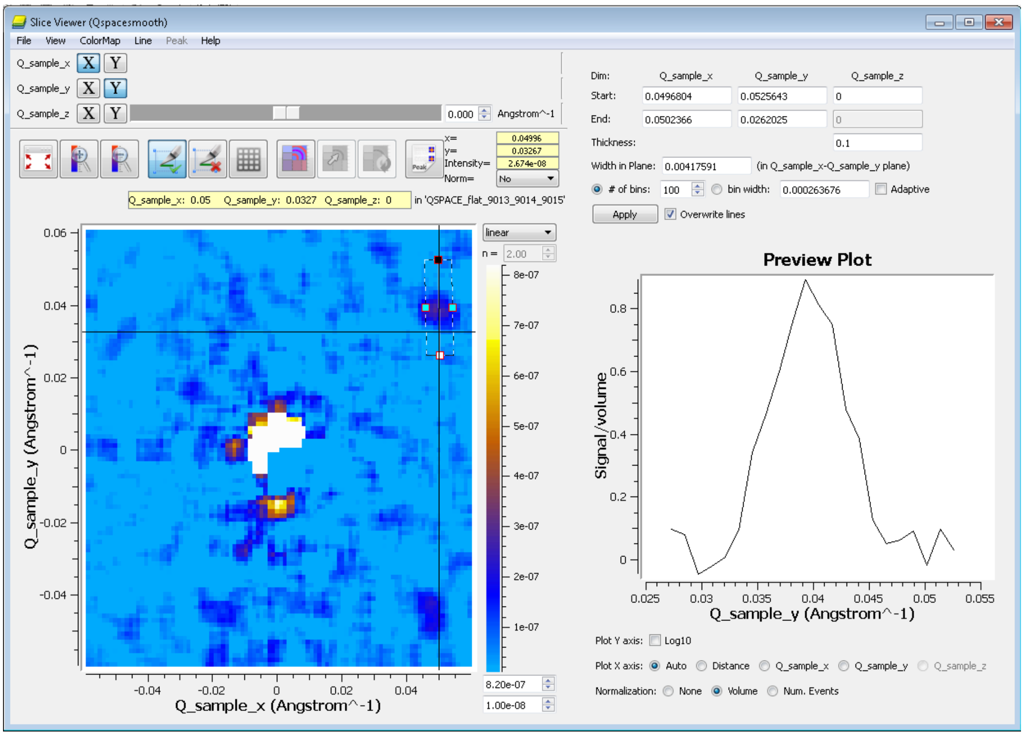

Q_sample_z: 0.000 Angstrom^-1

x= 0.04996
y= 0.03267
Intensity= 2.674e-08
Norm= No

Q_sample_x: 0.05 Q_sample_y: 0.0327 Q_sample_z: 0 in 'QSPACE_flat_9013_9014_9015'

linear
n = 2.00
8.20e-07
1.00e-08

Dim:	Q_sample_x	Q_sample_y	Q_sample_z
Start:	0.0496804	0.0525643	0
End:	0.0502366	0.0262025	0
Thickness:			0.1

Width in Plane: 0.00417591 (in Q_sample_x-Q_sample_y plane)

● # of bins: 100 ○ bin width: 0.000263676 ☐ Adaptive

☑ Overwrite lines

Plot Y axis: ☐ Log10

Plot X axis: ● Auto ○ Distance ○ Q_sample_x ○ Q_sample_y ○ Q_sample_z

Normalization: ○ None ● Volume ○ Num. Events

Figure 2.11: Boxes can be drawn around the Bragg spots in the Mantid slice viewer to determine the positions of the vortex lattice in q-space.

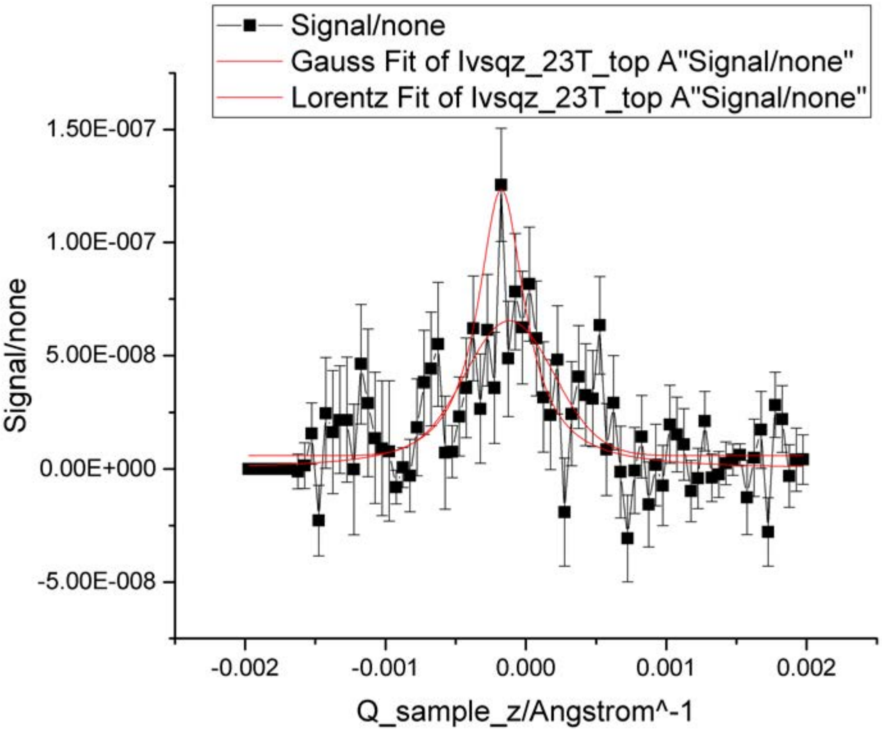

Figure 2.12: The intensity (neutron counts) as a function of q_z fitted to both a Gaussian and Lorentzian lineshape. The area under the curve represents the integrated intensity.

Chapter 3

Vortex Lattice in $YBa_2Cu_3O_7$

3.1 Introduction

The so-called high T_C superconductors first manifested in the form of $(La_{1-x}Ba_x)CuO_4$ [8] with a critical temperature of approximately 35 K. A year later, in 1987, superconductivity was shown to exist above the boiling point of liquid nitrogen (77 K) in $YBa_2Cu_3O_{7-\delta}$ (YBCO) [111] with a T_C up to 93 K depending on the composition. This chapter summarises the physical properties of YBCO and details the previous investigations that have been carried out over the years. Following this, the recent vortex lattice study will be presented.

3.2 Crystal Structure

The superconducting properties of $YBa_2Cu_3O_{7-\delta}$ are heavily dependent on the value of δ which can vary between 0 and 1 ($\delta = 1$ in the undoped parent compound). YBCO crystallises in a perovskite structure consisting of layers of yttrium, barium oxide, copper oxide or copper dioxide. The crystallographic a and b axes are identical for $\delta = 0$ making for a tetragonal structure with an occupancy of a single "free" electron per unit cell. The crystal structure of stoichiometric $YBa_2Cu_3O_7$ is shown in figure 3.1.

The cuprate family of superconductors have one thing in common - their copper-oxide

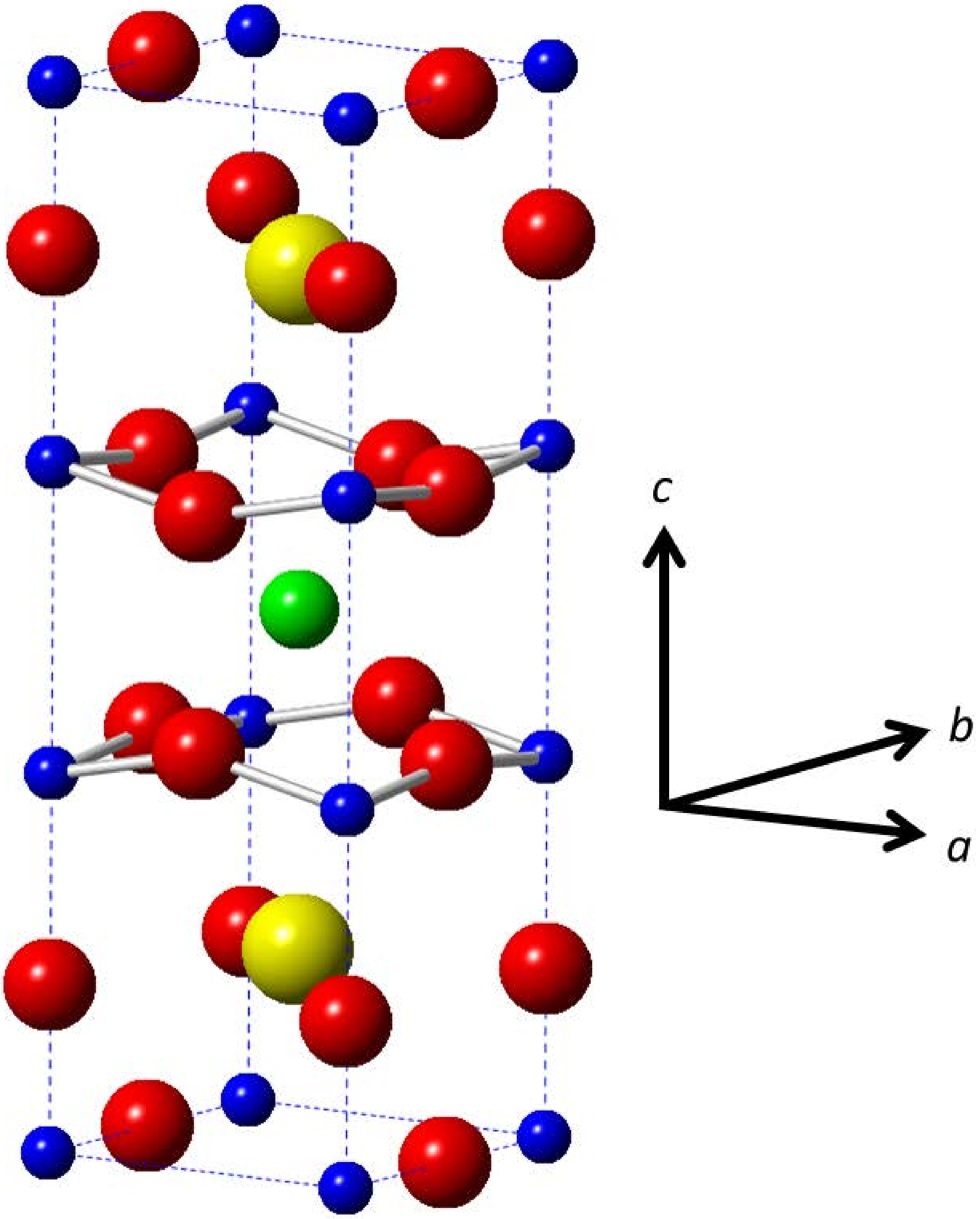

Figure 3.1: $YBa_2Cu_3O_7$ crystal structure. Copper is shown in blue, oxygen is shown in red, barium is yellow in purple and yttrium is shown in green. Lattice parameters: a = 11.68 Å , b = 3.887 Å , c = 3.823 Å .

(CuO_2) layers. A key feature of the YBCO unit cell is the two layers of CuO_2. It is widely agreed that the superconductivity takes place in these layers. What is noticeable in figure 3.1 is that the yttrium layer does not contain an oxygen atom. This is because the yttrium has a valence of 3+ whereas the barium has a valence of 2+, and the *bond sum rule* for charge balancing implies that each yttrium coordinates with eight oxygen atoms (with a valence of -2) in the planes above and below the yttrium plane [80].

Yttrium's role in the compound is simply to keep the two CuO_2 layers apart. The Y atom can be replaced by almost any of the lanthanides with little effect on the superconducting properties.

The two barium-oxygen (BaO) layers are above the upper CuO_2 layer and below the lower CuO_2 layer in the unit cell. In each BaO layer the barium atom is surrounded by four oxygen atoms at the unit cell edge. At the top and bottom of each unit cell lies the copper-oxide chain layer which has certain oxygen atoms missing when compared to the CuO_2 planes. The missing oxygens are imperative to understanding the crystal structure of $YBa_2Cu_3O_{7-\delta}$. A non-zero δ is an indicator that a fraction of the conventionally expected seven oxygens are missing. T_c is maximum at $\delta = 0.07$ (93 K), and for $\delta = 0.5$ the superconductivity is destroyed. Figure 3.1 shows the fully oxygenated crystal structure with seven oxygen atoms ($\delta = 0$). It can also be seen that the oxygens in the copper-oxide chain layers are only along the b direction. This results in the orthorhombic unit cell as the lattice parameters $a \neq b$. Oxygen vacancies appear as δ increases, and at $\delta = 0.5$ the vacancies have an equal chance of occurring along the a and b directions so the unit cell has a square symmetry and the lattice parameters $a = b$ creating a tetragonal structure.

Due to the mismatch between the lengths of the a- and b-axes of the unit cell (in fully-oxygenated $YBa_2Cu_3O_7$), the crystal lattice symmetry is broken. It is energetically easy, during the crystal growth process, for propagation to switch from a to b. The result of this is irregularities in the single crystal - this is known as crystal twinning [80].

Flux pinning is affected by twinning. An example of this is when vortices are perpendicular to the twin boundaries; this may inhibit the motion of the vortices. In the case where the vortices are parallel to the twin boundary direction, the vortices are able to move along the boundaries but cannot go across them.

3.3 YBCO temperature-doping Phase Diagram

When $\delta = 1$, the composition is $YBa_2Cu_3O_6$, and it is an antiferromagnetic Mott insulator. Increasing the oxygen content (decreasing δ) results in doping holes into the CuO_2 layers which induces superconductivity. In figure 3.2, it can be seen that as the hole concentration increases (and the oxygen content (given as “x” in the figure)), a superconducting dome emerges which has a maximum at a value of $T_C \approx 93$ K. At very high temperatures (above T_C), the material enters a *bad metal* regime where the properties are vastly different from those of regular *good* metals. Below T^* lies the pseudogap regime which is an ambiguously defined boundary between *bad metal* and an even more anomalous regime [35].

3.4 Previous Vortex Lattice Studies

The earliest experiments studying the vortex lattice in YBCO were Bitter decoration studies which provided a real space image of the vortex lattice at low fields [37, 23, 24]. It was shown that the vortex lattice had a hexagonal structure up to 17 mT. However Bitter decoration experiments were limited in that they were unable to probe the bulk of the sample. This section will focus on the key small-angle neutron scattering studies that have been carried out on YBCO since 1990.

3.4.1 Low Field SANS Studies

The first observation of the vortex lattice in a high-T_C superconductor by small-angle neutron scattering was carried out on a twinned YBCO sample [34]. With a field of 0.2 T

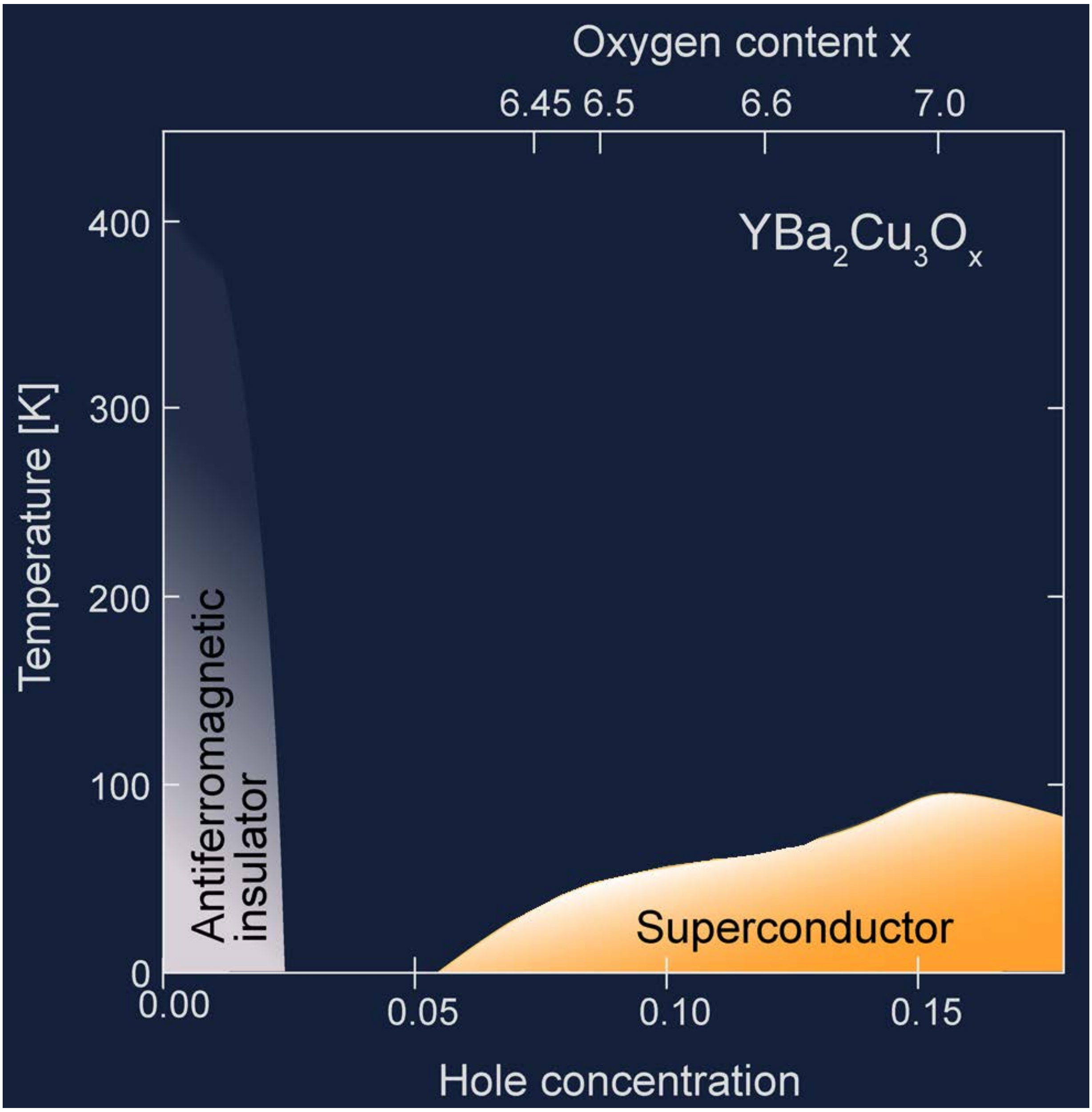

Figure 3.2: A schematic temperature-doping phase diagram of $YBa_2Cu_3O_x$. Figure reproduced from [17].

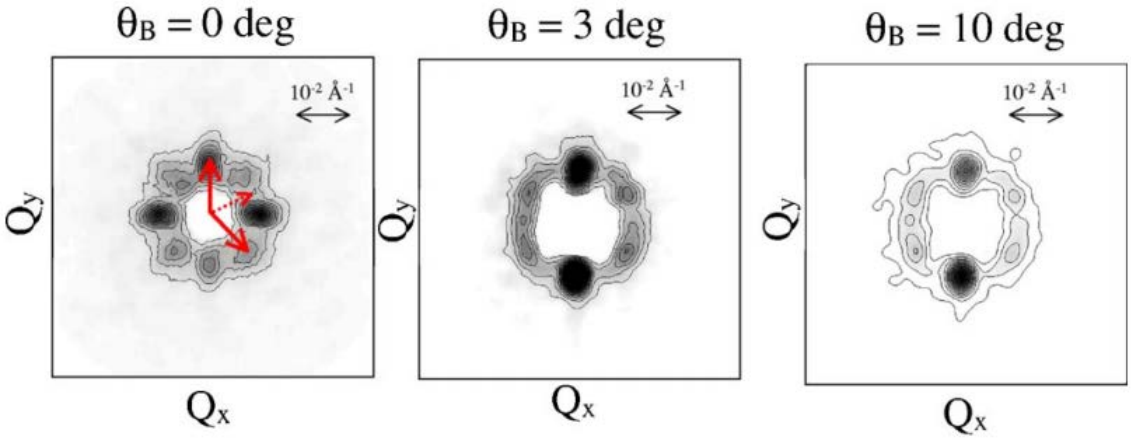

Figure 3.3: Diffraction patterns at 0.5 T and 4.2 K with the field at various critical angles θ_B. Figure reproduced from [83].

applied to the *c*-axis, and at a temperature of 20 K, the vortex lattice diffraction pattern showed that, due to flux pinning to the twin planes, a substantial fraction of the signal lay along the [1 1 0] direction. A later study by Yethiraj *et al.* [116], also on a twinned sample, showed that the influence of the twin boundaries can be inhibited by rotating the field away from *c*-axis. Further investigation by Simon *et al.* [83] found that the vortices became pinned to the twin planes if the angle between the field and the twin boundary direction was less than a critical angle ($\approx 10°$). This is shown in figure 3.3. Beyond this critical angle, a single vortex would follow a single twin plane but hop over to the next twin plane in order to keep the overall direction of the vortex parallel to the direction of the applied magnetic field.

The vortex lattice structure was studied up to 0.8 T in a twinned crystal by Yethiraj *et al.* [115]. The *c*-axis anisotropy, γ_{ac}, was found to be ≈ 4.5 which was in agreement with Bitter decoration values of the anisotropy. They also found, by rotating the field with respect to the crystal *c*-axis, that the vortex lattice anisotropy varies with the angle of induction.

Keimer *et al.* [51] studied the vortex lattice in a single crystal with a field of 0.5 T inclined at angles between 0 and 80° to the *c*-axis. Unlike the study by Yethiraj *et al.*, [116], they found that the vortex lattice remains triangular regardless of the angle between the field direction and the crystal c-axis, and for angles below 70° the vortex lattice orientation adjusts itself to maximise the pinning energy to the twin planes. At 80°, in the orientation predicted by anisotropic London theory, the vortex lattice consisted of independent chains.

A later study by Keimer *et al.* [52] extended the field range from 0.5 T to 5 T applied parallel to the c-axis. This study observed that the vortex lattice diffraction pattern remained largely unchanged. Keimer *et al.* claimed that the vortex lattice structure was made up of a superposition of four orientations of oblique lattice with two nearly equal lattice constants and an angle of 73° between primitive vectors. The authors attributed the stable vortex lattice structures to an increasing prominence of the gap anisotropy at high magnetic fields, implying a departure from the London regime. They argued that the Gibbs free energy, rather than pinning to twin boundaries, was responsible for the vortex lattice structure being composed of a superposition of hexagonal domains. This was shown to be incorrect by Forgan & Lee [33] who claimed that the vortex lattice structures observed by Keimer *et al.* were consistent with a vortex lattice structure comprising multiple hexagonal domains with the orientation of the domains determined by pinning to the twin boundaries.

A study by Johnson *et al.* [50] on an untwinned crystal, where the field was applied parallel to the c-axis, observed the diffraction spots which correspond to four orientations of a hexagonal lattice and are distorted by the a-b anisotropy. A value of the penetration depth ratio $\lambda_a/\lambda_b = 1.18$ was obtained. It was shown that for fields larger than the lower critical field, H_{C2}, the axial ratio of the ellipse of the diffraction pattern is equal to the penetration depth ratio. The diffraction spots lie in an elliptical ring as shown in figure 3.4 with the a axis vertical. The anisotropy is consistent with the increased supercurrent flow along the chain direction resulting in $\lambda_b < \lambda_a$. The value of $\lambda_{ab} = 1.18$ did not vary with field. The authors concluded that the chains in their crystals were disrupted by a small concentration of oxygen vacancies.

With the field applied parallel, or almost parallel, to the c-axis, the diffraction pattern

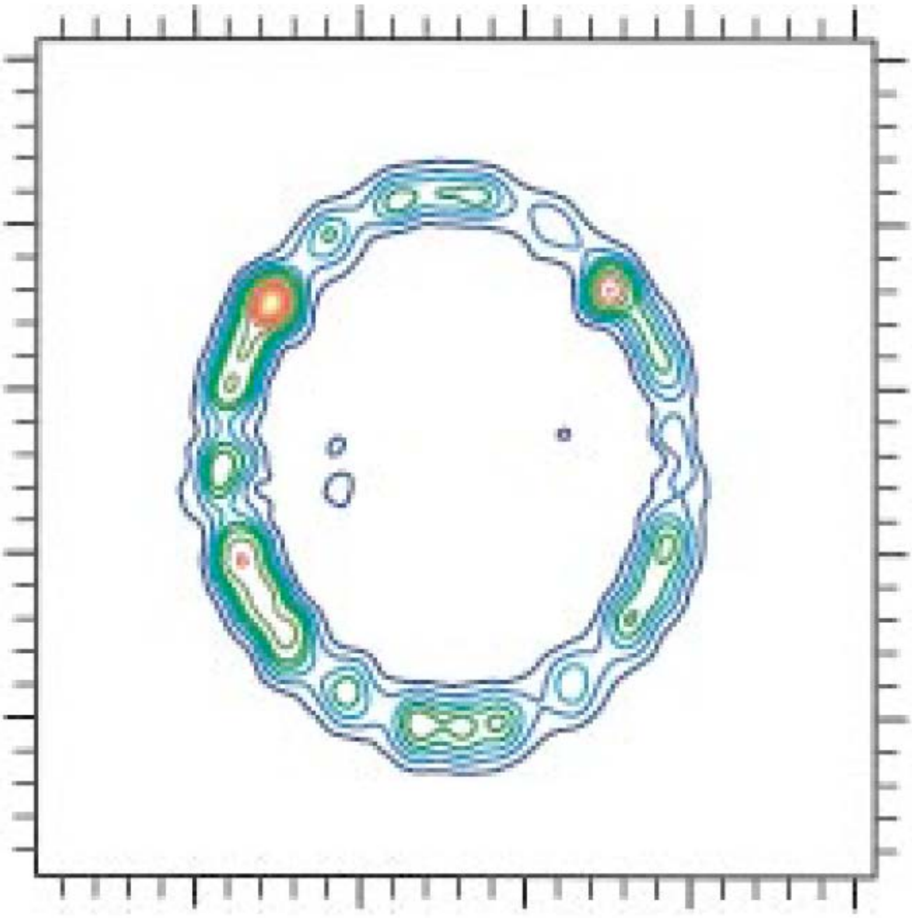

Figure 3.4: Diffraction pattern with 0.5 T applied parallel to the *c* axis. The elliptical nature of the ring is attributed to the penetration depth anisotropy. The *a*-axis is vertical in the figure. Figure reproduced from [50].

remained unchanged up to the maximum available field of 4 T. The anisotropy between the supercurrents along the crystal c-axis and the ab plane becomes important as the magnetic field is rotated by a large angle from c. This anisotropy, γ_c, mixes with the ab-anisotropy, γ_{ab}. If the b-axis is the vertical axis of rotation, the deviation from a ring is due to γ_c adding to γ_{ab} leading to a highly eccentric ellipse of scattering. However, when the a-axis is the vertical axis of rotation, diffraction spots from the two ab aligned vortex lattices remain, and the vortex lattice oriented with a becomes increasingly dominant as the angle of rotation is increased. The authors say that the difference between rotating about either the a- or b-axis is that the rotation about the b axis means the chains remain perpendicular to the field direction whereas the rotation about the a-axis changes the angle between the field and chain direction. However, by applying the magnetic field at an angle of 33° to the c-axis, the two anisotropies cancel and an undistorted hexagonal vortex lattice is observed. By increasing the applied field to above 3 T, the vortex lattice undergoes a 90° reorientation. The authors suggested this may be due to a field dependence to the mechanism that is controlling the vortex lattice orientation.

Simon *et al.* [83] studied the influence of the twin boundaries on the vortex lattice structure. They found that by increasing the angle of applied field to c, the vortices go from being aligned with the field to be being 'locked' due to pinning to a twin boundary path along the c axis. However, the vortices were observed to meander along the applied field direction once above a critical angle θ_B. This can be interpreted by anisotropic London theory which includes the effects of an anisotropic environment on the coordination of the vortex lattice. The value of the anistropy from [83] was $\gamma_{ab} \approx 1.3$ which was similar to the value found in previous studies [116].

3.4.2 High Field SANS Studies

Brown *et al.* [12] did the first "high-field" study of the vortex lattice in twinned $YBa_2Cu_3O_7$. At low fields, it was shown that the vortex lattice is made up of four distorted triangular vortex lattices which each belong to different domains within the sample. This is in

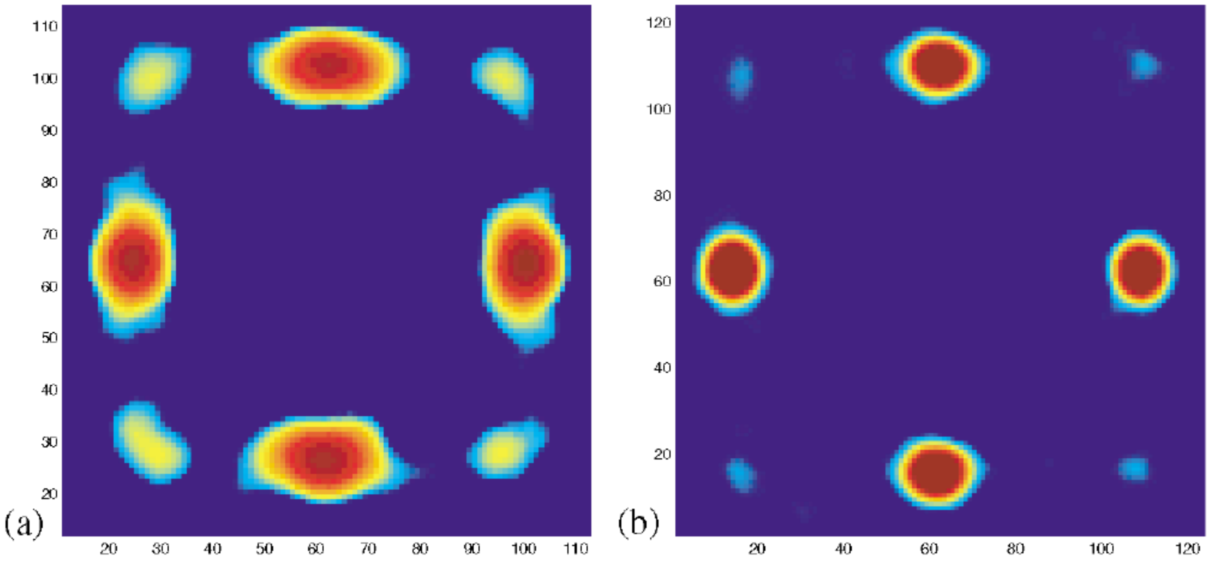

Figure 3.5: Vortex lattice diffraction patterns showing the change in position of the weaker spots at the applied field is increased. (a) at $B = 7$ T and (b) at $B = 11$ T. Figure reproduced from [12].

agreement with the observation by Keimer *et al.* [52]. The distortion is believed to come from the a-b anisotropy present in each domain of the orthorhombic crystal. This was confirmed by the aforementioned study by Johnson *et al.* [50] on an untwinned crystal. The diffraction pattern shown in figure 3.5(a) shows a distortion of the four triangular vortex lattices whereby some of the weaker diffraction spots are closer to the stronger diffraction spots, and the others have moved towards the corners. At 11 T, as shown in figure 3.5(b), the vortex lattice has undergone a structural transition to square whereby the strong diffraction spots are the only first order spots while the weaker spots in corners are now playing the role of second order spots of a square vortex lattice. The orientation of the square vortex lattice was as expected from d-wave theories [44, 82].

White *et al.* [104] mapped out the high-field phase diagram of the vortex lattice in a lightly twinned sample of $YBa_2Cu_3O_7$. They observed, at high field, a transition from the square coordination back to the triangular coordination by increasing the angle between the c-axis and the field direction or by increasing the sample temperature. The authors confirmed that the fourfold symmetry observed in the low field vortex lattice diffraction patterns arose from four distinct domains rather than square vortex lattices. It was also

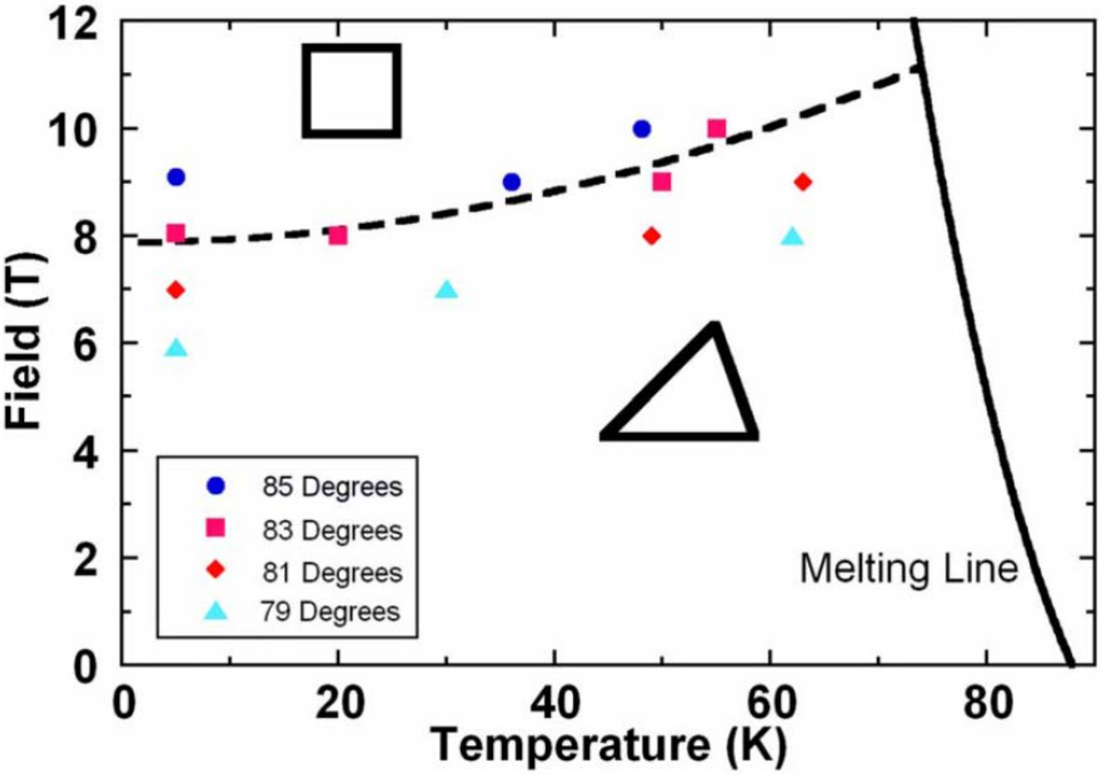

Figure 3.6: A schematic to show the vortex lattice structure as a function of magnetic field and temperature. The dashed line represents the angle halfway between the square and triangular phases as the transition is second order. Figure reproduced from [104].

found that the "aligning-effect" of one set of twin planes can be removed by changing the field direction such that it is approximately 5° from the crystal c-axis. By increasing the temperature, it is found that the hexagonal to square transition occurs at a higher field, as shown in figure 3.6. This is consistent with d-wave effects being responsible for the vortex lattice transition as the anisotropy in the d-wave gap becomes less important compared with the $k_B T$ as the temperature approaches T_c.

White *et al.*, in the same study, also investigated the effect of rotating the applied field towards the [1 0 0] direction making the vortices no longer parallel to either set of twin planes. This means both sets of two crystal domains are in different relative orientations with respect to the applied field as one is rotated about the a-axis and the other is rotated about the b-axis. They observed a a reduction in γ_{ab} at approximately 5 T. The vortex lattice undergoes a transition to a square coordination at higher fields. This is different to

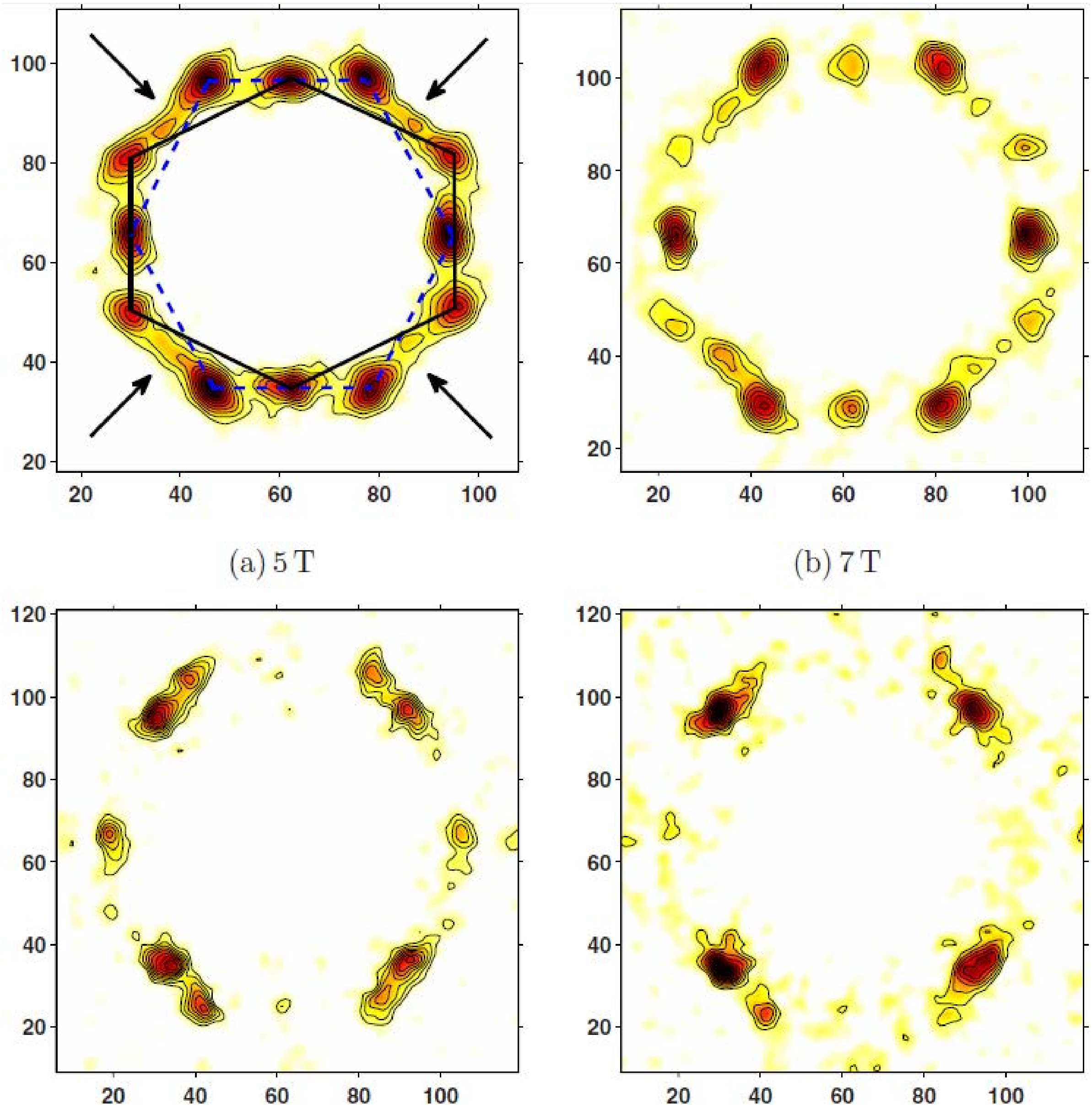

(a) 5 T

(b) 7 T

(c) 8.5 T

(d) 9 T

Figure 3.7: Magnetic field dependence of the vortex lattice structure with the field applied at an angle of 10° to the crystal *c*-axis. Two domains of the vortex lattice are distinguishable as seen from the dashed blue and solid black lines in (a). At higher fields, the vortex lattice structure becomes square. The field at which transition occurs is lower than if the field is parallel with the *c*-axis. Figure reproduced from [104].

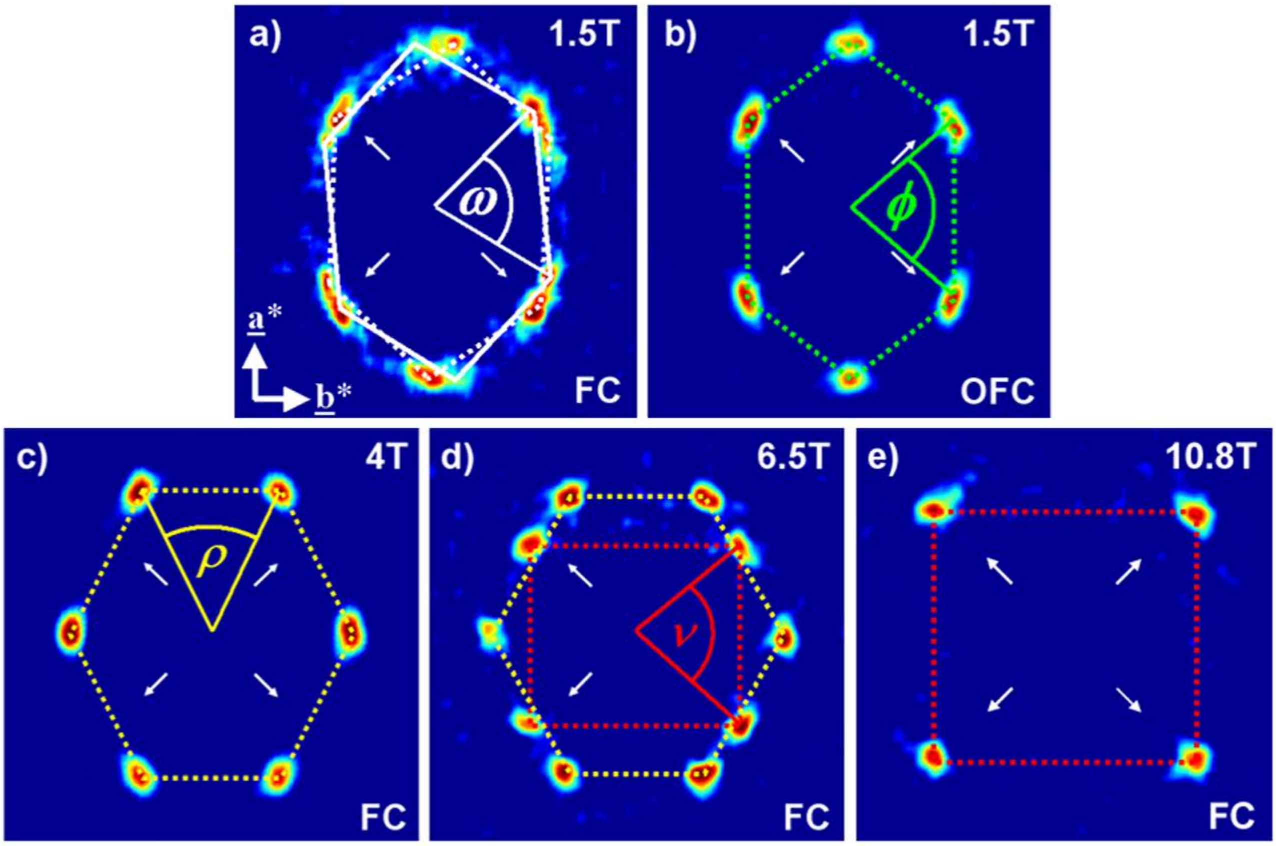

Figure 3.8: The evolution of the vortex lattice structure of detwinned YBCO with applied field at 2 K. Figure reproduced from [107].

transition with the field parallel to the *c*-axis as the transition occurs at a lower applied field and is first order - the evidence for it being a first order transition is the coexistence of both hexagonal and square vortex lattices as shown in figure 3.7.

White *et al*. [107] undertook the first truly high-field study (up to 10.8 T) on the vortex lattice structure transitions in detwinned YBCO. As the pinning to the twin boundaries does not occur in the detwinned crystals, a new distorted hexagonal vortex lattice structure was observed at intermediate fields. Figure 3.8(a) shows that at 1.5 T the vortex lattice structure can be markedly different whether it is prepared by simply field cooling (FC) or oscillating field cooling (OFC). By simply using the field cooling method, the vortex lattice structure is clearly made up of two distorted hexagonal domains similar to that observed in a twinned crystal. However when using the oscillating field cooling method, the vortex lattice structure is made up of a single distorted hexagonal domain. At higher fields the stronger inter-vortex interactions render the OFC vortex lattice preparation method as unnecessary. Figure 3.8(c) shows that the vortex lattice structure undergoes a first-order 90° reorientation. The authors attribute this structural transition to Fermi-surface effects. The vortex lattice undergoes another structural transition by increasing the field further. At 6.5 T, as shown in figure 3.8(d), the distorted hexagonal domain coexists with a rhombic domain. The distortions of each domain is in opposite directions which provides evidence for a d + s-wave admixture for the order parameter. The rapid crossover from one domain to the other indicates that the structural transition is first order. The vortex lattice is made up of only the rhombic domain by 7.5 T, and it becomes more square-like as the field is increased up to 10.8 T as shown in figure 3.8(e).

A further study by White *et al.* [106] studied the vortex lattice structure and form factor in detwinned YBCO at higher temperatures (up to T_C) up to high magnetic fields (10.8 T). Here the authors argue that the field-induced structural transitions can be described, for the most part, by the increasing importance of nonlocal effects on the vortex-vortex interactions as the field is increased.

I was involved in the first high field vortex lattice study on a detwinned crystal, that extended the previously investigated maximum field from 10.8 T to 16.7 T, with the field applied parallel to the c-axis. This work has been published as Cameron *et al.* [15]. We observed the continuation of the smooth variation in vortex lattice structure at high magnetic fields with the lattice passing through a square structure at 12 T and varying continually up to 16.7 T. The CuO chains provide an s-wave addition to the already d + s-wave order parameter. The contributions to the order parameter from the chain layers must have an opposite sign to the s-wave component of the CuO_2 layers in order to make sense of square vortex lattice structure at 12 T, and that at higher fields than those reached in the experiment could confirm that the lattice enters a field independent structure once the chain superconductivity is entirely suppressed. We also studied the vortex lattice melting. Figure 3.9 shows the variation of the vortex lattice form factor with temperature across the vortex lattice melting transition. It can be seen in figure 3.9(a)

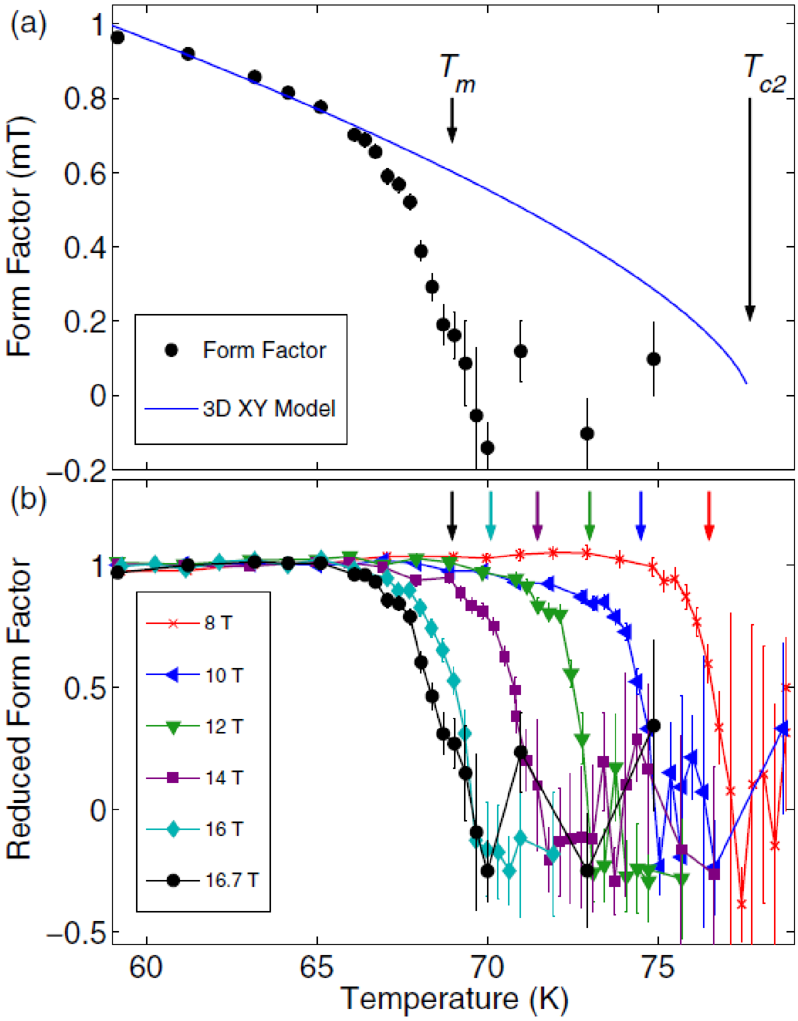

Figure 3.9: The variation of the form factor as a function of temperature across the vortex lattice melting transition. (a) The form factor for $B = 16.7$ T, alongside the predicted variation from the theoretical model. (b) The form factor for fields from 8 to 16.7 T. Figure reproduced from [15].

that the vortex lattice form factor falls off well below the model prediction. The falloff begins as a true Debye-Waller effect which arises from the increasing thermally induced deviations of the vortex lattice from equilibrium followed by vortex lattice melting when the displacements are a significant enough fraction of the "Lindemann criterion", c_L, of the vortex line spacing.

3.4.3 Ca-doped YBCO

By doping calcium on the yttrium sites, the hole concentration in the copper oxide planes can be increased beyond the values found in fully oxygenated YBCO, but without perturbing the chain ordering. This makes it easier to isolate the effect of the chains on the superconductivity when comparing with pure YBCO. I carried out a series of experiments on $Y_{0.96}Ca_{0.04}Ba_2Cu_3O_7$ (Ca-YBCO) [14]; in this thesis I report on the key results of relevance to discussion of the high field results in $YBa_2Cu_3O_7$. Since Ca-doped crystals are more difficult to detwin fully, we did not attempt this process, but reduced the effect on the SANS results of pinning by twin planes by small changes in field direction. The twin planes are along $\{1\ 1\ 0\}$ diections, so with B parallel to c, the vortex lines are parallel to the twin planes and very strongly pinned. However, by rotating about $\{1\ 0\ 0\}$ the field is tilted away from all thetwin planes, and for a tilt of a few degrees, the vortex lines pull out of the twin planes and the their pinning is much weaker [10].

We were able to find differences between the the Ca-doped YBCO and the fully oxygenated YBCO in the vortex lattice structure and coordination at 2 K as a function of magnetic field (up to 16.4 T) which indicates changes in the superconducting order parameter. We also found that the inclusion of calcium into YBCO increases the vortex pinning strength as it is more disordered at low fields than YBCO. The vortex lattice opening angle, as shown in figure 3.10, increases smoothly with field until around 13 T whereupon the vortex lattice structure remains constant up to the maximum applied field of 16.4 T with an opening angle of approximately 100°. This is significant as it agrees with the expected opening angle from Kirtley *et al.* [54], and we would expect the vortex lattice structure in $YBa_2Cu_3O_7$ to behave similarly to the Ca-doped sample as the low field behaviour is similar (albeit at approximately half the field in Ca-doped YBCO when compared to $YBa_2Cu_3O_7$). Therefore, in $YBa_2Cu_3O_7$, we would expect to reach the high-field limit of the structural evolution at approximately 26 T.

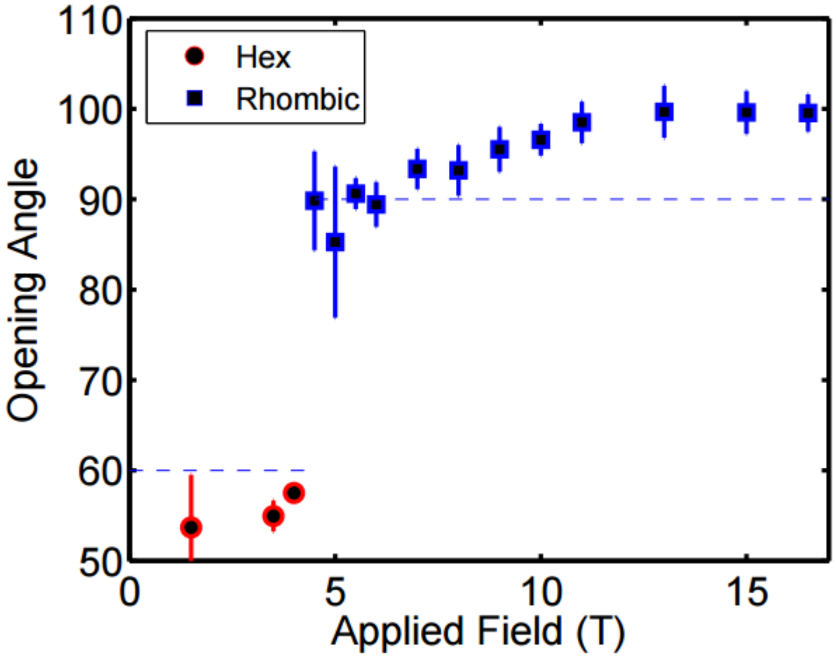

Figure 3.10: Opening angle of the vortex lattice diffraction pattern in Ca-doped YBCO.

3.5 The Vortex Lattice in $YBa_2Cu_3O_7$ up to 25 T

The results in this section are formed by a series of measurements taken at the Helmholtz-Zentrum, Berlin in January 2016. I carried out this experiment with assistance from Alistair Cameron, Alexander Holmes, Ted Forgan (along with the instrument support staff which included Oleksandr Prokhnenko and Maciej Bartkowiak). The results presented here also form a publication submitted to Physical Review Letters [77].

The conclusion of our overview of work on the vortex lattice of YBCO is that in high-quality de-twinned single crystals, the field-induced vortex lattice structural transitions are *first-order*, unlike the *second-order* structural transitions observed in the twinned samples [12, 104]. Here we extend the field range up to 25 T and obtain new information on the intrinsic vortex lattice structure and superconducting state at high fields.

3.6 Experimental Details

3.6.1 Sample Preparation

The sample consisted of a mosaic of eleven co-aligned single crystals of detwinned $YBa_2Cu_3O_7$ with a total mass of 72.7 mg. The crystals were grown by Andreas Erb from a molten flux of $BaCO_3$, CuO and Y_2O_3 in $BaZrO_3$ crucibles [29]. They were detwinned through the application of uniaxial stress at 500° C for 24 hours [65, 40]. The crystals were then oxygenated close to the O_7 composition under an O_2 atmosphere of 100 bar at 300° C for 150 hours [28]. The filled CuO chains made the crystals slightly over-doped, but greatly reduced pinning by oxygen vacancies relative to that for an optimally-doped sample. A crystal from the mosaic gave a T_c of 89.0 with a 90% transition width of 2 K. Given the high purity of the samples, the spread in T_c suggests a slight spread in oxygen content across the mosaic.

The mosaic was mounted on a 1 mm thick pure high purity aluminium plate with the crystal c axis perpendicular to the plate and the a direction co-aligned between crystals, as shown in figure 3.11. The higher the purity of the aluminium, the lower the contribution to the total scattering it has.

3.6.2 Experimental set-up

Our neutron measurements were the first vortex lattice study carried out at the High Magnetic Field Facility for Neutron Scattering which consists of the High Field Magnet (HFM) [96] and the EXtreme Environment Diffractometer (EXED) [75] at the Helmholtz-Zentrum Berlin (HZB). The HFM, described in chapter 2, is a hybrid solenoid magnet system with a maximum field of 25 T which makes it the highest continuous magnetic field available in the world for neutron scattering experiments (the magnet now has an increased maximum magnetic field of 26 T due to recent technical advances). The direction of the horizontal magnetic field, and therefore of the sample, can be rotated relative to the

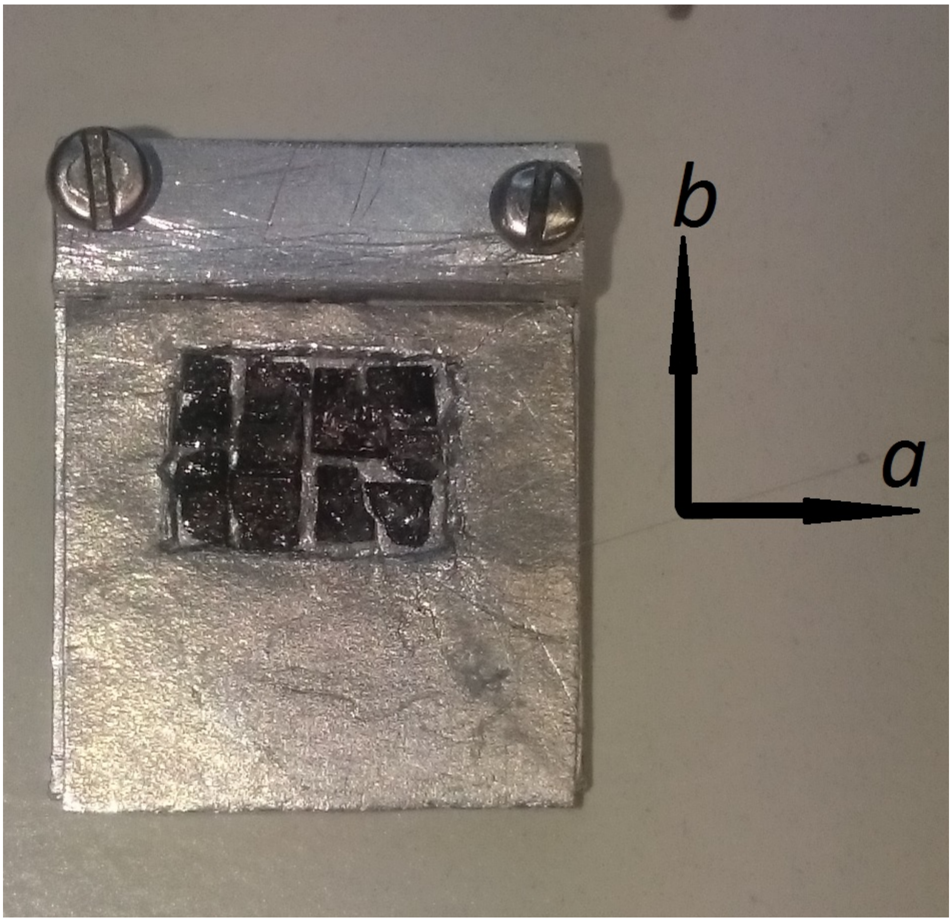

Figure 3.11: $YBa_2Cu_3O_7$ mosaic mounted onto an aluminium plate. A similarly co-aligned mosaic is on the opposite side of the plate.

incoming beam by up to 15°, limited by the size of the conical solenoid openings. The multi-purpose EXED instrument operates in time-of-flight (TOF) mode, with a wide range of incident neutron wavelengths, maximising the volume of reciprocal space that can be observed for a given orientation of the HFM.

The neutron beam from the HZB reactor was chopped into pulses with a full-width-half-maximum length of 2.5 μs, at a frequency of 10 Hz by two counter-rotating choppers at a distance of 53 m before the sample. The setup allowed neutrons over the wavelength range 2.5 - 9.3 Å to be identified by their time of arrival at the detector. The wavelength resolution arising from the width of the incoming neutron pulse varied from 7 to 2 % over the wavelength range. The incoming beam was collimated by a 30 mm diameter aperture at 6.5 m before the sample and a second 12 mm diameter aperture 1.0 m before the sample. The beam is collimated twice on the incoming side of the sample by 30 mm and 12 mm diameter apertures at a distance of 6.5 m and 1.0 m, respectively, from the sample. The sample area was defined by a 7×5 mm^2 hole in a cadmium "window frame" around the mosaic. The sample-to-detector distance was 5.5 m.

By measuring in TOF mode we can make use of the white neutron beam produced by the reactor. Given that all neutrons are admitted at the same time, t_0, the higher energy neutrons arrive at the detector sooner than the lower energy neutrons. The neutron's time of arrival at the detector therefore informs us of its wavelength. A typical SANS study of the VL (non-TOF mode) uses a monochromatic beam of neutrons of a particular mean wavelength 6 - 10 Å, with a typical FWHM wavelength spread of 10-20 %. The wavelength spread arising from the pulse width is not negligible in TOF mode.

3.6.3 Vortex Lattice Preparation

The vortex lattice was prepared for observation at the base temperature of 3 K by cooling the sample through T_C in an applied magnetic field. The vortex lattice quality is usually improved by oscillating the field value while cooling as explained in chapter 2. In the present case, the small variations $\sim$ 30 mT from the magnet power supply served this purpose. It is also worth noting that this oscillation of 30 mT continued throughout all measurements. For a given value of applied field, and given rotation of the HFM away from the incident beam direction, only one particular wavelength of neutron would be incident at the Bragg angle for diffraction by the vortex lattice. Neutrons of different wavelengths in the range supplied in TOF mode would be incident at angles away from the Bragg condition. Hence the data at a single sample angle can contain a substantial part of the "rocking curve" of intensity of the VL Bragg spot. In experiments with a monochromatic neutron beam, the integrated intensity under the "rocking curve" is obtained by taking measurements at many different sample angles, rocking through the Bragg condition. In the present case TOF measurements were taken at just a few sample angles to check for consistency and to ensure that the entire rocking curve was covered by the wavelength spread [73]. The vortex lattice diffraction pattern shown in figure 3.14 was obtained by measuring at 3 K for magnet rotation angles to the left and right, in order to obtain both LHS & RHS spots to give a complete 1st-order pattern from the VL. Background measurements were taken at the same angles above T_C and were subtracted from the measurements below T_C so that only the vortex lattice signal remained.

3.6.4 Vortex Lattice Form Factor

The vortex lattice form factor is the magnitude of a Fourier component of the spatial variation of the magnetic field within the vortices. The field dependence of this quantity is shown in figure 3.13, along with two simple theory lines, which are explained in the discussion section.

As described in chapter 2 the form factor, $F(\mathbf{q})$ for a diffraction spot with wavevector $\mathbf{q}$, is related to the integrated intensity, $I(\mathbf{q})$, by the following relationship [19]:

$$|F(\mathbf{q})|^2 = \frac{I(\mathbf{q}) q \Phi_0^2}{2\pi V \left(\frac{\gamma}{4}\right)^2}, \tag{3.1}$$

where Φ_0 ($= h/2e$) is the magnetic flux quantum, V is the illuminated sample volume, γ

(= 1.91) is the neutron magnetic moment in nuclear magnetons, and:

$$I(\mathbf{q}) = \Sigma \left[\frac{I(q_x, q_y, q_z, \lambda_n)}{\phi \lambda_n^2} \right], \tag{3.2}$$

where $I(q_x, q_y, q_z, \lambda_n)$ is the number of neutron counts centered in a small range about wavelength λ_n, which arrive in a pixel of **q**-space centered on (q_x, q_y, q_z). ϕ is the incident neutron flux density in that neutron wavelength range. The sum is performed over the region of **q**-space containing a single diffraction spot and over the entire spectrum of neutron wavelengths used, after background subtraction. The vortex lattice rocking-curve width was obtained by fitting a Gaussian line shape to the intensity summed over q_x, q_y as a function of q_z. The variation of the q_z with field is shown in figure 3.12. The larger errors in our recent measurements compared with previous measurements is attributed to the overall lower intensity at HZB compared with ILL, resulting is lower statistics. There is also a very large variation of size in the error bars of the data from EXED; this is especially apparent when comparing the error at 23 T to the error at 25 T. We attribute this to the relatively short counting time at 23 T compared to at 25 T. The background measurements at 23 T also had shorter counting times than would have been ideal. This was for technical reasons that did not allow us to change the magnetic field from 25 T to another field for over 24 hours. Whilst this meant that the statistics were significantly enhanced for the measurement of q_z at 25 T, we were unable to match these statistics at the other fields (especially 23 T as there was a technical issue with the resistive coils of the hybrid cryomagnet that did not allow us to measure above 21 T towards the end of the experiment). The q_z width is larger than the instrumental resolution.

Discussion

The field-dependence of the form factor is shown in figure 3.13. The vortex lattice form factors of the previous measurements have been scaled down by 20% in order to make the data match with our current data. A small discrepancy is not particularly surprising

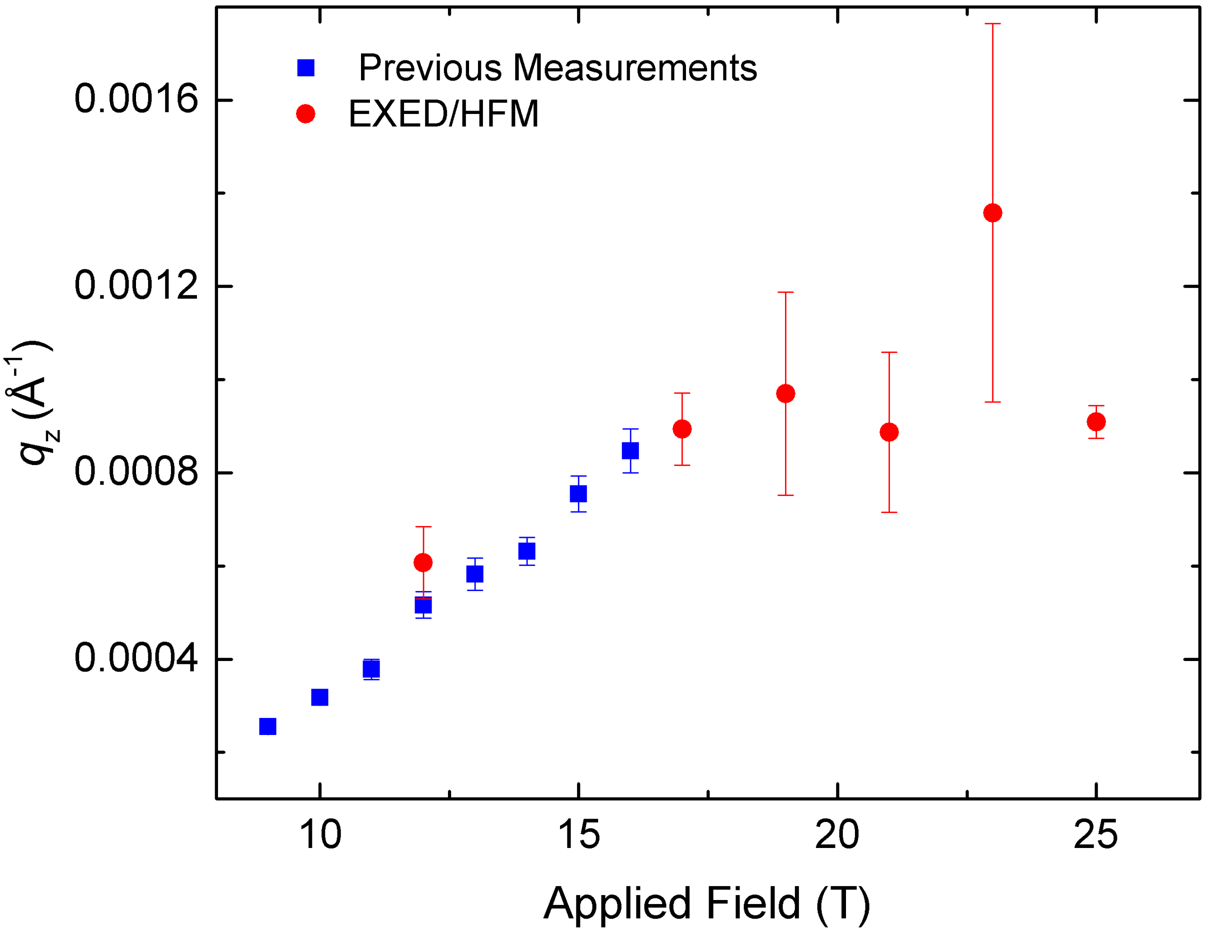

Figure 3.12: The evolution of the vortex lattice perfection with magnetic field at 3 K. The red circular points are from the measurements taken at EXED, and the blue points are from the measurements done at ILL.

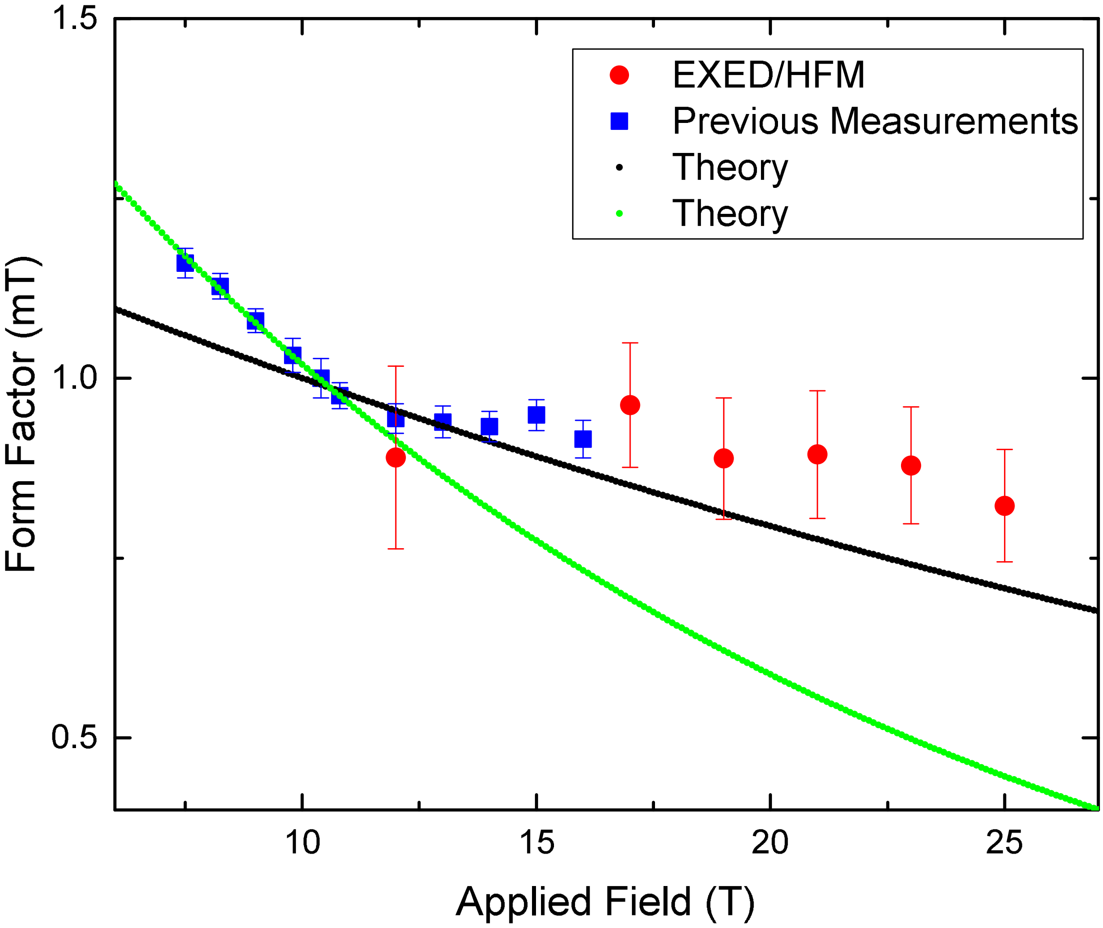

Figure 3.13: Vortex lattice form factor as a function of magnetic field. For comparison we have included previous measurements [15, 106]. The form factors of the previous measurements have been scaled down by 20% so that the data match up. This may reflect calibration differences between the monochromatic and TOF measurements. The continuous black ($\xi = 14.8$ Å) and green lines ($\xi = 26$ Å) represent the predictions of the modified London model (see text) for two different choices of coherence length, ξ.

when doing experiments at two different instruments at different sources for numerous reasons such as the different calibration standards across the two instruments. Also, the sample used for the present study is not exactly the same mosaic as previously used in previous measurements. The alignment between individual crystals making up the mosaic sample may also be slightly different between the two experiments. We attribute the 20% difference between the old and new data to small errors from a number of sources, such as those described above.

For fields much less than B_{C2} ($= \mu_B H_{C2}$), it is expected that the form factor will obey an extended London model, where at low temperatures the effect of the vortex cores of size $\sim \xi$, the coherence length, is represented by an exponential factor [106]:

$$F(\mathbf{q}) = F_{\mathrm{London}}(\mathbf{q}) \times \exp(-cq^2\xi^2). \tag{3.3}$$

Here, c is a constant ~ 0.44 [106], and we have ignored any a-b anisotropy in ξ because throughout our field range, $\mathbf{q}$ remains approximately equidistant in angle from both axes. However, we have to take account of the anisotropy of the London penetration depth, because - by assumption - the degree of superconducting pairing, and hence one of the penetration depths in the basal plane, is field-dependent. We therefore introduce values λ_a & λ_b, arising from supercurrents along the a & b directions, so that the London equation for the form factor becomes anisotropic.

$$F\left(q\right) = \frac{\langle B\rangle}{1+q^2\lambda^2} \rightarrow \frac{\langle B\rangle}{1+q_x^2\lambda_b^2+q_y^2\lambda_a^2}. \tag{3.4}$$

We have proposed that the value λ_b for the chain-direction currents is field-dependent, as the chains become depaired. This happens over a field range around 10 T, so we take for this variation a phenomenological expression that has the expected qualitative behaviour at large and small fields:

$$\lambda_b^2(B) = \lambda_a^2(1 + 0.4\tanh((B-10)/7)) \tag{3.5}$$

Here, B is in Tesla, and we take the approximate width of the field range where λ_b is varying as 7 T. The factor 0.4 means that the two penetration depths differ by $\pm \sim 20\%$ at low and high fields, with λ_b shorter than λ_a at low field and longer at high field.

To calculate the form factor as a function of field, we need the values of q_x, q_y & q, which may be obtained from the positions of the diffraction spots. Alternatively, using only the value of B, the experimentally-determined value of ν, and the fact that each vortex contains one flux quantum, one may write:

$$q^2 = 4\pi^2 B/\Phi_0 \sin(\nu)\ ;\ (q_x, q_y) = q(\sin(\nu/2), \cos(\nu/2)) \tag{3.6}$$

The exponential in equation 3.3 for the form factor relies on the value of ξ, which may be related to the upper critical field using the Ginzburg-Landau relationship: $B_{\mathrm{C2}} = \Phi_0/2\pi\xi^2$. Hence, the experimental value of B_{C2} may be used to give the expected value for ξ or alternatively the core effect may be shown to fall off approximately exponentially with field:

$$\exp(-cq^2\xi^2) = \exp(-2\pi c B/B_{\mathrm{C2}} \sin(\nu)). \tag{3.7}$$

It is clear from figure 3.15 that the vortex lattice remains more robust at high fields than would be expected from the suppression of spatial Fourier components of the field due to overlap of the vortex cores, even using a very small value of 14.8 Å for ξ. The field dependence below 11 T implies a larger value of ξ, and at still lower fields [106] the data may be fitted by an effective $\xi > 30$ Å . Such a large value probably reflects a 'static Debye-Waller factor' which arises from vortex lattice distortions due to pinning [106], which mimics a broader vortex core. We find that the widths of the diffraction spots in all three directions of $\mathbf{q}$ are almost field-independent, with the FWHM in q_z $\sim 6 \times 10^{-4}$ Å^{-1} which is at least twice the instrument resolution. This indicates that vortex lattice imperfections, probably due to pinning, are not completely negligible at high field, although they do not appear to be changing with field in this region. The q_z width corresponds to a correlation length along the vortex lines of $\sim 4 \times 10^{-7}$ m.

In any case, even if pinning effects were completely negligible, the form factor is not falling off with field as expected for a constant value of λ_L and a reasonable constant value (based on our previous SANS results on YBCO) of ξ. If we assume that the field is leading to weakening of superconductivity along the CuO chain direction (b-direction), we can use a reasonable value of ξ to fit the data up to ~ 13 T but not to higher fields. The intensity of the vortex lattice signal reflects the field contrast between the cores and their surroundings. We therefore conclude that, at high fields (although low relative to $B_{\mathrm{C}2}$), there is a contribution to the spatial variation of magnetic field in the VL in addition to that arising from super-currents circulating around the vortices. This extra contribution *must* correspond to an additional magnetisation of the vortex cores. This can arise as follows: in the cores, the carriers are de-paired and much less strongly bound in the anti-parallel spin arrangement of Cooper pairs, so the spins are freer to align parallel to the magnetic field. This allows the formation of a Pauli paramagnetic moment in the core region [45]. Such effects must be present in all singlet-pairing superconductors, but will be negligible unless $\mu_{\mathrm{B}} B_{\mathrm{C}2} \geq k_{\mathrm{B}} T_{\mathrm{C}}$, so that the Zeeman energy of the electron spins is comparable with the zero-field energy gap. Pauli paramagnetic effects have been observed by SANS in a heavy-fermion material $\mathrm{CeCoIn_5}$ [9, 105], a borocarbide [21] and an iron-based superconductor [61], but not to our knowledge in YBCO. Nevertheless, Pauli-paramagnetic effects are expected in our sample, because it satisfies $\mu_{\mathrm{B}} B_{\mathrm{C}2} \simeq k_{\mathrm{B}} T_{\mathrm{C}}$.

The Pauli-paramagnetic behaviour observed in the heavy fermion superconductor $\mathrm{CeCoIn_5}$ [9, 109] is quite different to what we have observed in $\mathrm{YBa_2Cu_3O_7}$. In $\mathrm{CeCoIn_5}$, the form factor actually increases with applied field. A similar effect is seen in $\mathrm{CeCu_2Si_2}$ as will be shown in the next chapter. It is clear that the paramagnetic effects are not the same in YBCO as they are in these two heavy fermion compounds. Therefore, it may be more useful to compare the Pauli-paramagnetic behaviour observed by us in YBCO with that of $\mathrm{TmNi_2B_2C}$ observed by DeBeer-Schmitt *et al*. [21]. As shown in figure 3.17, the form factor (plotted on a logarithmic y-scale) clearly lies above the theoretical lines (obtained by the Clem model for two different penetration depths), however it does not increase with field in the same way as $CeCoIn_5$ does. The low field behaviour of $TmNi_2B_2C$ is similar to our observations in YBCO. The vortex lattice form factor in $TmNi_2B_2C$ remains constant up to approximately $0.6H_{C2}$. Although the dashed red line fits well to the end points, it does not succeed in fitting to all of the intermediate points. These intermediate points are clearly not exponentially dependent on the applied field. The authors attribute the nonexponential behaviour of the form factor to paramagnetic effects. They explain this by a microscopic calculation which takes into account paramagnetism as shown in the theoretical models by Ichioka & Machida, [45, 46], as described in chapter 1 and also as described in the publication by DeBeer-Schmitt *et al.* [21]. From the calculations the authors conclude that the paramagnetic parameter μ is approximately 1.71 in $TmNi_2B_2C$ at 1.6 K. This indicates weak paramagnetic effects. Based on our evidence that the form factor is still slowly decreasing with field in YBCO (although not exponentially), we would expect it to have an even weaker paramagnetic effect than that of $TmNi_2B_2C$ ($\mu \approx 1$). A field-induced increase of the vortex lattice form factor would be indicative of a strong paramagnetic effect ($\mu > 2$), and it is clear that this is not the case in either YBCO or $TmNi_2B_2C$.

3.6.5 Vortex Lattice Structure

The vortex lattice structure can be described by the angle between two diffraction spots, ν, which is bisected by the b^* direction. Figure 3.14 shows a typical diffraction pattern at 23 T and 3 K. The incident beam has been masked out, and the data were "smoothed" using a hat function in the software package Mantid.

Figure 3.15 shows the opening angle, ν, as a function of magnetic field. The red circular points represent measurements from this study, and for comparison we have included data for the opening angle between 9 - 16 T from previous measurements [15]. We see here that the structure continuously evolves through a square vortex lattice at approximately 12.5 T and increases up to approximately 100° at the maximum applied field of 25 T, which is expected based on previous results on Ca-doped YBCO. All of these measurements were

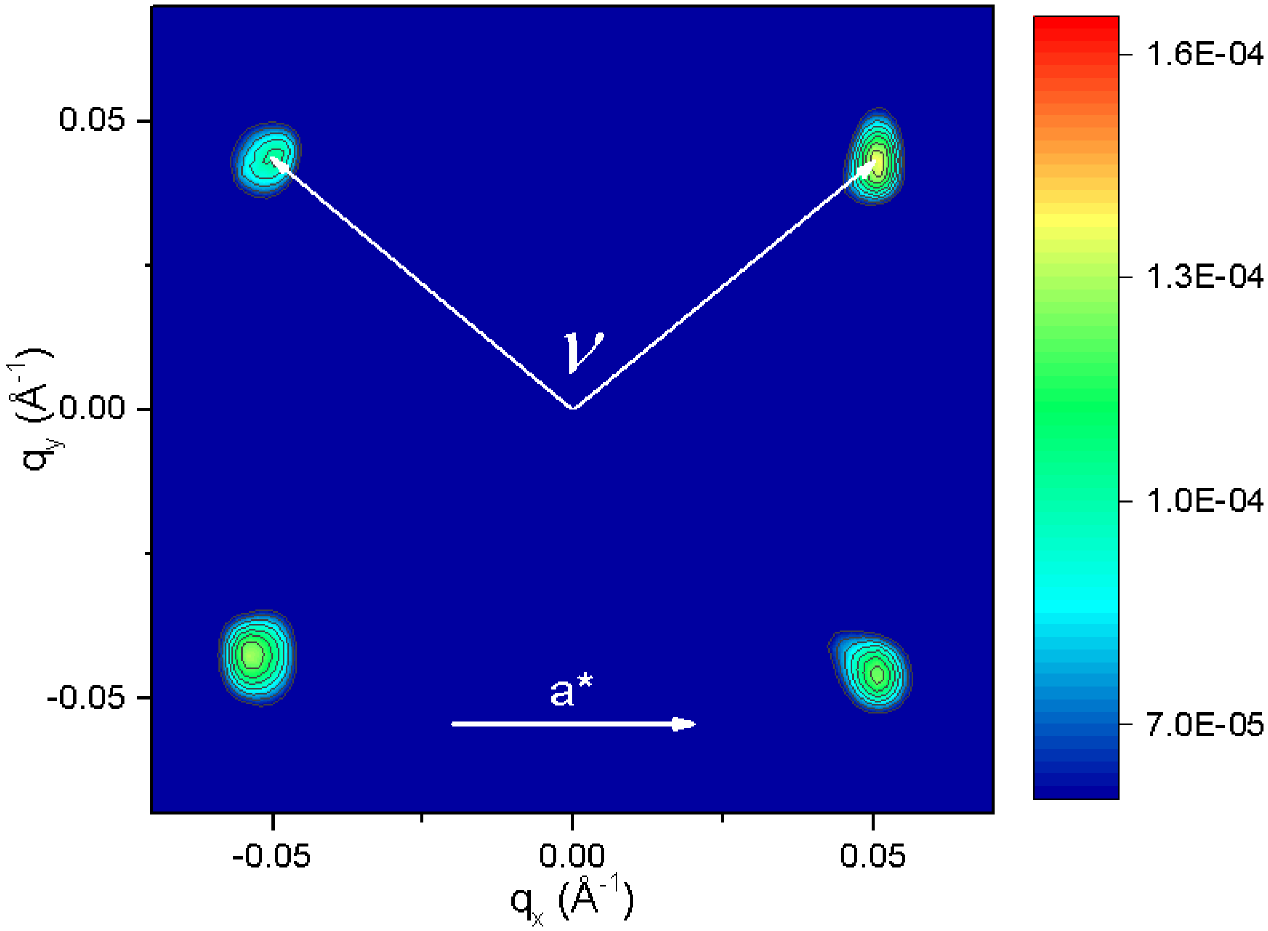

Figure 3.14: A vortex lattice diffraction pattern at 23 T and 3 K. The opening angle, ν, is used to describe the structure of the vortex lattice. The plotted signal is a measure of the counts per pixel summed along q_z divided by the product of the incident beam intensity and the square of the neutron wavelength.

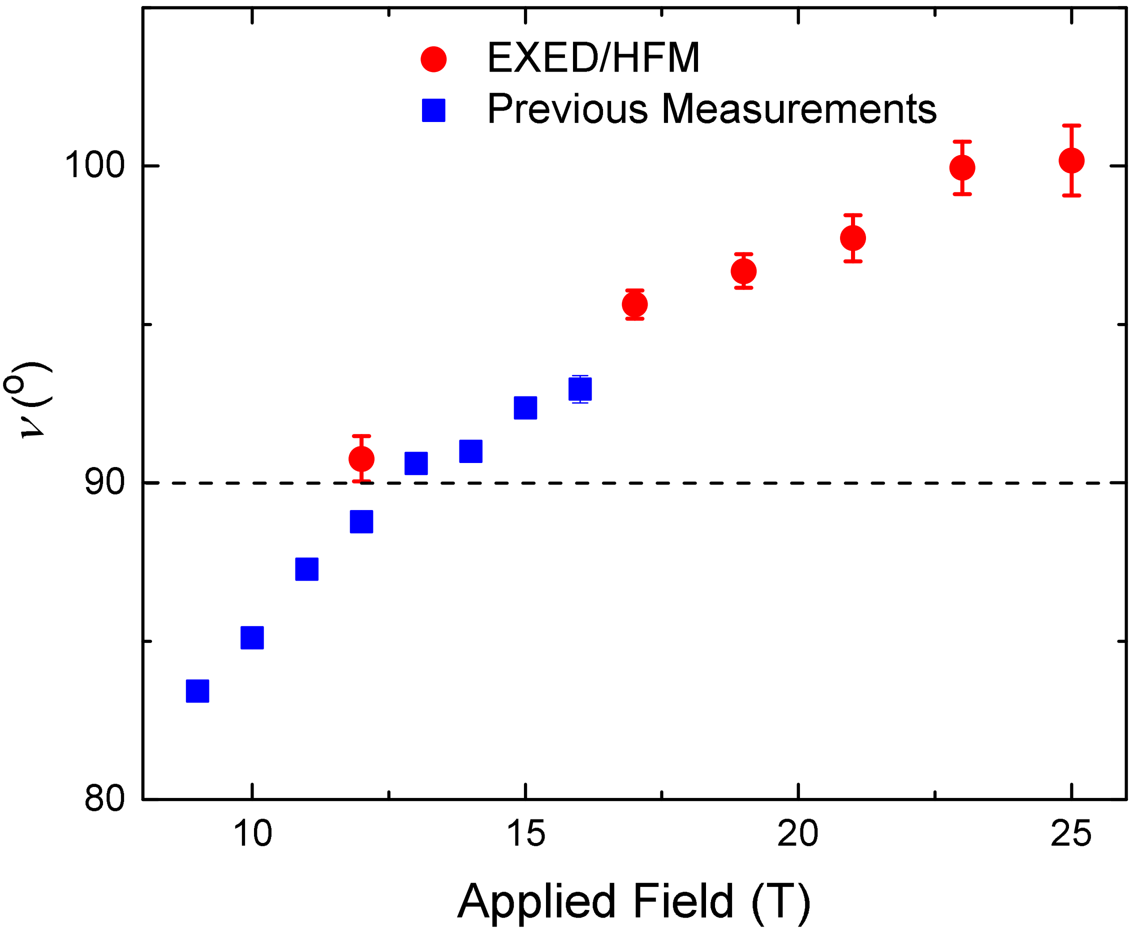

Figure 3.15: The evolution of the vortex lattice structure with magnetic field at 3 K. The red circular points are from this study while the blue square points are from a previous study [15] up to 16.7 T.

done at 3 K.

Discussion

To understand the evolution with field of the vortex lattice structure at base temperature, we must consider the whole field range that has been explored in this compound. Firstly, at the lowest fields below ~ 2 T, the vortex lattice structure resembles a distorted hexagonal [106, 12, 108]. The distortion of $\sim 30\%$ is independent of field and its sign indicates

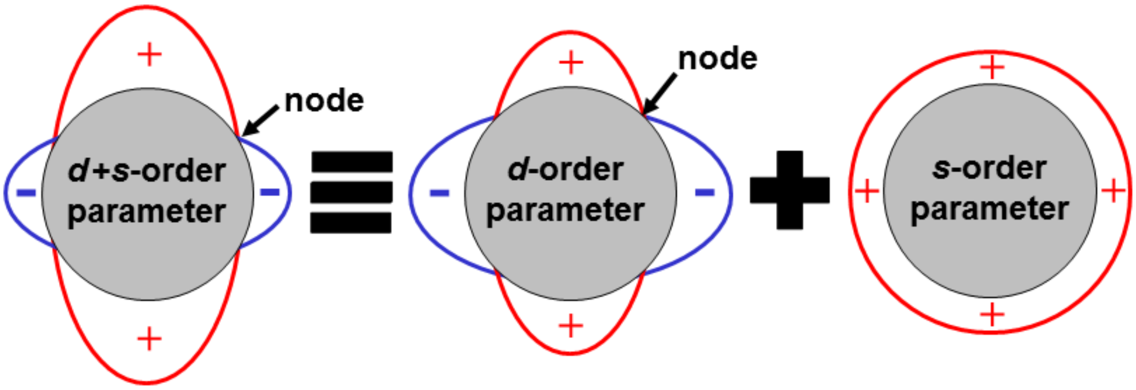

Figure 3.16: Schematic representation of the variation of a $d + s$ superconducting order parameter around a cylindrical Fermi surface. In YBCO, such an admixture must arise because of the crystal structure and it has the same orthorhombic symmetry. It is seen that the nodal positions lie nearer the direction of weaker superconductivity.

an enhanced superfluid density along the b-direction, which no doubt arises from superconductivity of the carriers in the CuO chains, which run along this direction. This may be described by anisotropic London theory [57], which applies when values of the London penetration depth λ_L and the vortex spacing are both much larger than the vortex core diameter $\sim \xi$, the coherence length.

Despite the a-b anisotropy revealed by the vortex lattice distortion, the form factor is the same for all diffracted spots. However, this is expected in London theory, because the form factor is a function of $q\lambda_L$, where q is the wavevector of a VL diffraction spot. When a-b anisotropy of λ_L leads to a vortex lattice distortion, the anisotropy of q and λ_L exactly cancel in this theory.

The stronger superconductivity along b is confirmed by zero-field measurements of the angles of the nodes in the order parameter, by Kirtley *et al.*,[54]. In a purely d-wave superconductor, these would lie at exactly 45° to both a and b axes, whereas they are found to be closer to a. As represented schematically in figure 3.16, this indicates enhanced superconductivity along b.

Between $\sim$ 2 & 6.5 T, the vortex lattice is also distorted hexagonal, but with the hexagon rotated by 90° relative to the very low-field case [106, 12, 108]. The distortion decreases with increasing field.

It should be noted that for the field parallel to a principal axis (c-axis in this case) anisotropic London theory gives the free energy of the vortex lattice as independent of the orientation of vortex lattice relative to the crystal lattice. However, because of this degeneracy *any* additional interaction, however weak, can give a preferred vortex lattice orientation. In this case, it is probable that the vortex lattice orientation is controlled by "nonlocal" interactions [59, 58, 60], which become more important as the vortex lattice spacing comes closer to the vortex core size as the field is increased. However, the existing nonlocal theories [59, 58, 60] are for the case of an isotropic energy gap, which does not apply here and does not predict the 90° reorientation. Nonlocal refers to nonlocal London theory which unlike the local London theory described in chapter 1, where the supercurrent density is proportional to the magnetic vector potential, the supercurrent density and the magnetic vector potential have a nonlocal relationship. It is believed that for strongly type-II superconductors, where the penetration depth is much greater than the coherence length, that nonlocal effects become less important. However, theoretical work [59, 58, 60] predicts that nonlocal corrections to the London equations have an effect on the vortex lattice coordination.

The structure in this field region has been discussed by White *et al.* [106]. For present purposes, we merely emphasise the reduction of anisotropy with field, which strongly suggests that the chain carrier superconductivity is suppressed with field to a much greater extent than that of the CuO_2 planes.

Finally, above ~ 6.5 T, the vortex lattice adopts a high-field structure [106, 12, 108], similar to that observed here. This is a centered-rectangular arrangement: the nearest-neighbour vortex pattern is exactly the same as the pattern of diffraction spots around the main beam - but rotated by 90° about the field axis. (This simple relationship represents the transformation between real and reciprocal lattices for the 2-dimensional vortex lattice.) At approximately 12.5 T, the centered rectangle passes through a square arrangement. At this field, the nearest-neighbour vortex directions are at 45° to the a and

b axes, and change by less than ±5° from this value over the whole field range in which this vortex lattice structure is observed. This result is very suggestive because this is the direction of the nodes in the order parameter if YBCO were a pure d-wave superconductor. The vortex lattice structure in such a material has been calculated as a function of field using first-principles Eilenberger theory [44]. This predicts a first order transition as a function of field from hexagonal to square vortex lattice. This first-principles calculation shows that at high fields the vortex lattice nearest-neighbour direction is along the nodes of the d-wave order parameter.

To clarify how the nearest-neighbour direction relates to the nodal position, a summary of the application of Eilenberger theory in the case of a single vortex line in a $d_{x^2-y^2}$-wave superconductor by Ichioka *et al.* [44] is provided. It was shown that the field distribution around the vortex core is fourfold symmetric and this is an intrinsic feature in a $d_{x^2-y^2}$-wave superconductor. From the calculations, it was revealed that the spatial distribution of the low energy quasiparticle states similarly had a fourfold symmetry. The fourfold symmetry of the low energy quasiparticles is accompanied by extended *tails* that propogate along the nodal directions far from the vortex core. These tails reflect the spatial symmetry of the order parameter. The impact of the tails on the structure was studied [44], and the authors considered the role of the quasiparticles in three categories (i) those from the continuum states associated with the nodal structure in the $d_{x^2-y^2}$-wave pairing, (ii) the core excitations from the bound states localised in a vortex core, and (iii) the quasiparticle transfer between vortices. The role of quasiparticle tunnelling (i.e. transfer between vortices) becomes more significant at higher fields as the vortex cores overlap. When the overlapping occurs, Ichioka *et al.* [44] calculated that the lower energy vortex lattice configurations correspond to a square vortex lattice, with the nearest neighbour directions parallel to the nodal directions [103].

Therefore, if we assume that in YBCO above $\sim$ 6.5 T, the vortex lattice nearest-neighbour directions are closely linked to the nodal directions, then the variation of the vortex lattice structure with field shown in figure 3.15 may be interpreted as an indication of the movement of the nodal directions. Firstly, at fields ~ 7 T, we deduce that the nodes are closer to the *a*-direction than the *b*-direction, which is consistent with superconductivity being stronger along *b* than *a*. This is consistent in sign with the anisotropy in λ_L shown by the vortex lattice at low fields and the direct measurement of nodal positions at zero field by Kirtley *et al.* [54]. However as we have seen, the *b*-direction superconductivity is weakened by field, and this trend is expected to continue in the high-field region. This behavior is confirmed by the progressive movement of the vortex lattice structure towards square at B ~ 12.5 T. From the continuation of this trend at higher fields *past* the square configuration, we deduce that in this region superconductivity is stronger along *a*, giving nodal directions closer to *b*, as indicated in figure 3.16(b). This suggests that the superconductivity in the chain carriers is sufficiently weakened by field that they tend to de-pair the plane carriers also. We recognise that the decomposition of the carriers into chain and plane is a simplification, since they hybridise where the energy bands cross. Also, the electronic structure of the plane carriers is not quite the same along *a* and *b*, so there will be basal plane anisotropies, which may pull the VL nearest-neighbours slightly away from the nodal directions. Nonetheless, the variation of the vortex lattice structure with field shows that the basal plane anisotropy is field-dependent. This is far more likely to be a field effect on the superconductivity, as described, rather than on the underlying electronic band structure. Kirtley *el al.* also finds deviations from the four-fold symmetry, and provides results that are consistent with the gap being larger in the *b*-axis direction than the *a*-axis direction at low fields. The results by Kirtley *et al.* are indicative that a 100° opening angle of the vortex lattice is expected in YBCO [54].

3.7 Conclusions and Outlook

Using neutron scattering at a unique instrument, we have observed diffraction by the lattice of magnetic flux vortices in a superconductor at higher fields than ever before. Our results for $YBa_2Cu_3O_7$ are a clear indication that high magnetic fields tend to destroy

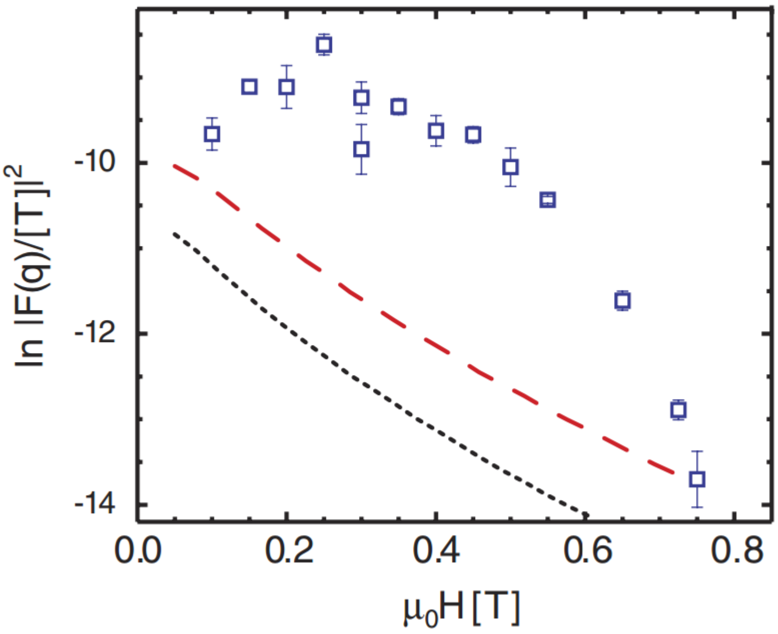

Figure 3.17: The field-dependence of the vortex lattice form factor at 1.6 K in $TmNi_2B_2C$. The lines show the predicted form factor obtained by the Clem model with $\xi = 210$ Å and $\lambda = 780$ Å (dotted black line) or 600 Å (dashed red line). Figure reproduced from [21].

superconducting pairing in the carriers traveling along the crystal b direction (CuO chains) in this material. This leads to a field-dependent change in the superconducting anisotropy, which will be reflected in a change in the angular position of the order-parameter nodes in this orthorhombic $(d+s)$-wave material. In addition, we find that the intensity of the diffraction signal from the vortex lattice hardly falls off at high fields. This is an indication of Pauli-paramagnetic vortex cores, and also bodes well for further studies at the high-field frontier when still greater steady fields become available at neutron scattering facilities.

In the future, it would be of interest to study the temperature-dependence of the vortex lattice form factor and structure up to 25 T. The top graph in figure 3.18 by Cameron *et al.* [15] shows the vortex lattice form factor as a function of temperature at 10 T and 16 T. The lower graph in figure 3.18 shows the perfection of the vortex lattice as a function of temperature at 10 T and 16 T. An irreversibility temperature of $\sim$ 45 K can be estimated based on the temperature dependence of the FWHM, below which the vortex lattice is “frozen in” and the rocking curve width (FWHM) and structure do not change. The 10 and 16 T observations of the structure as a function of temperature

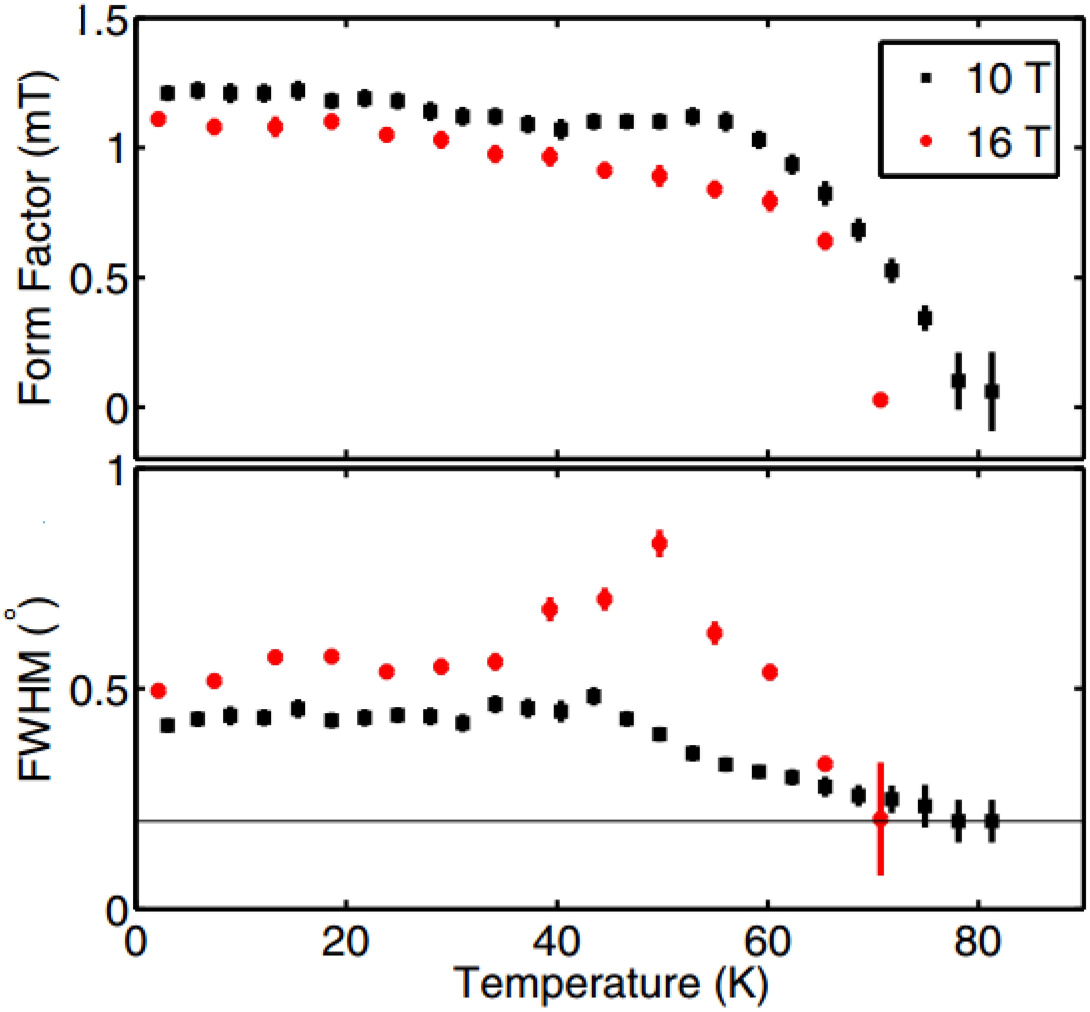

Figure 3.18: The temperature dependence of the vortex lattice form factor and the perfection of the VL structure (rocking curve width) from earlier measurements. Figure reproduced from [15].

suggest that field- and temperature-dependent changes in the nodes may influence the vortex lattice structure and the pinning effects. The temperature dependence of the form factor at low temperatures has been suggested to be due to stronger nonlocal effects in the presence of larger fields [106]. At higher temperatures, the effects of melting the vortex lattice by thermal fluctuations can be observed [15]. It is of great interest to establish how these effects of temperature continue into the new field region made accessible by EXED.

Chapter 4

Vortex Lattice in $CeCu_2Si_2$

4.1 Heavy Fermion Superconductivity

The discovery of heavy fermion superconductors marked an important turning point in the history of superconductivity as it presented a likely candidate for exhibiting complex order parameter symmetries and a pairing mechanism that was not electron-phonon mediated in f-electron compounds.

Prior to the discovery of heavy fermion superconductors, superconductor properties were commonly studied within the context of BCS theory. BCS theory describes pairing between conduction electrons as being phonon-mediated so the Debye temperature, Θ_D, plays a large role in the energy scale. However, the discovery of $CeCu_2Si_2$ showed this to not always be the case as its Cooper pairs are made up of quasiparticles with enhanced heavy masses rather than formed from ordinary conduction electrons [102].

There are several hallmark features of heavy fermion superconductivity. The first is the size of the jump at T_C in the specific heat, ΔC, which is set by the large effective mass of the quasiparticles. The second feature is that the energy scale of the effective Fermi temperature, T_F ($= \epsilon_F/k_B$), is very low, for example in $CeCu_2Si_2$ the spin fluctuation temperature of $\approx$ 10 K serves as T_F. This means that the energy scale sequence of $T_C < T_F < \Theta_D$ observed in heavy fermions in markedly different to the characteristic frequencies of BCS theory which obey $k_B\Theta_D h \ll k_B T_F h$. These two features make it apparent that the superconductivity seen in heavy fermions is certainly not conventional [102]. Another feature is the very large orbital upper critical fields at absolute zero, $H_{c2}^{orb}(0)$ - these can be calculated using WHH (Werthamer, Helfand, Hohenburg) theory [100] from the large slopes of $\frac{dH_{c2}}{dT}_{T_c}$ near the superconducting transition temperature. Although not exclusively a property of heavy fermion superconductors, almost all of the heavy fermion superconductors seem to have a very large penetration depth λ relative to their coherence length ξ making them very strongly type-II superconductors. Table 1 illustrates the key properties of three well-known heavy fermion superconductors.

Quantity	**$CeCu_2Si_2$**	**$CeCoIn_5$**	**UPt_3**
Structure	Tetragonal	Tetragonal	Hexagonal
γ (J/mol K^2)	1	-	0.44
T_C (K)	0.7	2.3	≈ 0.5
H_{C2}^{ab} (T)	2	11.6-11.9	2.1
H_{C2}^{c} (T)	2.3	4.95	2.8
λ ($\mathring{A}$)	≈ 700	≈ 2500	4500-7400
ξ ($\mathring{A}$)	-	53-82	≈ 120

Table 1: This table summarises some of the key properties of three well known heavy fermion superconductors. The data is from [74]. Missing values for $CeCu_2Si_2$ and $CeCoIn_5$ reflects more complex behaviour.

4.2 $CeCu_2Si_2$ Properties and Crystal Structure

$CeCu_2Si_2$, the first heavy fermion superconductor, was discovered in 1979 by Frank Steglich [85]. The material is a heavy fermion with a Sommerfeld coefficient of the linear terms in specific heat γ = C/T $\approx$ 1000 mJ/molK^2. Based on the initial experimental observation that $\Delta C/\gamma T_c \approx 1.4$, it was believed that the superconducting state is carried by Cooper pairs formed by the heavy fermion quasiparticles. However it is unlikely that the superconductivity can be described by the conventional phonon-mediated theory as the Debye temperature is larger than the typical electronic energy scales in $CeCu_2Si_2$ [39].

Even though the compound was discovered almost four decades ago, there remains many unanswered questions regarding its properties. Many of the difficulties come during its growth whereby incongruent melting (when a solid substance does not melt uniformly and therefore decomposes into another solid and a liquid with varying compositions) has been an issue in the past. This has resulted in large discrepancies in the properties of $CeCu_2Si_2$ between different methods of sample preparation and annealing conditions. The magnetic and superconducting properties of $CeCu_2Si_2$ are very sensitive to the precise stoichiometry. Several ground state properties are realised within a very narrow homogeneity range of the 1:2:2 phase. A very slight Si-excess stabilises the so-called A-phase whereas a slight Cu-excess stabilises the superconducting state (S-phase). Samples with the stoichiometric 1:2:2 composition exhibit the coexistence of both the magnetic and superconducting phases (A/S-phase). A schematic phase diagram by Stockert *et al.* [88] is shown in figure 4.1. High pressure experiments doping the Si sites with Ge indicate that $CeCu_2Si_2$ is located in close proximity to a quantum critical point. It has been observed in specific heat and electrical resistivity measurements [38] that non-Fermi liquid behaviour is exhibited near the quantum critical point. It was concluded that the A-phase is a spin-density wave with a very small ordered moment, and neutron diffraction measurements [87] suggest that the spin-density wave instability is the origin of the quantum criticality. An S-type sample typically has $T_C \approx 0.7$ K and $H_{C2} = 2$ T for $H \parallel a$ and 2.3 T for $H \parallel c$.

The crystal structure of stoichiometric $CeCu_2Si_2$ is shown in figure 4.2. It has a tetragonal structure belonging to the I4/mmm space group.

4.3 Previous Studies

This section provides an overview of the main studies that have attempted to elucidate the nature of the superconductivity in S-type $CeCu_2Si_2$ in recent years.

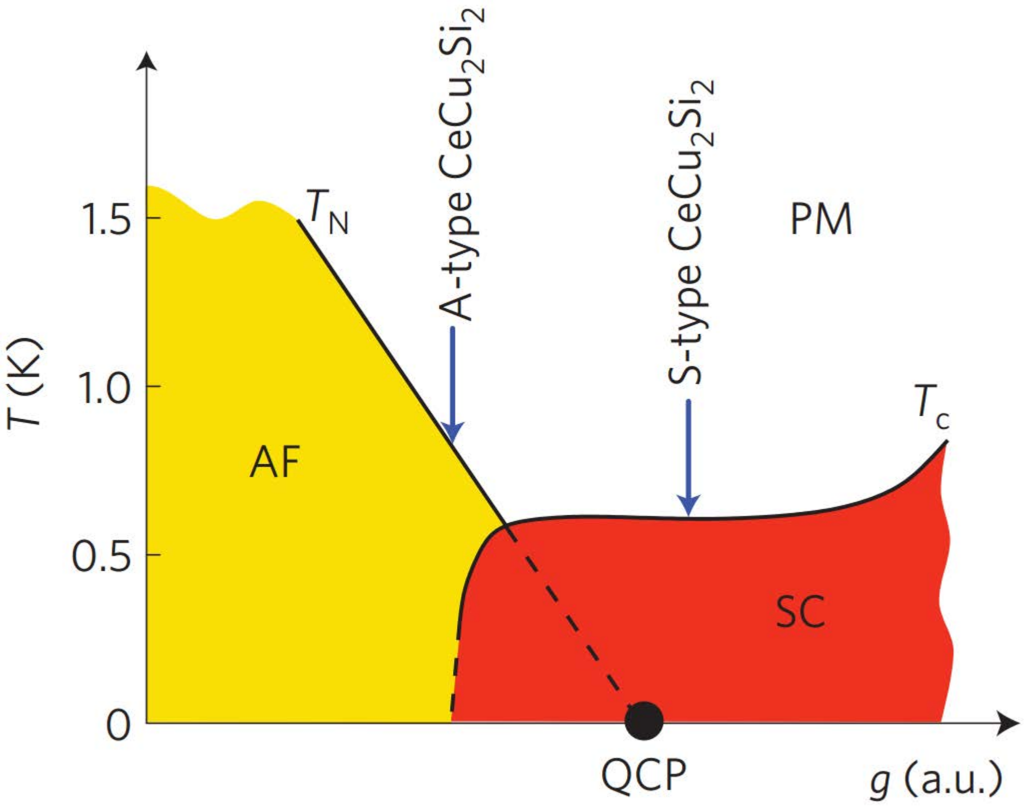

Figure 4.1: Schematic phase diagram of $CeCu_2Si_2$ displaying the main ground state possibilities in this material. The yellow section represents the antiferromagnetic phase, the red represents the superconducting phase and there is also competition between the two between the A-type and S-type samples - this is known as the A/S-type sample. Figure reproduced from [88].

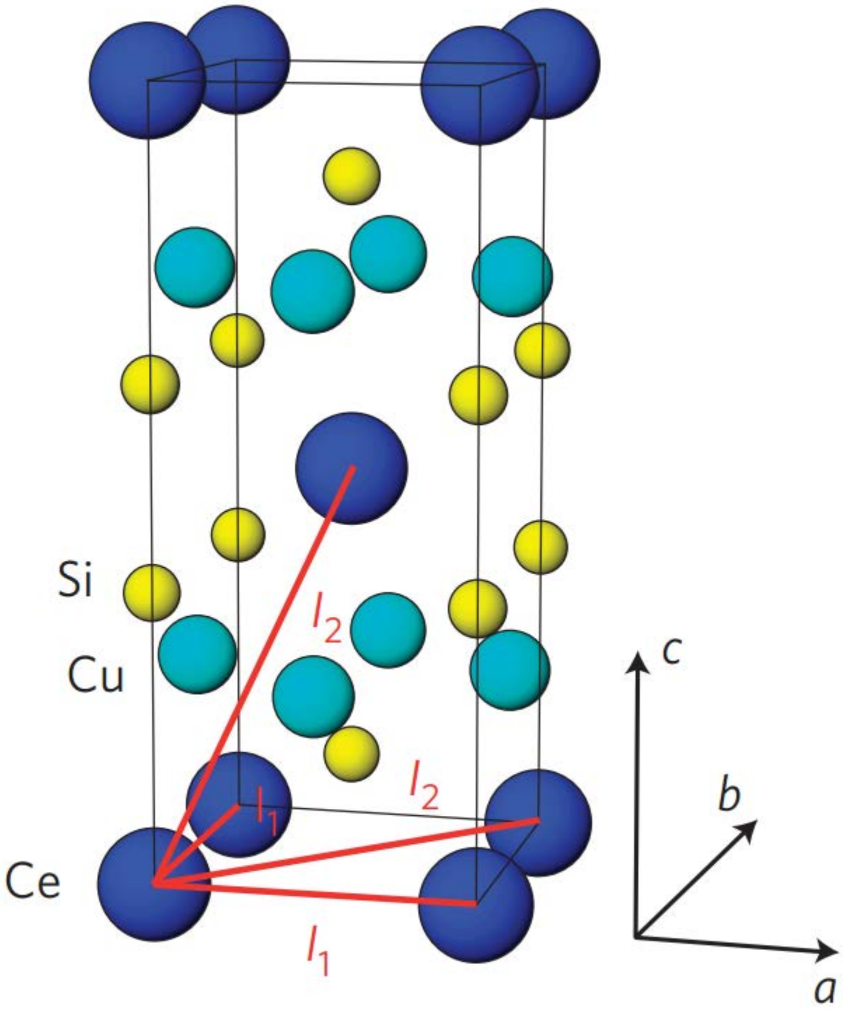

Figure 4.2: Crystal structure of $CeCu_2Si_2$. The compound has a tetgragonal structure. The Ce atoms are shown in blue, the Cu atoms are shown in teal and the Si atoms are shown in yellow. Figure reproduced from [88].

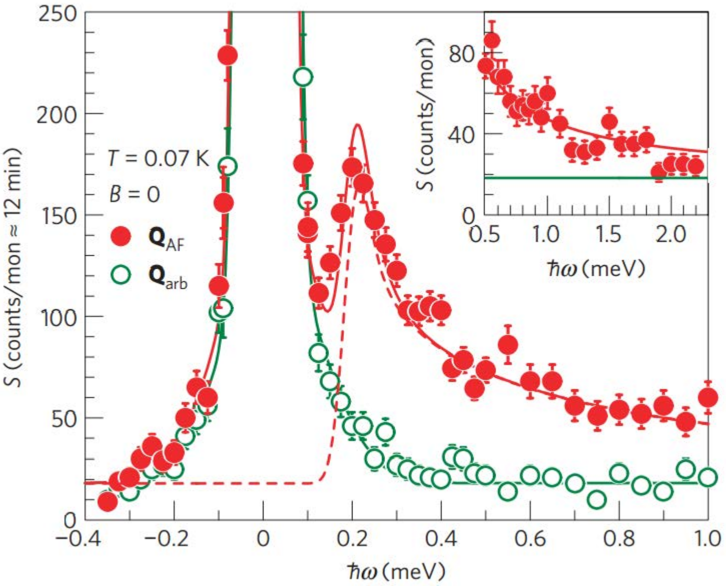

Figure 4.3: High resolution inelastic scattering spectra as a function of energy transfer at **Q** in superconducting (full circles and normal (open circles) states. The spin gap opening can be seen in the superconducting state. Figure reproduced from [88].

Stockert *et al.* [88] studied an S-type sample using high-resolution inelastic neutron scattering experiments in magnetic fields up to 2.5 T applied along the [1 1 0] axis at temperatures down to 60 mK. The authors showed that the S-type crystals have an inelastic magnetic response in the superconducting state at the same **Q** as the antiferromagnetic vector $\mathbf{Q}_{AF}$ in the A-type and A/S-type samples, as shown in figure 4.3. Therefore they share the same incommensurate wave vector which is associated to long range magnetic order as seen in the A- and A/S-type samples as well as magnetic fluctuations. The opening of the spin-excitation gap, $\hbar\omega_{gap} \approx 0.2$ meV $\approx 3.9\ k_B T_c$, removes spectral weight from lower to higher energy transfers which results in the inelastic line of this nature. When compared to the sharp signals observed in other heavy fermion superconductors (such as CeCoIn$_5$, [86]), this inelastic line can be regarded as broad. The spin excitations are part of an overdamped dispersive mode as shown in figure 4.4. Its velocity is much smaller than the strongly renormalised Fermi velocity which indicates a retardation of the coupling between the heavy quasiparticles and the quantum critical spin excitations. The authors also observed that the magnetic exchange energy saving is at least an order of magnitude greater than the condensation energy which implies that antiferromagnetic

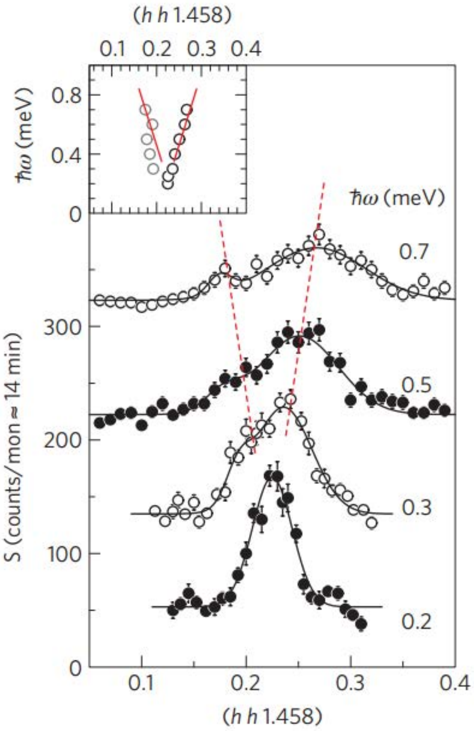

Figure 4.4: Wave vector dependence of the magnetic response for various energy transfers. Figure reproduced from [88].

excitations are the primary driving force for superconductivity.

Eremin *et al*. [30] argued that spin resonance modes in $\mathrm{CeCu_2Si_2}$ are magnetic excitons from superconducting quasiparticles. The authors analysed the dynamical magnetic susceptibility below the T_C and showed that the resonance feature evolves at the wave vector of the magnetic instability. The authors claim that the very sharp resonance found at $\mathbf{Q}_{SDW}$ in the inelastic neutron scattering measurements [87] points towards a $d_{x^2-y^2}$-wave symmetry of the superconducting gap because the order parameter sign change over the spin density wave ordering wavevector connects much of the renomalised Fermi surface. This is at odds with the study by Vieyra *et al*. [93] which determined the gap symmetry of $\mathrm{CeCu_2Si_2}$ from angle-dependent H_{C2} measurements. The resistive measurements were carried out on an S-type single crystal upon rotation within the basal tetragonal plane.

Vieyra *et al*. argue that the sharp resonance referred to by Eremin *et al*. [30] occurs in the superconducting state of 2 dimensional superconductors rather than 3 dimensional superconductors such as $\mathrm{CeCu_2Si_2}$. In $\mathrm{CeCu_2Si_2}$, as shown in the aforementioned study

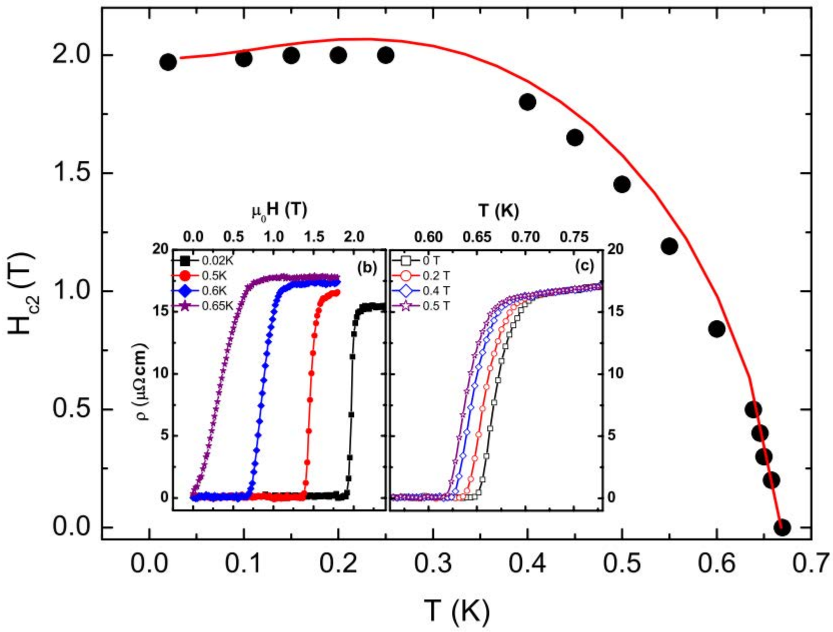

Figure 4.5: *H*-*T* phase diagram of CeCu$_2$Si$_2$ where the solid red curve is the theoretical line for *d*-wave symmetry. Resistivity measurements as a function of field and temperature are shown in the insets. Figure reproduced from [93].

by Stockert *et al*. [88], the spin-excitation gap forms out of a broad magnetic response which is an order of magnitude larger than the gap energy. Therefore Vieyra *et al*. believe that it is too soon to simply attribute this inelastic line in the inelastic neutron scattering data as $d_{x^2-y^2}$-wave state. Instead they show that a weak coupling BCS theory model can describe the upper critical field behaviour of CeCu$_2$Si$_2$ after having included Pauli limiting in the calculation. The temperature dependence of the upper critical field is reproduced by the calculation, as shown in figure 4.5. Ultimately they come to the conclusion that the order parameter has a d_{xy} symmetry based on the angle-resolved resistivity measurements of H_{C2} which exhibits a four-fold symmetry. However, Wang *et al*. [94] are critical of the conclusion reached by Vieyra *et al*. [93] as they claim that it is not appropriate to fit the angle-resolved upper critical field for a specific temperature. The authors claim that a more appropriate method to deduce the gap symmetry from experiments of the in-plane H_{C2} is by measuring the angular dependence of the upper critical field at various temperatures and to check whether there is a $\pi/4$ shift at a certain critical temperature T^*, where $T < T^*$ along nodal directions and $T^* < T < T_C$ along the antinodal directions.

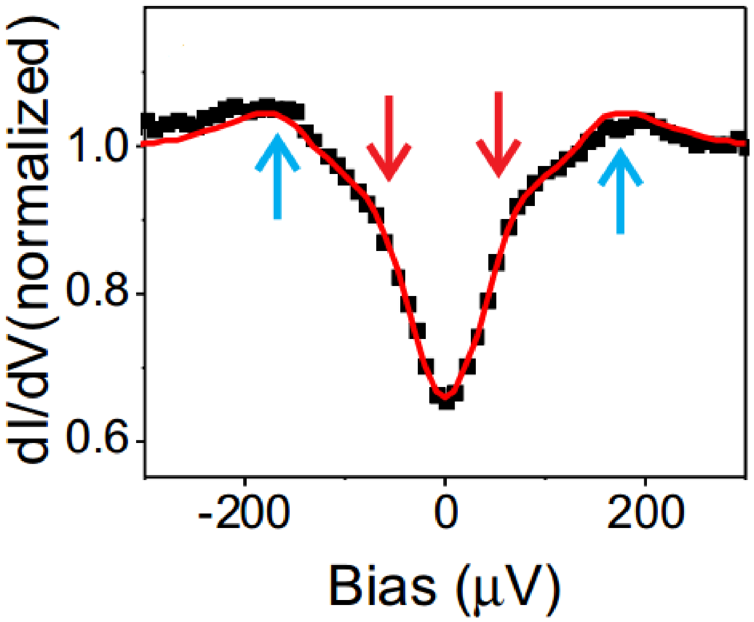

Figure 4.6: Tunneling spectrum at 20 mK exhibiting a gap-like feature. The blue arrows indicate the main gap and the red arrows indicate the low energy shoulder. The red line is the best fit for the gap that describes the *d*-wave symmetry at low energies and also the gap that describes the *s*-wave symmetry at high energies. Figure reproduced from [27].

A detailed low temperature study of the specific heat and magnetisation was carried out by Kittaka *et al.* [55] on a high quality single crystal. The authors acknowledged that the debate, at that time, was whether gap symmetry is $d_{x^2-y^2}$ or d_{xy}. The authors showed that the temperature dependence of the specific heat exhibits an exponential decay with a two-gap feature. The field dependence of the specific heat also indicated multiband superconductivity as C_e/T at 0.6 T showed a kink at 65 mK and then decreased rapidly as it was further cooled. At high fields, anomalous behaviour was attributed to Pauli-paramagnetic effects which are expected to be strong in this compound. Therefore they believed that CeCu$_2$Si$_2$ is nodeless which implies that the gap is fully open in the heavy mass bands as the specific heat is sensitive to the heavy quasiparticle contribution.

The first and only other study of the vortex lattice state of CeCu$_2$Si$_2$ was carried out by Enayat *et al.* [27] using the STM method. They observed, at 20 mK, that the differential tunneling conductance measured on the surface reveals a gap-like feature on an energy scale of 100 μeV which is attributed to the superconducting gap. The authors

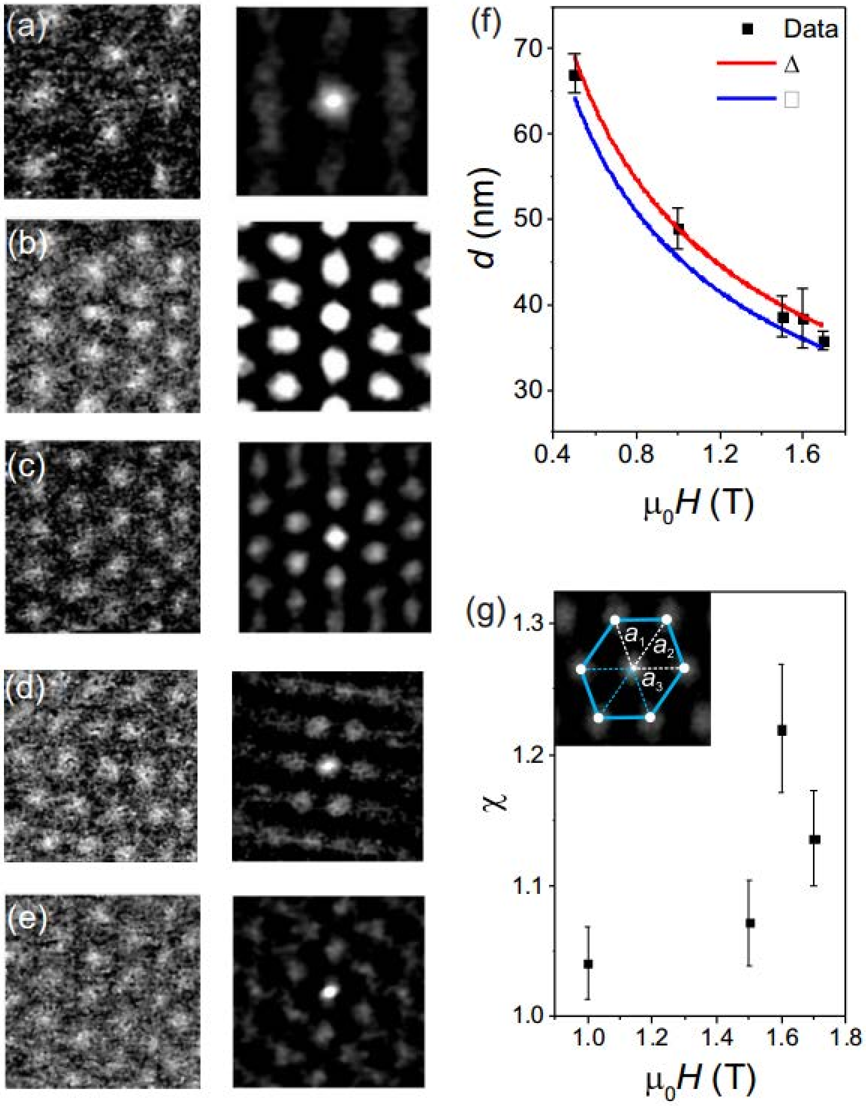

Figure 4.7: (a)-(e) Spatial maps of the zero bias tunneling conductance at 200 mK in fields of 0.5, 1, 1.5, 1.6 and 1.7 T. A triangular vortex lattice can be seen at all fields. (f) The vortex core separation at a function of magnetic field. (g) The vortex lattice anisotropy as a function of magnetic field. The inset shows how the anisotropy is extracted from the 1.6 T data as an example. Figure reproduced from [27].

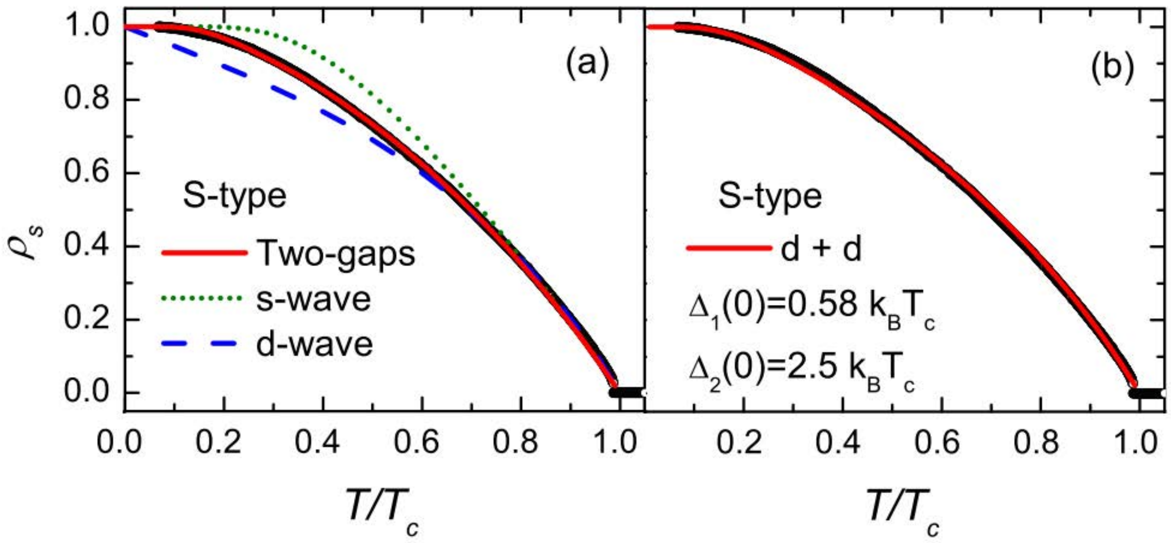

Figure 4.8: (a) The superfluid density of $CeCu_2Si_2$ fitted with two fully open gaps, an *s*-wave model and a *d*-wave model. (b) The superfluid density fitted with a $d + d$ band mixing pairing model. Figure reproduced from [72].

used different models to describe the gap; they found that the low energy features could be described by a superconducting gap with a *d*-wave symmetry and the high energy features could be described a superconducting gap with an *s*-wave symmetry. This is shown in figure 4.6.

The vortex lattice was observed from spatial maps of the zero bias tunneling conductance in various magnetic fields up to 1.7 T (parallel to the *c*-direction) as shown in figure 4.7. An isotropic *s*-wave gap usually implies a triangular vortex lattice. Having analysed the distance between the vortex cores as a function of magnetic field from the spatial maps along the high symmetry direction, it is revealed that the behaviour is consistent with a triangular Abrikosov lattice. However a distortion can be seen in the data, shown in figure 4.7(g), away from a regular triangular symmetry - the distortion is largest at 1.6 T ($\approx 0.7H_{C2}$). This distortion indicates an anisotropic interaction between the vortex cores. The features observed in the tunneling spectra, i.e. the lack of evidence for anisotropy in the shapes of vortex cores, supports a multigap scenario. The magnetic field dependence of the zero bias tunneling conductance also agrees with the specific heat measurements by Kittaka *et al*. [55], which therefore strengthens the multiband scenario.

Recent London penetration depth measurements by Pang *et al.* [72] indicate fully gapped behaviour at very low temperatures in agreement with Kittaka *et al.* [55]. The authors propose a nodeless $d + d$ band-mixing pairing state, which yields good fits to the superfluid density (shown in figure 4.8(b)) and the specific heat, as the superconducting order parameter of $\mathrm{CeCu_2Si_2}$. This state has the required sign change of the order parameter along the antiferromagnetic vector $\mathbf{Q}_{AF}$ on the Fermi surface deduced from the inelastic neutron scattering measurements by Stockert *et al.* [88].

A very recent study by Yamashita *et al.* [112] reported low temperature specific heat, thermal conductivity and penetration depth measurements in $\mathrm{CeCu_2Si_2}$. The measurements indicate the absence of gap nodes at any point on the Fermi surface. They also show, by electron irradiation, that the superconductivity is robust even when the electron mean free length is shorter than the coherence length ξ. The authors claim that this is indicative of superconductivity which is robust against impurities. This implies that there is no sign change in the gap function ruling out d-wave and $s_{\pm}$-wave states as unlikely scenarios. $d_{xy} + id_{x^2-y^2}$ and $s + id_{x^2-y^2}$, which are unconventional states with irreducible representations of the gap function, can be ruled out due to their sensitivity to impurities, and also because these states are not degenerate, therefore two superconducting transitions would be expected. Accidental degeneracy would be broken by pressure or doping, but previous measurements have not exhibited two superconducting transitions under pressure or by doping. The authors come to the conclusion that the pairing in $\mathrm{CeCu_2Si_2}$ is a fully gapped non sign-changing s-wave state [112], which contradicts the claims of the other studies discussed above.

The previous studies on $\mathrm{CeCu_2Si_2}$ fail to provide any clear agreement regarding the nature of the superconductivity. Perhaps the most unexpected results are from Yamashita *et al.* [112] as the fully gapped s-wave state contradicts virtually every other study summarised in this section which indicate that the pairing mechanism is unconventional. It is also highly unlikely that the conventional electron-phonon interaction could overcome the on-site strong Coulomb repulsive force, which enhances the effective mass to approximately 1000 times the bare electron mass, in this material which lacks high energy strong-coupled phonons. The gap function is therefore likely to be unconventional, though the precise nature appears to vary between samples and experimental techniques. This could be due to the large range of sample quality depending on the method of growth and the exact stoichiometry of the sample. Also, the STM study is sensitive to the sample surface quality (the sample used for the STM study came from the same growth as the measurements in the Result section of this chapter, but SANS is far less sensitive to sample surface quality). What can be claimed with more certainty at this stage is that the pairing interaction is driven by strong magnetic fluctuations as the superconductivity occurs in the vicinity of a quantum critical point.

4.4 $\mathbf{CeCoIn_5}$ as Comparison

$CeCoIn_5$ has been heavily studied by various techniques due to the fact that it can be fairly easily grown as ultraclean single crystals, and its T_C of 2.3 K means that the superconducting state is more accessible than other Ce-based heavy fermion superconductors such as $CeCu_2Si_2$. Techniques such as angular and temperature dependence of the thermal conductivity [70, 49] and angular dependence of the specific heat [91] have confirmed the $d_{x^2-y^2}$-wave symmetry of $CeCoIn_5$.

This material is a Pauli-limited superconductor which means that the superconductivity is destroyed by the coupling of the magnetic field to the spin of the electrons rather than by orbital supercurrents [53]. Ichioka and Machida [45] showed that a superconductor with strong Pauli paramagnetic effects has paramagnetic moments around its vortex cores. This has been confirmed by small angle neutron scattering experiments which exhibit unusual properties of the vortex lattice behaviour in $CeCoIn_5$ [9, 109].

Figure 4.9 shows that the vortex lattice intensity (shown as the square of the form factor) increases with field which is in contrast to superconductors that are not Pauli-limited whereby the intensity typically decreases exponentially with field. The additional

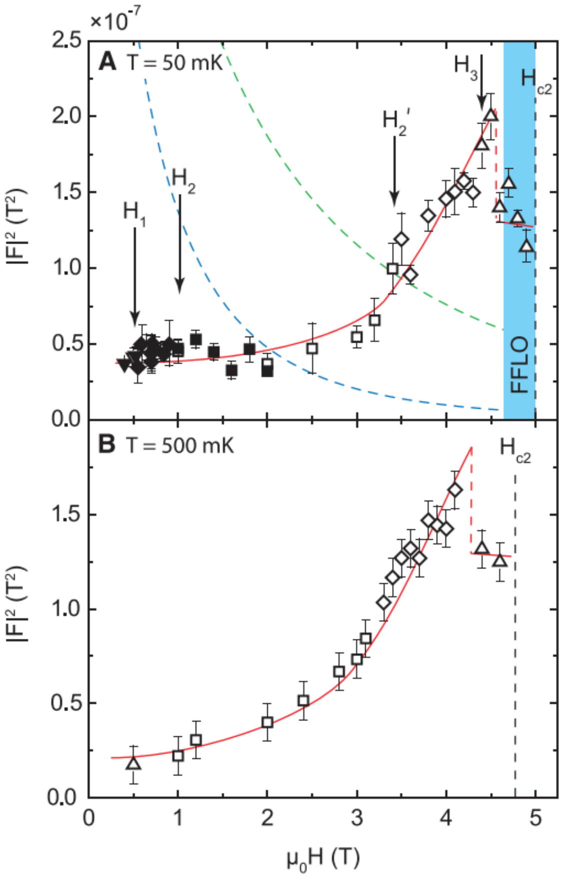

Figure 4.9: (A) The field dependence of the vortex lattice form factor at 50 mK for $CeCoIn_5$ (B) The field dependence of the vortex lattice form factor at 500 mK. Figure reproduced from [9].

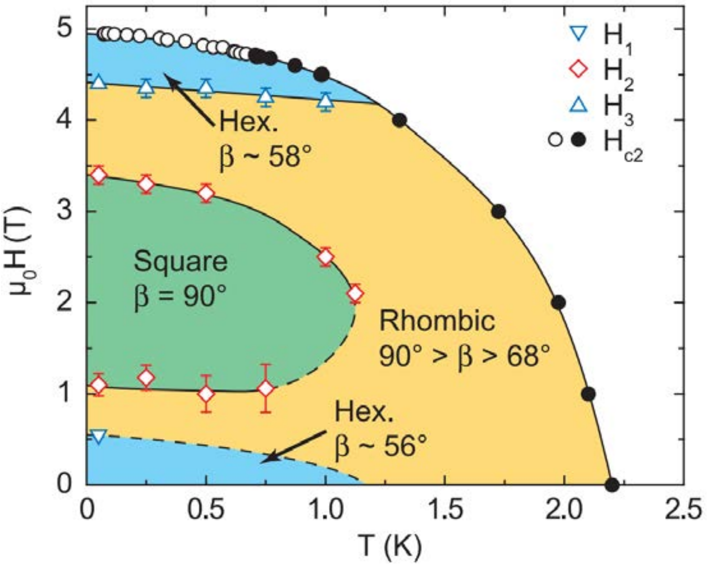

Figure 4.10: Vortex lattice structure phase diagram for $CeCoIn_5$ with the field parallel to the *c*-axis. Figure reproduced from [9].

intensity with field is indicative of paramagnetism in the vortex cores that increases in strength as the field is increased.

Figure 4.10 shows the complex vortex lattice phase diagram of $CeCoIn_5$ whereby the vortex lattice changes with both field and temperature. At the lowest measured temperatures the structure goes from triangular to rhombic to square to rhombic with increasing field, and remarkably goes back to triangular as H_{C2} is approached. A triangular vortex lattice arrangement is expected at low fields where the gap symmetry does not have a significant effect as the vortices are spaced well apart but as the field is increased and the vortices move closer together a square arrangement is expected due to the increasing significance of the symmetry of the gap function. Close to H_{C2} it seems the gap symmetry once again plays a minimal role as the arrangement of the vortices returns to triangular. This reentrant behaviour of a rhombic lattice transitioning back to triangular with increasing field has not been observed in any other superconductor.

4.5 Sample Preparation

The SANS experiment used a 2.0 g S-type single crystal provided by Oliver Stockert which was also used in an inelastic neutron scattering study [88]. The sample has a zero field $T_C = 0.7$ K and $H_{C2} = 2.3$ T for $H \parallel c$.

The single crystals were grown using a self-flux method combined with a Bridgman cooling technique by Seiro *et al*. [78]. The procedure began using polycrystals of nominal composition $Ce_xCu_2Si_2$ ($0.95 \leq x \leq 1.1$) which were obtained in an arc furnace under Ar atmosphere. The ingots produced by this are put in a crucible (Al_2O_3) together with a 40 mol% excess Cu as self-flux. The crucible is then heated up to approximately 1550°C for between 15 and 30 minutes and then cooled down.

Wavelength-dispersive X-ray spectroscopy was used to check the composition of the grown crystals by comparing to pure Copper and Ce_5Si_4. X-ray powder diffraction was used to determine the lattice parameters of the single crystals. A Quantum Design PPMS

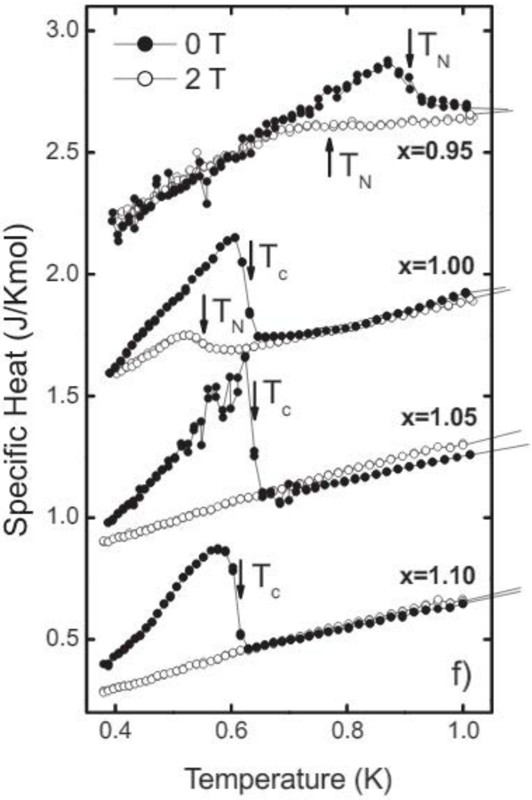

Figure 4.11: Specific heat vs. temperature for different Ce content x. Figure reproduced from [78].

was used to then measure the specific heat down to 0.4 K.

The crystal structure was found to be I4/mmm tetragonal for all crystals. The crystals with a higher Cu/Si ration exhibit superconductivity. The transition is seen by the sharp peak in figure 4.11 which vanishes as a field of 2 T is applied. The sample used in the measurements for this thesis only exhibit a superconducting ground state unlike the lower Cu/Si ratio samples (x = 0.95, 1.00) which show an antiferromagnetic transition.

The single crystal was mounted onto a pure aluminium sample holder with hyrogen-free Cytop©, as shown in figure 4.12. Aluminium was used for the sample holder as it is almost entirely transparent to neutrons. The sample was mounted such that the crystal c-axis was parallel to the applied field. The sample is shown in figure 4.13 where the c-direction is labelled - this also indicates the direction that the field was applied.

Figure 4.12: $CeCu_2Si_2$ mounted on the aluminium sample holder which is to be placed in the dilution fridge of the 17 T horizontal cryomagnet described in chapter 2.

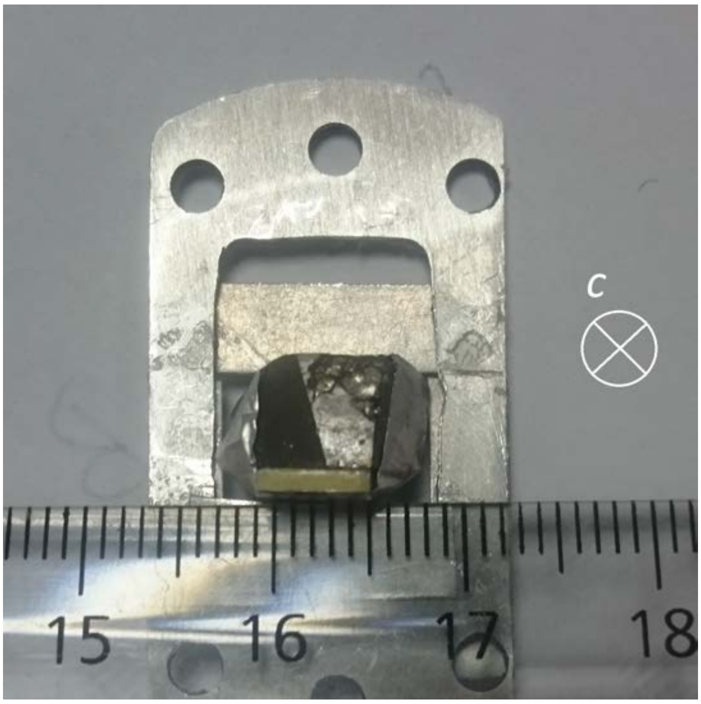

Figure 4.13: $CeCu_2Si_2$ sample mounted on the aluminium holder. The *c*-axis direction is labelled. The field is applied parallel to the *c*-axis.

4.6 Results

The results in this section are formed by a series of measurements taken on the D33 instrument at the ILL, Grenoble in July 2016. Prior to the beamtime at ILL, we also measured the vortex lattice at PSI, Switzerland, but beyond proving that the vortex lattice could be observed via SANS, we did not obtain further data from that for further analysis. The experiment was carried out by me with assistance from Alexander Holmes, Ted Forgan, Elizabeth Blackburn, Stephen Pollard, and Philippa Jefferies (along with the instrument support staff which included Robert Cubitt).

Most measurements had the following instrument parameters: $\lambda_{neutron} = 6$ Å, collimation = 12.8 m, and detector distance = 13.0 m.

4.6.1 Vortex Lattice Structure

The vortex lattice state is induced by applying a magnetic field larger than the lower critical field, H_{C1}, and smaller than the upper critical field, H_{C2}. The precise field applied between this range has the potential to induce phenomena such as structural transitions of the vortex lattice as seen in other superconductors, such as $YBa_2Cu_2O_7$. The measurements in this section were all done at 130 mK and 350 mK.

We observe an approximately isotropic hexagonal vortex lattice structure across the entire field range. Figures 4.14 to 4.17 show the evolution of the vortex lattice with field (all are plotted on the same intensity scale). The vortex lattice was prepared using the oscillating field cool method described in Chapter 2. All *d*-wave superconductors, such as $YBa_2Cu_3O_7$ and $CeCoIn_5$, exhibit a hexagonal-to-square vortex lattice structural transition with increasing field. The lack of a structural transition in $CeCu_2Si_2$ encourages us to rule out the possibility of it possessing a pure *d*-wave superconducting gap, like $CeCoIn_5$ was proven to have [9, 109].

The hexagonal vortex lattice is very slightly anisotropic - although it is not consistently extending in any particular direction with field, nor is the anisotropy obviously increasing

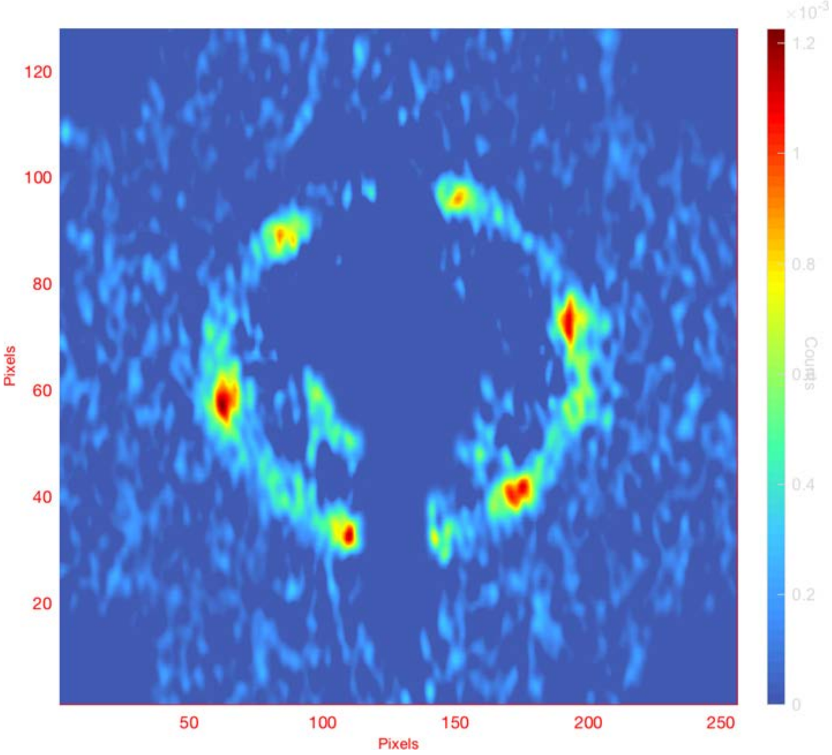

Figure 4.14: Vortex lattice diffraction pattern at 0.8 T and 130 mK.

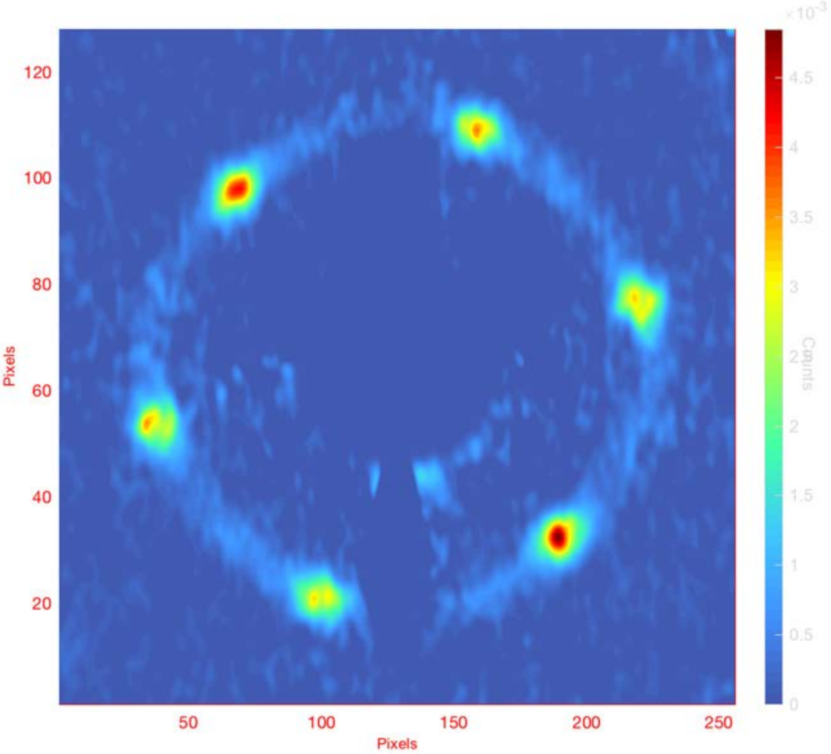

Figure 4.15: Vortex lattice diffraction pattern at 1.5 T and 130 mK.

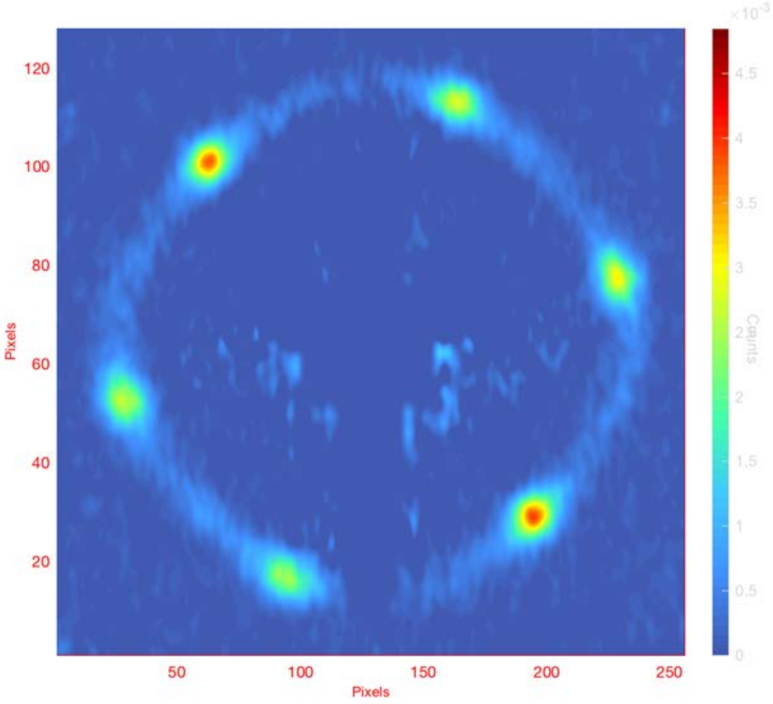

Figure 4.16: Vortex lattice diffraction pattern at 1.8 T and 130 mK.

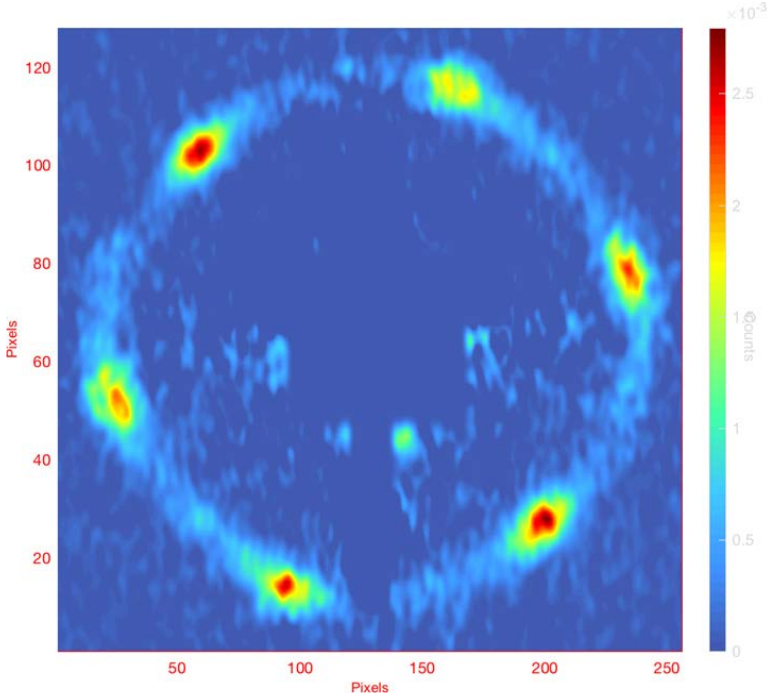

Figure 4.17: Vortex lattice diffraction pattern at 2 T and 130 mK.

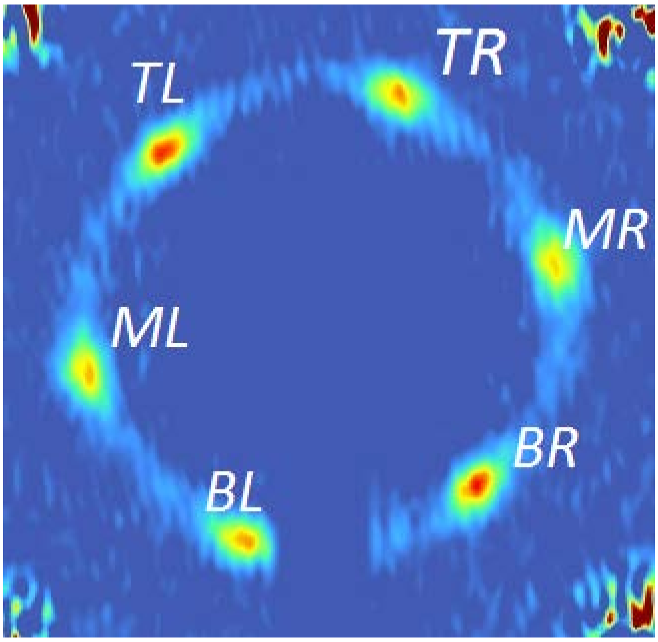

Figure 4.18: Vortex lattice diffraction pattern at 1 T and 130 mK with labels at each spot. The labels are used to describe the small distortions with field in figure 4.19.

with field. There are relatively small distortions of the Bragg spots at all measured fields when compared to where they are expected to be assuming an isotropic hexagonal vortex lattice. There does not appear to be any clear pattern of the vortex lattice distortion as a function of field, so the origin of the distortion is unknown. The evolution of the distortion, described by q, as a function of field is shown in figure 4.19. The expected q is also plotted in black (Q calculated).

Figure 4.20 shows the field dependence of the rocking curve FWHM at 130 mK. All rocking curves were obtained under identical experimental conditions, i.e. identical collimation and detector-to-sample distance. The FWHM of the rocking curves describes the perfection of the vortex lattice. It is clear that the FWHM varies little with field indicating that any vortex lattice disorder is insignificant. This also indicates that we are instrumental-resolution limited. We were able observe the vortex lattice at higher temperatures at 0.8 T compared with 1.6 T due to the decreased T_c with increasing field.

The vortex lattice structure appears to be independent of temperature. As shown in figure 4.21, it can be seen that despite the larger errors at higher temperatures, the vortex lattice spots are once again controlled by the instrumental resolution.

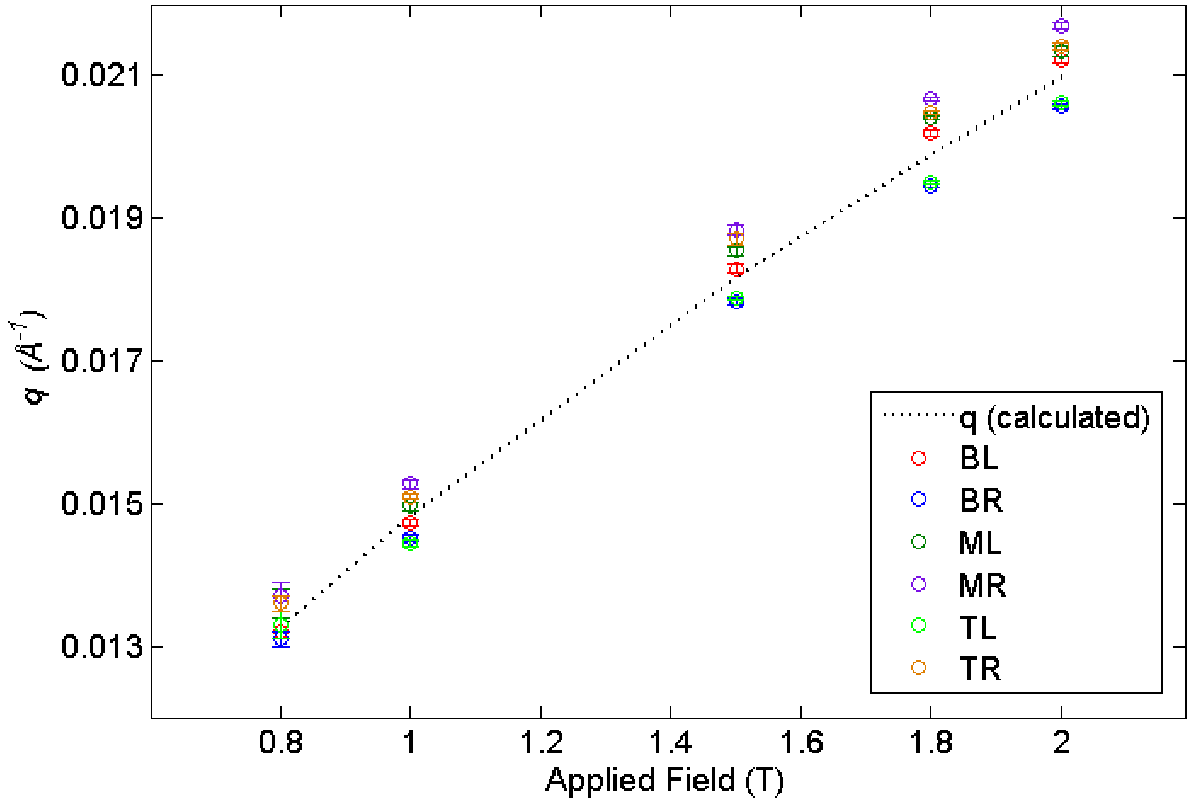

Figure 4.19: The evolution of the vortex lattice spot-position distortion with field. The labels are described in figure 4.18. The dashed line represents the ideal q for a hexagonal lattice as a function of field.

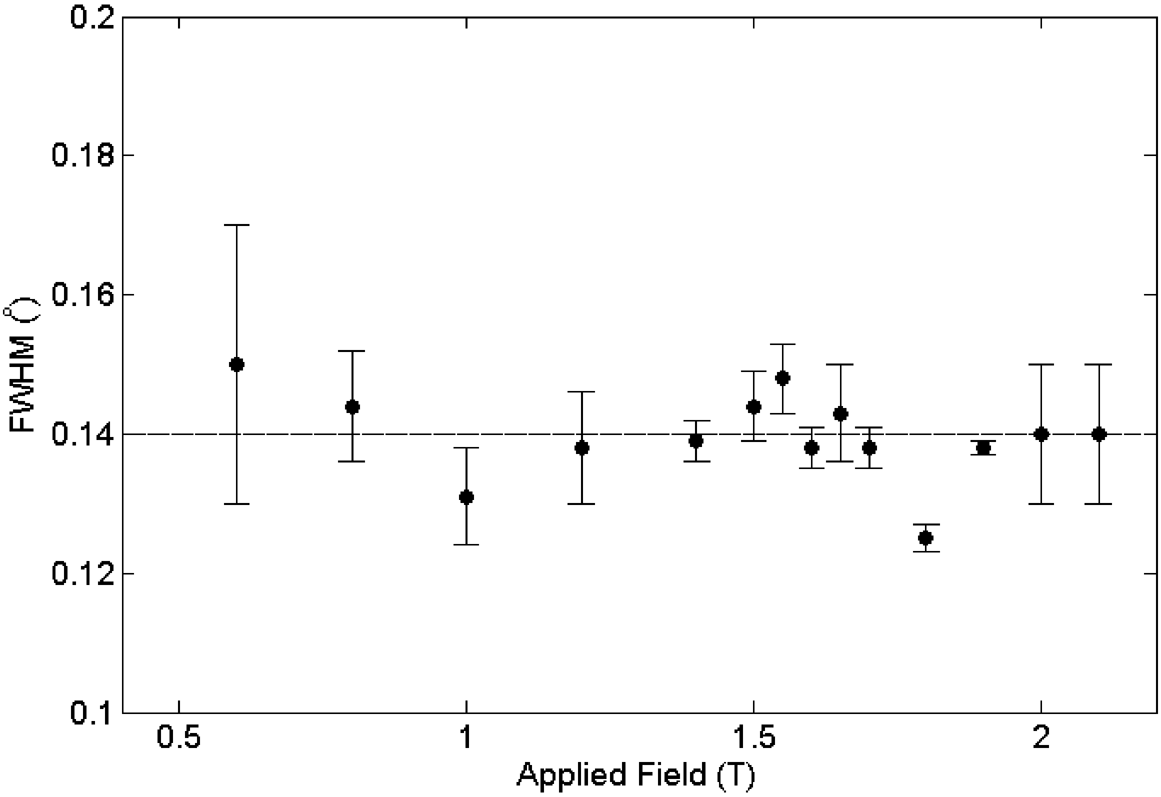

Figure 4.20: The field dependence of the FWHM of the rocking curves at 130 mK. It is clear that the rocking curve widths (fitted as shown in figure 2.9) remain almost identical, and therefore the vortex lattice is not disordered. The rocking curve widths also lie close to the instrumental resolution at all measured fields. A straight line has been added as a guide to the eye.

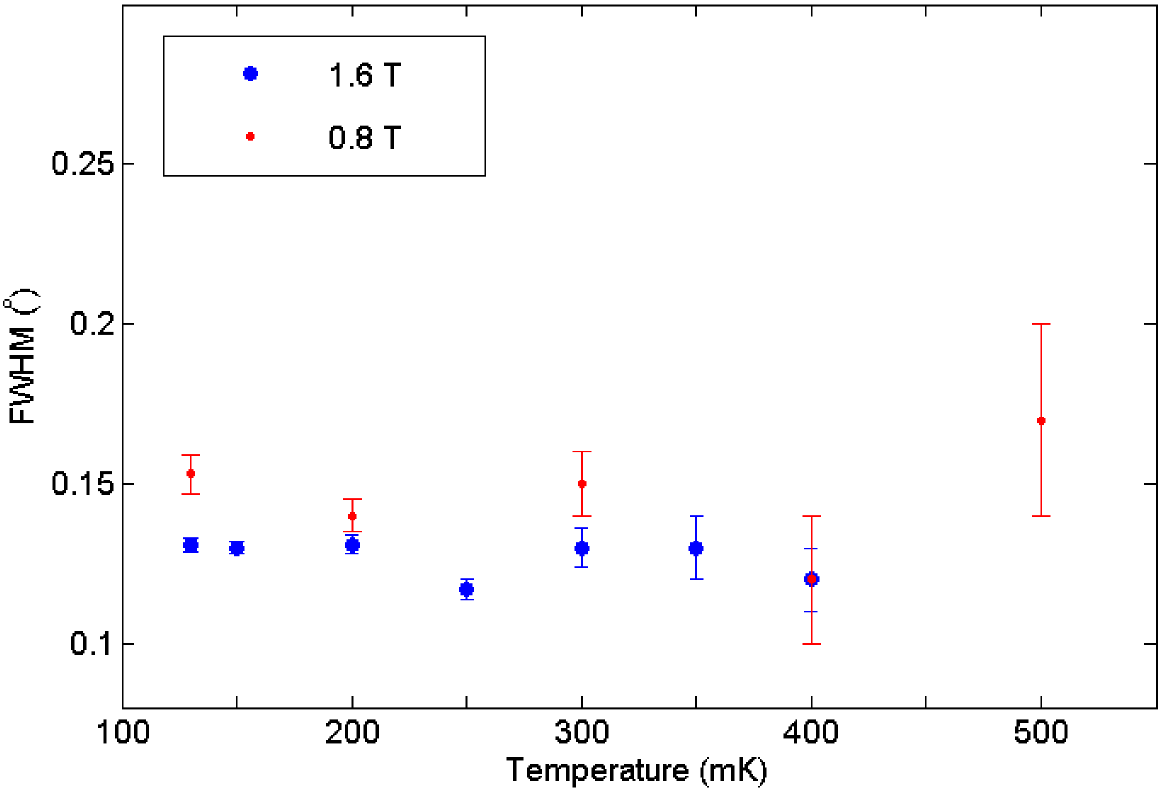

Figure 4.21: The temperature dependence of the rocking curve widths at 0.8 T and 1.6 T.

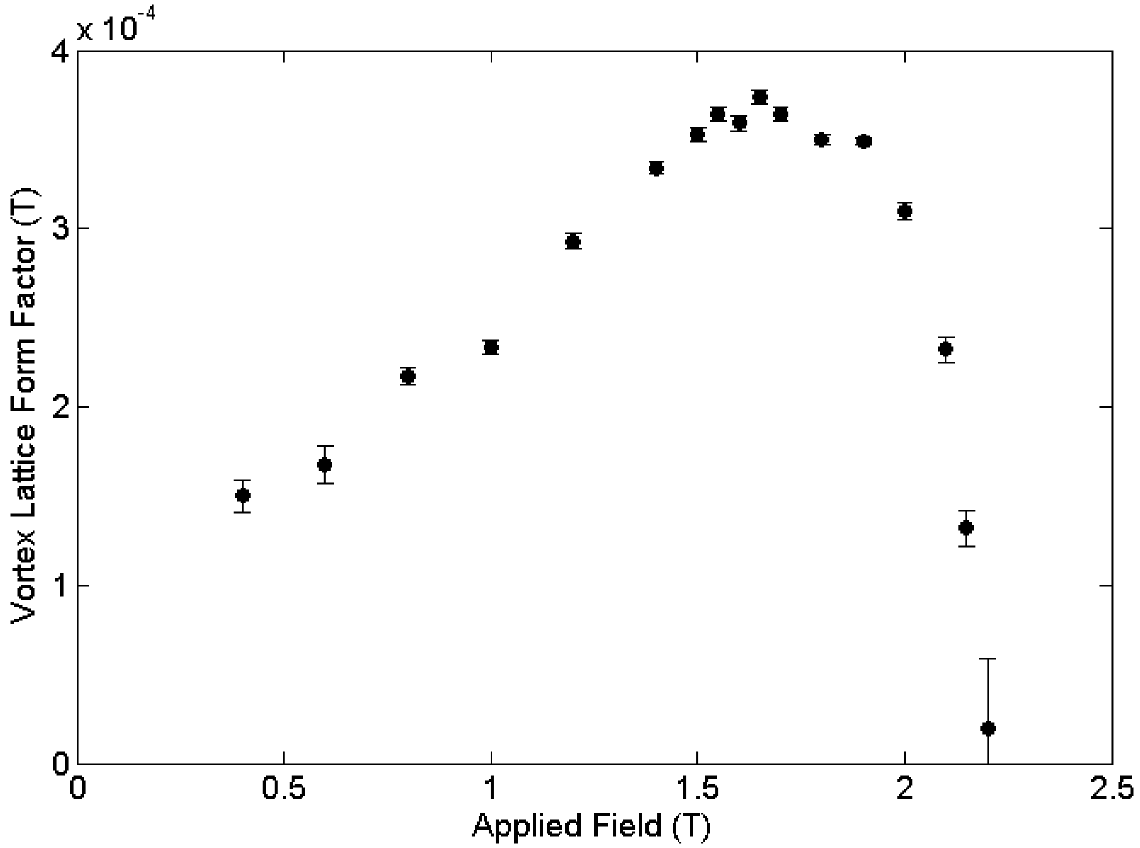

Figure 4.22: The vortex lattice form factor as a function of applied field at 130 mK. These measurements were taken at with a neutron wavelength $\lambda_n = 6$ Å .

4.6.2 Vortex Lattice Form Factor

The initial measurements to extract the form factor were done under the following instrumental configuration of a 12.8 m collimation length, a 13 m detector distance and a neutron wavelength of 6 Å . This configuration was chosen to measure as many fields as possible under a single set of parameters. We were able to measure here between 0.4 T to 2.15 T at 130 mK, as shown in figure 4.22.

The present configuration would not allow for any measurements lower than 0.4 T due to the large levels of noise near the centre of the detector (which is the location of the region of interest at these low fields under these beam conditions). This required us to adjust the beam configuration slightly. The collimation length and detector distance were kept fixed, but the neutron wavelength was increased to 10 Å . This allowed the Bragg

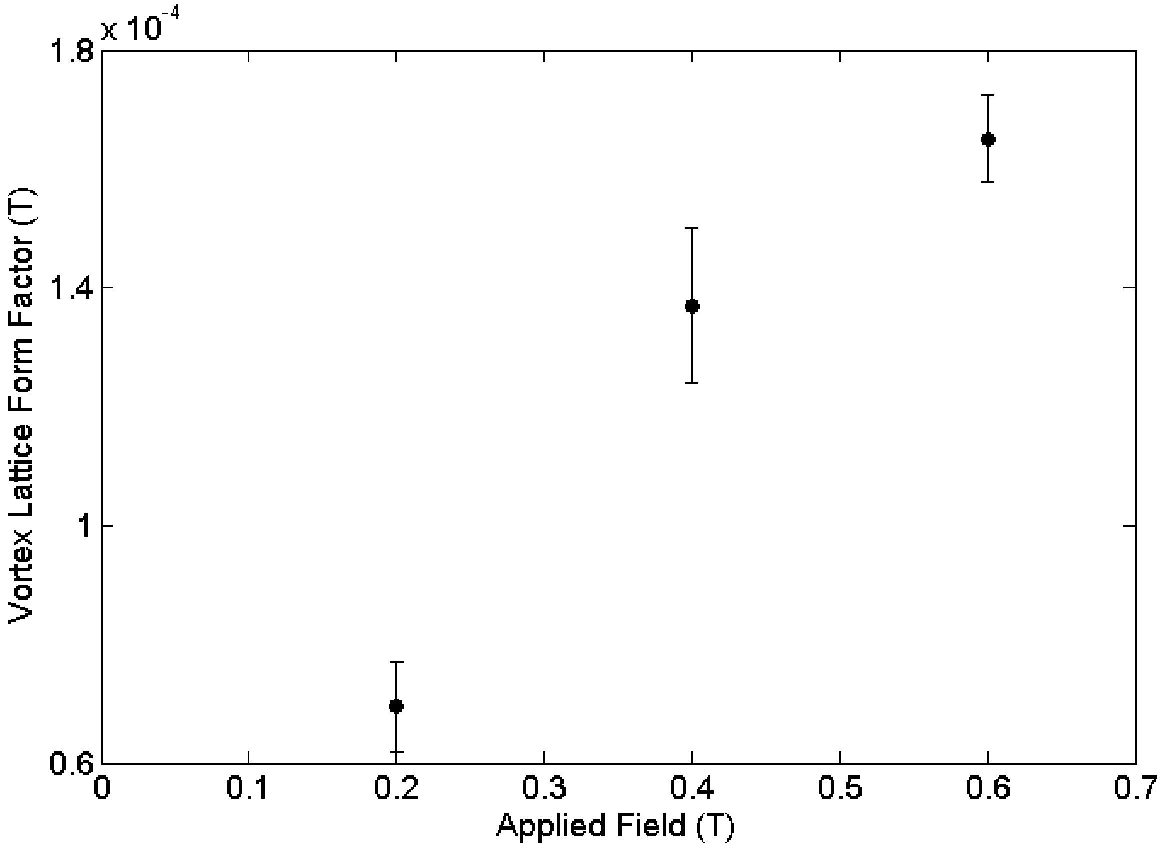

Figure 4.23: The vortex lattice form factor as a function of applied field at 130 mK. These measurements were taken at with a neutron wavelength $\lambda_n = 10\ \mathring{A}$.

spots at low field to move away from the noise-filled centre of the detector. Three fields were measured with $\lambda_n = 10$ Å , as shown in figure 4.23.

The results can be combined by comparing the direct beam intensities of the two configurations. The neutron beam intensity is considerably higher at 6 Å so the low field 10 Å data must be scaled up to make it directly comparable with the higher field data. This is shown in figure 4.24. This increase in the vortex lattice form factor at low fields is indicative of Pauli-limited superconductivity. In superconductors which do not have a paramagnetic contribution in the vortices, the vortex lattice form factor should decrease with increasing field as the vortex cores overlap.

To demonstrate the discrepancy between the observed vortex lattice behaviour compared to what is typically expected, we have fitted the field dependence of the form factor

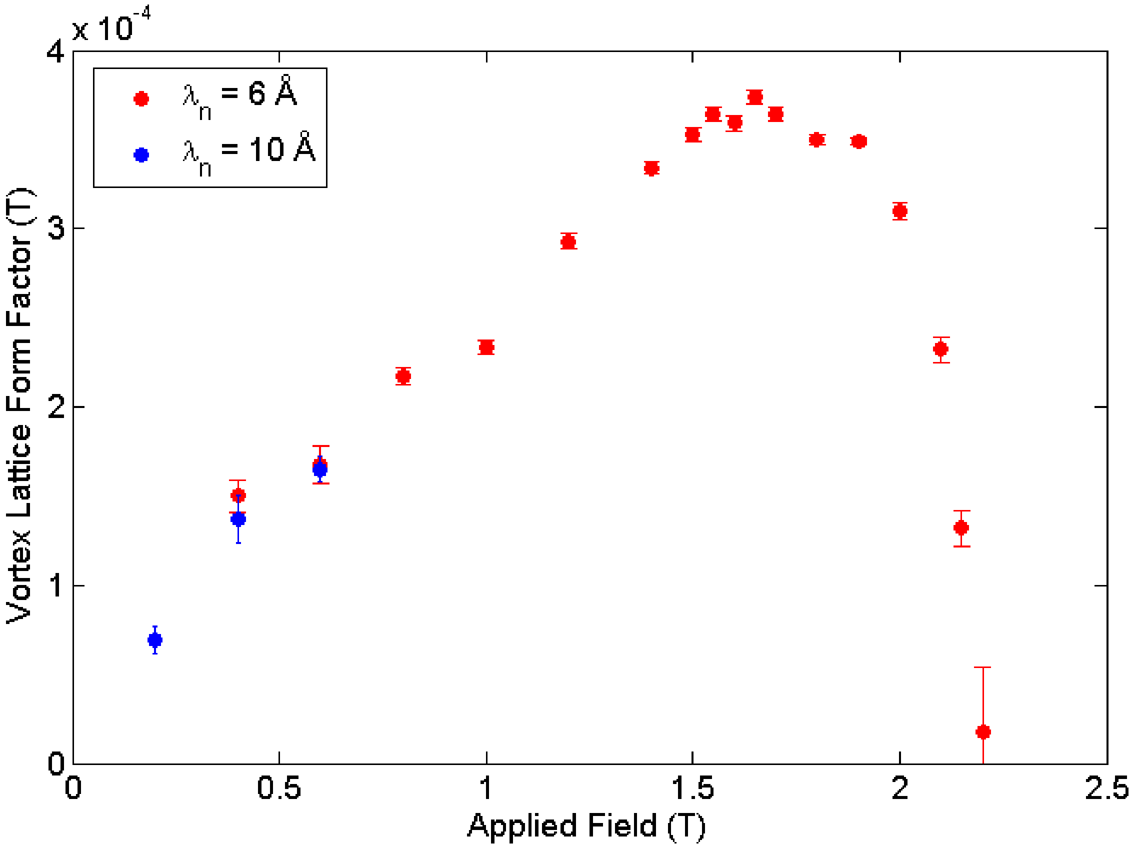

Figure 4.24: The vortex lattice form factor as a function of applied field at 130 mK. This graph shows the combination of the data collected in figures 4.22 and 4.23.

to the non-local London model:

$$F_q = \frac{\langle B \rangle}{1 + q^2\lambda^2} e^{-cq^2\xi^2} \tag{4.1}$$

where $\langle B \rangle$ is the average induction, q is the magnitude of the wavevector $\boldsymbol{q}$ defined earlier, ξ is the coherence length, λ is the penetration depth, and c ($= 0.5$) is an empirical core cutoff parameter. This is the non-local version of the London model described in equation 3.4; the difference being the inclusion of the exponential term which caters for the finite size of the cores of the vortices. This has been fitted to the vortex lattice form factor data in figure 4.25 with two values of the penetration depth, λ_L ($=$ 500, 700 nm) from Pang *et al.* [72], and a single value of the coherence length, ξ ($=$ 7 nm), from Enayat *et al.* [27]. It is clear to see that this model is not remotely compatible with the enhanced form factor experimentally observed at low fields in $\mathrm{CeCu_2Si_2}$.

Field-dependence of the Vortex Lattice Form Factor at Higher Temperature

We also studied the field dependence of the vortex lattice form factor at 350 mK, as shown in figure 4.26. It can be seen that the form factor is still increasing with field at low fields, however the cross-over field whereby the vortex lattice form factor appears to begin decreasing with field occurs at a lower field than for the 130 mK measurements (although there are not enough measurements between 1.4 and 1.7 T are required to confirm the precise cross-over field for 350 mK).

It is clear in figure 4.27 that there is a temperature dependence to the vortex lattice form factor at all measured fields, however the overall behaviour (increasing at low fields and decreasing as the upper critical field is approached) is essentially temperature-independent. In $\mathrm{CeCoIn_5}$, the form factor data only becomes temperature dependent when moving to higher fields, where the increase of the form factor at higher fields is more slowly suppressed with temperature. The progressive suppression of the form factor also appears to be apparent here at higher temperatures, however, in contrast with

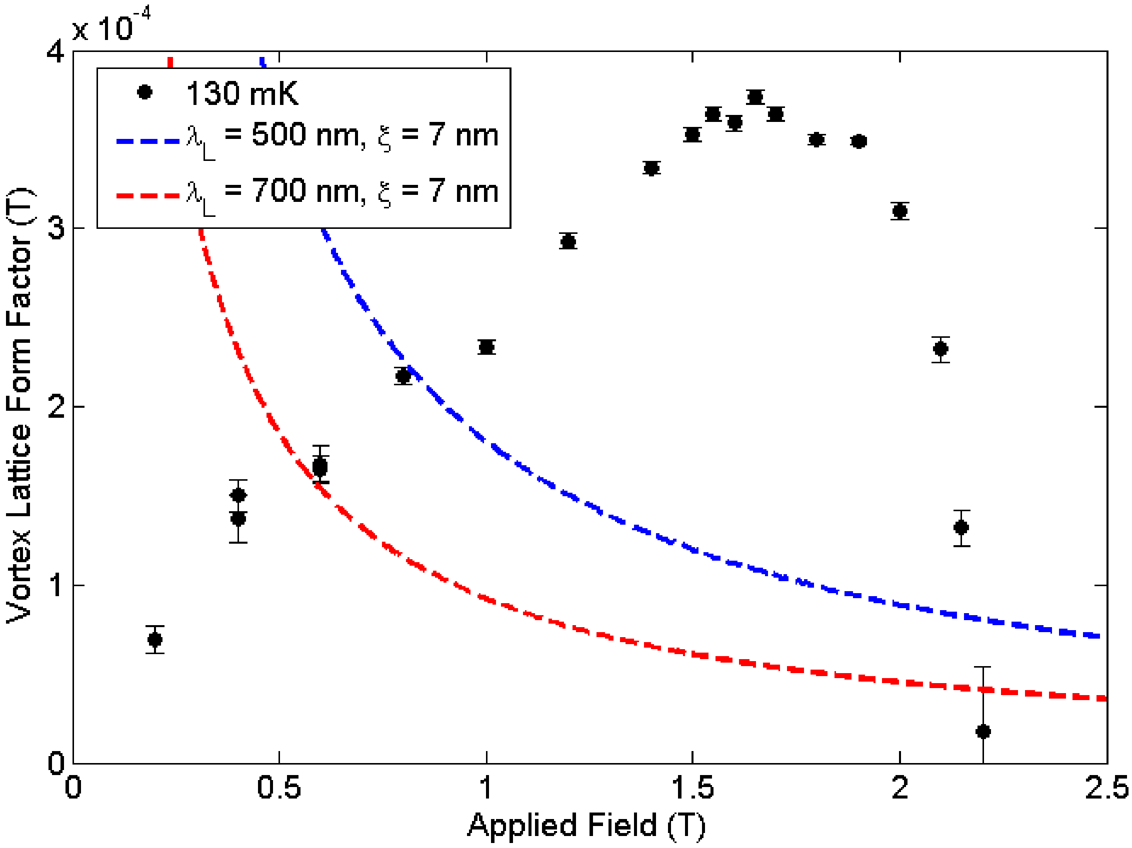

Figure 4.25: The field-dependence of the vortex lattice form factor in $CeCu_2Si_2$ at 130 mK for $H \parallel c$. The red and blue dashed lines are representative of the field-dependence of the vortex lattice form factor in accordance with the London model with reasonable fitting parameters.

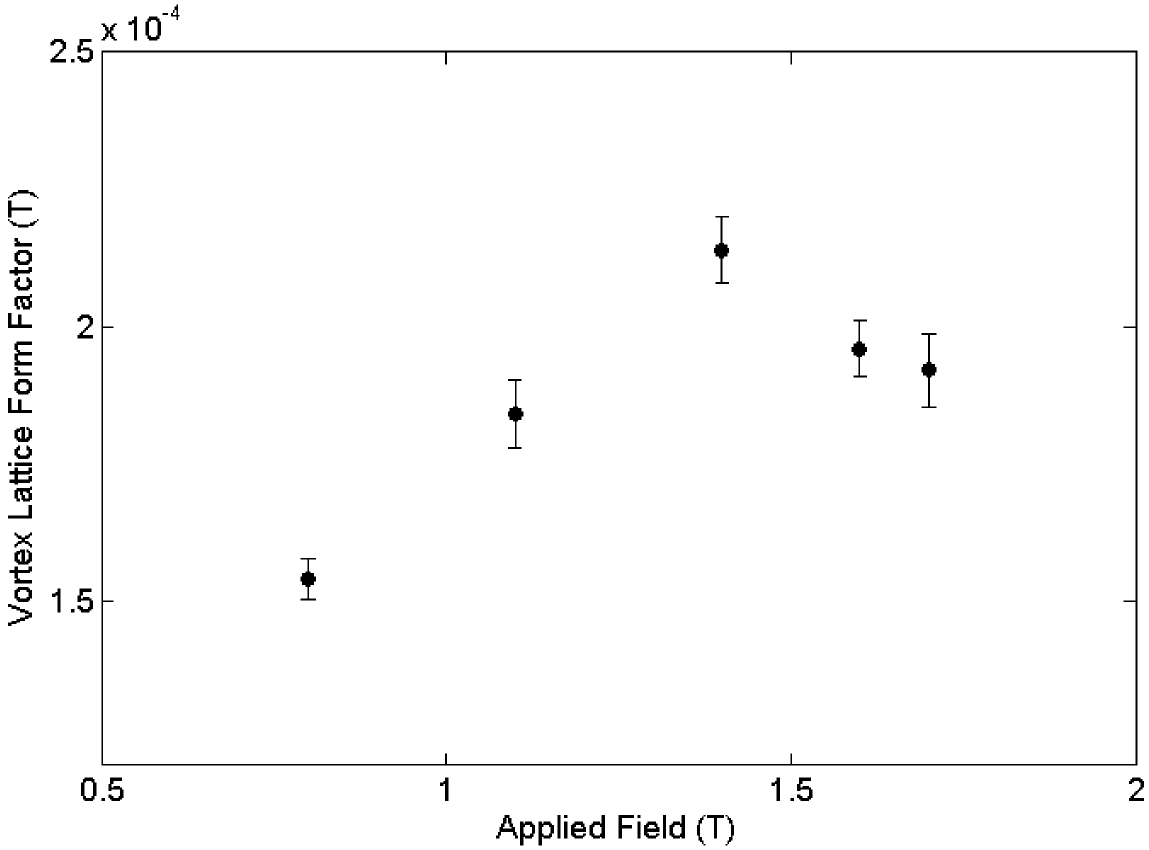

Figure 4.26: The field-dependence of the vortex lattice form factor at 350 mK. The rise in the form factor is still apparent at lower fields, although the cross-over field to a more conventional regime appears to occur at a lower fields compared to the the form factor data at 130 mK.

$\mathrm{CeCoIn_5}$, the vortex lattice form factor is also clearly lower here in the low-field region at higher temperatures. The peak data point for the 130 mK field-dependence data has a vortex lattice form factor value of approximately 0.38 mT (at an applied field of 1.65 T), whereas for the 350 mK data this is approximately 0.21 mT (at an applied field of 1.4 T). The peak vortex lattice form factor is approximately 1.8 times larger at 130 mK compared with 350 mK. However when looking at the 0.8 T data, the 130 mK form factor is approximately 0.22 mT whereas at 350 mK the form factor is approximately 0.15 mT. This is approximately only 1.47 times larger at low temperature. This indicates that the rise of the vortex lattice form factor at low fields is being suppressed with temperature, and increasingly conventional behaviour is being recovered as the temperature is increased.

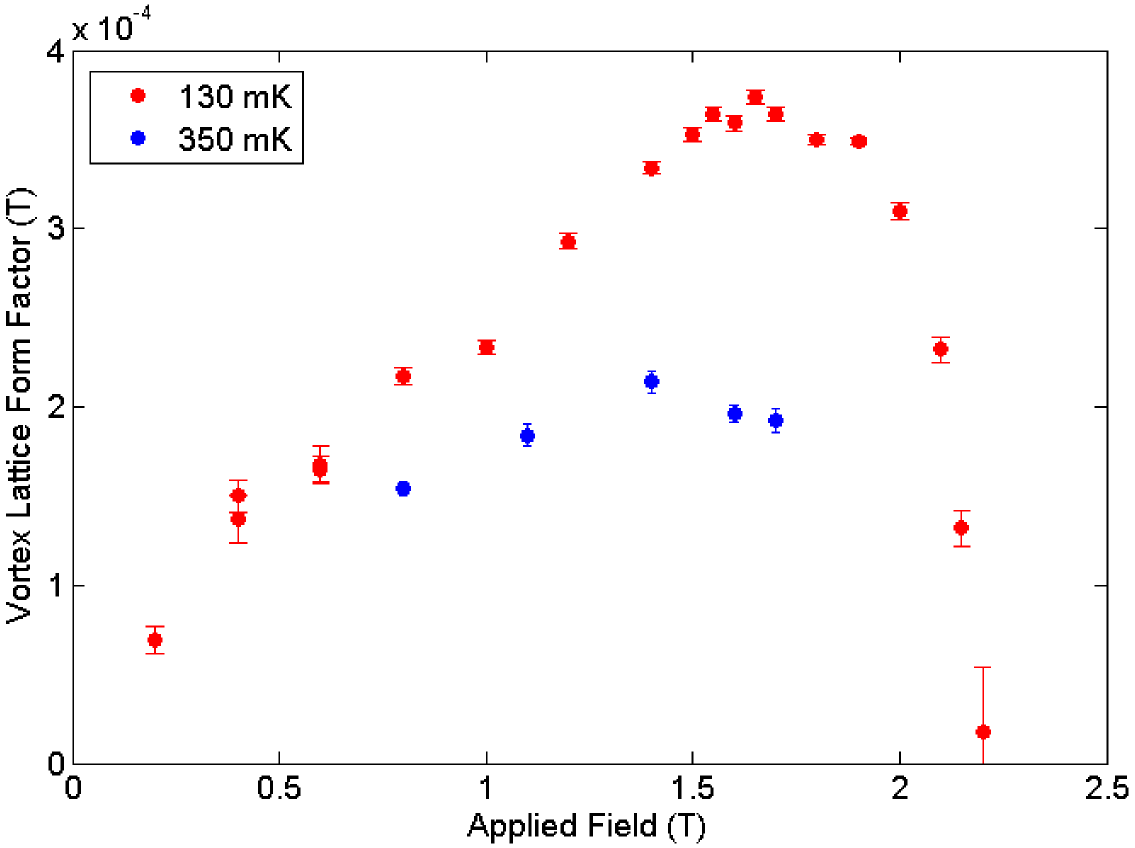

Figure 4.27: Field- and temperature-dependence of the vortex lattice form factor. The low temperature data includes the measurements using both instrumental configurations.

4.6.3 Discussion

Vortex Lattice Structure

Perhaps the most interesting initial observation is that the vortex lattice remains hexagonal throughout the entire field range at both 130 mK and 350 mK. The absence of a structural transition to a rhombic or square phase indicates that $CeCu_2Si_2$ is very unlikely to be a pure *d*-wave superconductor as all studies on *d*-wave superconductors to date have observed a field-induced structural transition of the vortex lattice, such as in the *d*-wave $CeCoIn_5$ where the vortex lattice has several structural transitions.

Shiraishi, Kohmoto and Maki, [82], made use of the extended Ginzburg-Landau theory, which includes the fourth-order derivative term, to study the vortex lattice of a *d*-wave superconductor in a magnetic field parallel to the crystal *c*-axis. They discovered that a long-range fourfold term gives rise to the vortex core interaction which favours the orientation of two vortices parallel to diagonal directions (1, 1, 0) and (1, -1, 0). They found that, in the low field regime, the vortex lattice undergoes a second order transition from triangular to square as the field is increased. An earlier theoretical study by Won and Maki [110] also examined the vortex state of a *d*-wave superconductor in a magnetic field parallel to the *c*-axis. The study found that a square lattice gives the most stable configuration, which was in agreement to SANS results by Keimer *et al.* [52]. From the evidence of these theoretical studies, it is unlikely that $CeCu_2Si_2$ possesses a *d*-wave gap due to the absence of a vortex lattice transition to a square configuration.

The anomalous vortex lattice distortions seen in $CeCu_2Si_2$ have not been observed in other compounds. Huxley *et al.* [92] found that in UPt_3, the vortex lattice realigns itself with the anisotropic superconducting gap as the temperature is increased. However, this is quite different to $CeCu_2Si_2$; firstly UPt_3 has a hexagonal crystal structure and secondly the distortion is temperature-induced. However, in earlier studies of UPt_3 [56, 114], a field-induced distortion was observed although it is was clearly field-dependent rather than anomalous as seen in the $CeCu_2Si_2$ data. In most compounds, distortions in the vortex lattice as a function of field are indicative of an imminent first order vortex lattice structural transition. As this does not occur in $CeCu_2Si_2$, the origin of the anomalous distortions remain unclear. There remains several possibilities as to what may have caused the distortions including that the oscillating field cool method may not have been effective in promoting the vortex lattice to arrange periodically in a way that resembles the actual equilibrium. It would be useful to re-measure the vortex lattice at a single field using various cooling techniques and field oscillations of various magnitudes to check whether the distortions remain. Another possibility is that the sample itself was not uniform, or the field was not applied exactly parallel to the c-axis. It would be useful to measure the angle-dependence of the vortex lattice (i.e. the angle between the c-axis and the field direction) to check whether the sample was simply mounted incorrectly. The experiment done at PSI only measured a single Bragg spot which was at the expected q value within errors, although the errors were larger because of the overall lower statistics of that initial experiment.

Field-induced increase of the vortex lattice form factor

As with $CeCoIn_5$, it seems that the most likely explanation for the enhanced form factor is found within the quasiclassical Eilenberger theory taking paramagnetic effects into account as described in chapter 1 [45, 46]. In figure 1.6(b), the field-dependence of the form factor is shown. In superconductors with weak paramagnetic effects, the square of the form factor decays exponentially as a function of applied field because the variation of the internal magnetic field falls with increasing field (as shown in figure 1.6(a)). However, in the case of strong paramagnetic effects, the form factor increases towards the upper critical field because the variation of the internal magnetic field increases due to the enhanced paramagnetic moment at the vortex core [46]. The strength of the paramagnetic effect is defined by the paramagnetic parameter μ which is defined as

$$\mu = \frac{\mu_B B_0}{\pi k_B T_C} \tag{4.2}$$

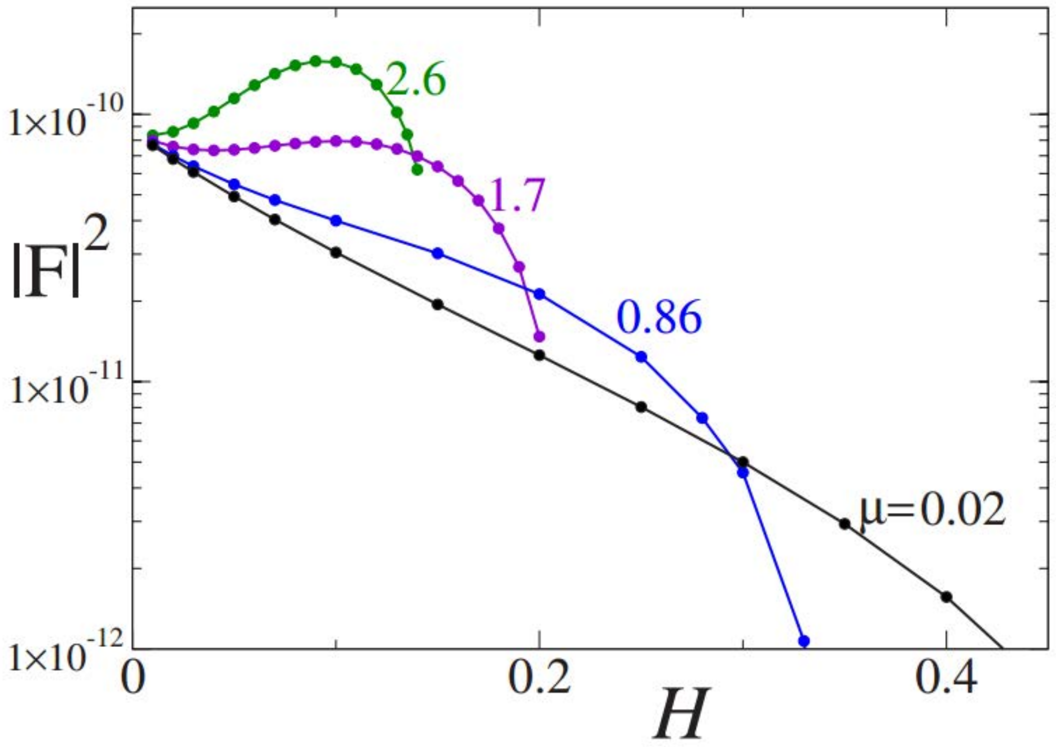

Figure 4.28: Calculated predictions of the field dependence of the vortex lattice form factor for $\mu = 0.02$, 0.86, 1.7, and 2.6 at T $= 0.1T_c$. The vertical axis is in logarithmic scale. Figure reproduced from [46].

where B_0 is a scaling parameter related to B_{C2} referring to the field-scale used by Ichioka *et al*. [45]. Materials with negligible paramagnetic effect ($\mu = 0.02$) decrease with field monotonically. A relatively large μ is required to explain the effects seen in CeCu$_2$Si$_2$, as shown in figure 4.28. The graph indicates that CeCu$_2$Si$_2$ likely has a paramagnetic parameter $\mu > 2.6$ (as shown in figure 4.28.

Other than the paramagnetic parameter μ, there are two other ways of describing the strength of the Pauli-paramagnetic effect. The first is the Maki parameter given by

$$\alpha_M = \sqrt{2}\frac{H_{c2}^{orb}}{H_p} \tag{4.3}$$

where the $H_p = (\Delta_0/\sqrt{2}\mu_B)$ is the Pauli limiting field with order parameter amplitude Δ_0 at T = 0 and H_{C2}^{orb} is the orbital depairing upper critical field. The other measure of paramagnetic effects is α_{para} by Adachi *et al.* [2],

$$\alpha_{para} = \frac{\mu_B H_{C2}^{orb}}{2\pi k_B T_C}. \tag{4.4}$$

The orbital depairing upper critical field $H_{C2}^{orb} = 0.561 B_0$, so dividing α_{para} by the paramagnetic parameter μ gives

$$\frac{\alpha_{para}}{\mu} = \frac{H_{C2}^{orb}}{2B_0} \approx 0.28. \tag{4.5}$$

Substituting the expression for the Maki parameter α_M into the expression for α_{para}, and then re-arranging gives $\alpha_M \approx 7.12\alpha_{para}$ [109]. By combining this with the result from equation 4.5, we can obtain following expression relating the Maki parameter and the paramagnetic parameter,

$$\mu = \frac{\alpha_M}{1.99}. \tag{4.6}$$

This makes it apparent that μ is sensitive to the Pauli limiting field and the orbital depairing upper critical field. According to calculations by Tsutsumi *et al.* [98], the Maki parameter for $CeCu_2Si_2$ is $\alpha_M = 3$. This would imply a value of the paramagnetic parameter of $\mu = 1.5$. Figure 4.28 shows the form factor behaviour for $\mu = 1.7$, this makes it apparent that an increase in the form factor at low fields would be difficult to detect. Therefore $\mu = 1.5$ does not agree with our experimental data. Clogston, [20], estimated the Pauli limiting field to be $H_p = 1.84T_C \approx 1.2$ T for $T_C = 0.65$ K. WHH theory (Werthamer, Helfand and Hohenberg) [100] was used to calculate the orbital upper critical field as $H_{C2}^{orb} = 10.4$ T. This implies a Maki parameter of $\alpha_M = 7.97$, and therefore (from equation 4.6) the paramagnetic parameter $\mu = 4$. This would be in better agreement with our experimental data as the Pauli-paramagnetic effect appears to be stronger than $\mu = 1.5$, or even $\mu = 2.6$ shown figure 4.28 (note that in figure 4.28 the square of the form factor is shown which accentuates the enhancement) when compared with figure 4.25. It is also worth noting that the estimate of the Pauli-limiting field H_p did not account for strong spin-orbit coupling, so whilst the estimated value of $\mu = 4$ is in general agreement with our experimental data, the value should be treated with some degree of caution.

Yamashita *et al.* [112] calculated that the orbital upper critical field in their crystal is 14.7 T for $H \parallel c$. By substituting this value into equation 4.4, and then substituting the value of α_{para} into equation 4.5, we get a paramagnetic parameter of $\mu \approx 8$.

Fall of the vortex lattice form factor as H_{C2} is approached

The field-dependence of the vortex lattice form factor data that has been presented shows that the form factor increases up to a peak value with field before rapidly falling off as the upper critical field is approached. The origin of this fall is of interest to us. In $CeCoIn_5$, the form factor seems to fall almost discontinuously at H_{C2} at the lowest measured temperatures, and this transition becomes increasingly second order at higher temperatures. Our form factor data for $CeCu_2Si_2$ was measured at 130 and 350 mK. 130 mK is approximately $0.2T_C$ for $CeCu_2Si_2$. At $0.2T_C$ for $CeCoIn_5$, the form factor decreases in a similar way to that observed in $CeCu_2Si_2$. Measurements at lower temperatures, ideally as low as $0.1T_C$, should confirm whether or not the second order upper critical field transitions that we observe are temperature-induced.

In $CeCoIn_5$ [9], it was originally believed that the declining form factor could be attributed to an FFLO-type state. However, a later study by White *et al.* [109] of the temperature-dependence of the vortex lattice form factor in $CeCoIn_5$ indicated that the onset of an FFLO-type state seemed unlikely to be the main driving force behind the falling form factor at high fields. The decline of the form factor at high fields appears to be reproducible in the calculations of Ichioka & Machida [45, 46] within the quasiclassical Eilenberger theory without the inclusion of an FFLO state.

The theory [45] indicates that for large μ values, there are two contributions to the overall internal magnetisation; the diamagnetic contributions associated with the screening currents and the field-induced core magnetisation [103]. Figure 4.29 shows that the field-induced core magnetisation dominates the overall magnetisation, but much like the diamagnetic contribution it also begins to fall at the highest fields. This indicates the the fall in the vortex lattice form factor at high fields is related to the fall in the core

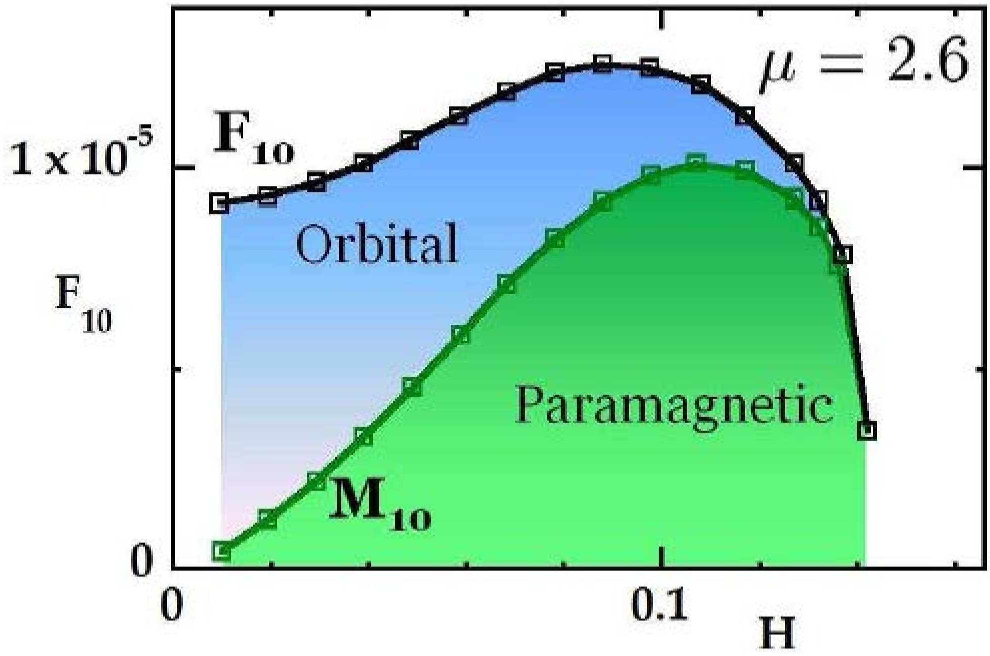

Figure 4.29: The field dependence of the form factor for μ = 2.6, T = $0.1T_c$, and κ = 89. The relative contributions of the field-induced vortex core paramagnetism and the orbital contributions to the entire internal magnetisation are shown. Figure reproduced from [103].

magnetisation at the same field. It it worth noting that the field dependence in figure 4.29 is calculated for a square vortex lattice structure. It is also worth considering the spatial structure of the core magnetisation $M(\mathbf{r})$ as a function of field. Figure 4.30 shows a numerical calculation of this, and it is clear that at higher fields the spatial distribution becomes broader. This is indicative of overlapping paramagnetic vortices as they expand. Therefore, similar to the explanation for same phenomenon in CeCoIn$_5$ by White *et al.* [103, 109], the fall of the vortex lattice form factor as the upper critical field H_{C2} is approached is likely due to the decreased spatial confinement of the core magnetisation at high fields.

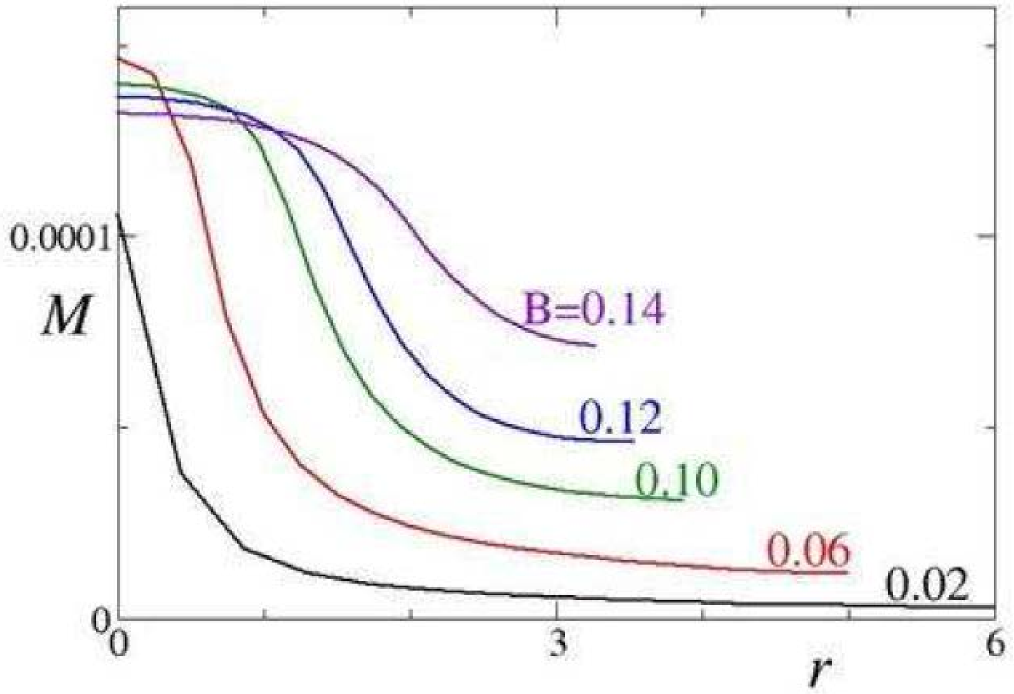

Figure 4.30: Numerical calculations of the field dependence of the spatial distribution of the core induced paramagnetic moment. The calculation considers the same case as figure 4.29. Figure reproduced from [103].

4.7 Conclusions and Outlook

By studying the vortex lattice in $CeCu_2Si_2$ we have established, from the lack of a structural transition, that the superconducting order parameter is unlikely to be purely *d*-wave. From measurements of the vortex lattice form factor we have confirmed that the vortex cores do have a strong paramagnetic effect which is exhibited in the field-dependence of the form factor whereby the paramagnetism in the vortex cores provides additional contrast with increasing field in the low-field region. The form factor behaviour seems to match well to a value of the paramagnetic parameter $\mu = 4$ which was calculated previously. Other values of μ (= 1.5 and 8) do not seem suitable for our data. The value of $\mu =$ 4 neglected spin orbit effects. White *et al*. [102] claims that it is likely that $H_{C2} > H_p$ due to strong spin orbit scattering in $CeCu_2Si_2$, so the value of the paramagnetic effect which is derived from a value of H_p by Clogston [20] can justifiably be treated with a certain degree of scepticism. Figure 4.31 shows the vortex lattice form factor of $CeCu_2Si_2$ plotted

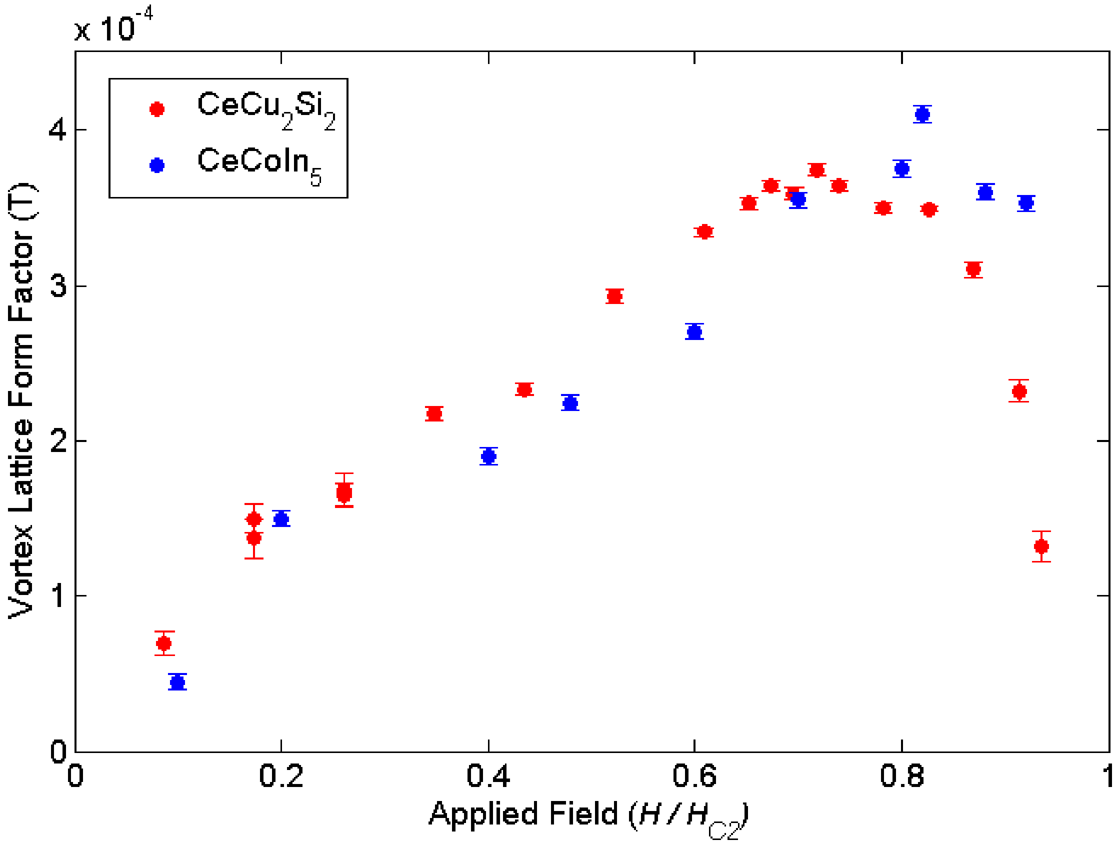

Figure 4.31: The field-dependence of the vortex lattice form factor for both $CeCu_2Si_2$ (130mK) and $CeCoIn_5$ (500 mK). Both are measured at approximatelt $0.2T_C$. The $CeCoIn_5$ data is from [9].

against the form factor of $CeCoIn_5$. This shows how remarkably similar the behaviour is in these two different heavy fermion compounds. However, there is no reason to expect the form factor to be identical in these two compounds, so the similarity in the vortex lattice form factor values is more likely to be coincidental than of any physical significance. The $CeCu_2Si_2$ measurements were taken at 130 mK, and the $CeCoIn_5$ measurements were taken at 500 mK (reproduced from [9]). This makes the data comparable as they were both measured at approximately $0.2T_C$.

The fall of the form factor as H_{C2} is approached is attributed to the spatial confinement of the core magnetisation at high fields, as is thought to be the case in $CeCoIn_5$. It appears that the upper critical field transition becomes increasingly second order as the temperature is increased in $CeCu_2Si_2$. This indicates a first order transition may occur if

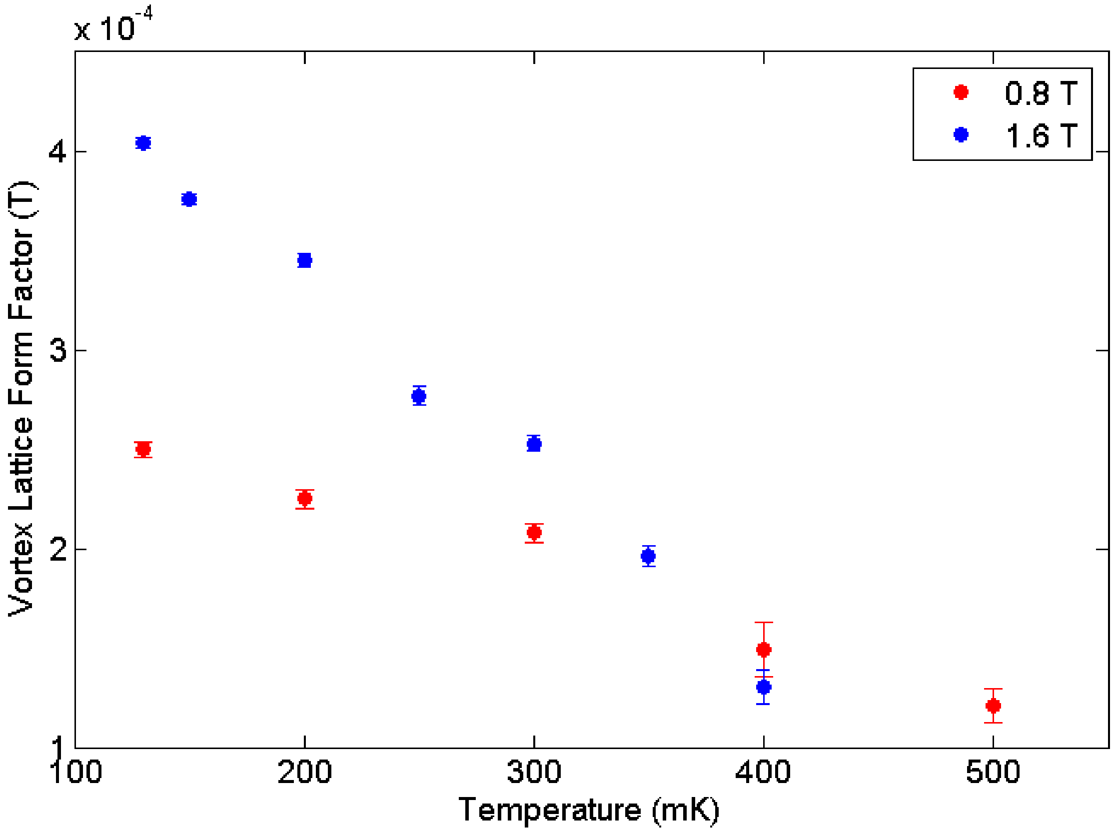

Figure 4.32: The vortex lattice form factor as a function of temperature at 1.6 T and 0.8 T. The linear decrease with temperature indicates nodal behaviour, however measurements at even lower temperature are required to confirm this.

the vortex lattice is studied at a suitably small fraction of T_C. The upper critical field can remain a second order transition in multiband superconductors, however if a first order transition is observed at low temperatures in $CeCu_2Si_2$ this would be indicative of single band superconductivity [98].

Preliminary measurements of the temperature dependence of the vortex lattice form factor have been done down to $0.2T_C$. These were measured at 0.8 T and 1.6 T as shown in figure 4.32. The preliminary measurements shows a linear decrease of the vortex lattice form factor with increasing temperature. If this dependence remains linear down to $0.1T_C$, it would be indicative of nodal behaviour. Further measurements are scheduled to be undertaken down to approximately $0.1T_C$ across the entire field range at PSI.

Chapter 5

Conclusions

To summarise the work in this thesis, we have studied the vortex lattice in two superconductors; the cuprate $YBa_2Cu_3O_7$ and the heavy fermion $CeCu_2Si_2$. We presented evidence for the existence of Pauli-paramagnetic effects in both systems.

In YBCO, we observed the vortex lattice behaviour at higher fields than ever before. Our results for YBCO show that high fields destroy superconducting pairing in the carriers traveling along the crystal b direction (CuO chains). This leads to a field-dependent change in the superconducting anisotropy, which is reflected in a change in the angular position of the order-parameter nodes in this orthorhombic $(d+s)$-wave material. We also observed the lack of falloff of the intensity of the diffraction signal from the vortex lattice at high fields which we interpret as the signature of Pauli-paramagnetic vortex cores.

In $CeCu_2Si_2$, we found that due to the lack of a structural transition in the vortex lattice, the superconducting order parameter is unlikely to be purely d-wave. The field dependence of the vortex lattice form factor provided evidence that the vortex cores have a strong paramagnetic effect. Unlike in YBCO, the upper critical field is easily accessible at low temperatures in $CeCu_2Si_2$. The rapid decrease of the vortex lattice form factor as H_{C2} is approached is attributed to the spatial confinement of the core magnetisation at high fields. It appears that the upper critical field transition becomes increasingly second order at higher temperatures which is may be indicative of a first order transition occurring if the vortex lattice is studied at a sufficiently small fraction of T_C ($\approx 0.1 T_C$).

It is worth considering why our evidence for Pauli-paramagnetic cores does not manifest itself in same way in YBCO as it does in $\mathrm{CeCu_2Si_2}$. In YBCO, the vortex lattice form factor behaviour closely resembles that of $\mathrm{TmNi_2B_2C}$ whereas $\mathrm{CeCu_2Si_2}$ is far more like $\mathrm{CeCoIn_5}$. The paramagnetic effect is weaker in YBCO than $\mathrm{CeCu_2Si_2}$, and this is clear from their respective field-dependences of the vortex lattice form factor. The form factor in YBCO deviates from the usual exponential behaviour, however, unlike $\mathrm{CeCu_2Si_2}$, it does not actually increase with field. Instead the form factor just falls more slowly and linearly with fields up to 25 T (still a small fraction of H_{C2}). This behaviour is also observed in $\mathrm{TmNi_2B_2C}$ whereby the vortex lattice is approximately constant up to $0.6H_{C2}$. The borocarbides (the family to which $\mathrm{TmNi_2B_2C}$ belongs), similarly to YBCO, also have a layered structure. Apart from this, the two compounds are quite dissimilar – YBCO is also much more strongly type-II with a κ approximately an order of magnitude larger than in most borocarbide superconductors. In $\mathrm{CeCu_2Si_2}$, the field-dependence of the form factor resembles that observed in $\mathrm{CeCoIn_5}$. Both of these heavy fermion compounds have a stronger paramagnetic effect than $\mathrm{TmNi_2B_2C}$ and YBCO. One commonality between these compounds is that they both contain cerium. However, it is still unclear what is the definitive driving force behind differences in the paramagnetic effects in these systems. What we have established is that the paramagnetic effects play a major role in fully understanding the vortex lattice behaviour in YBCO and $\mathrm{CeCu_2Si_2}$.

Chapter 6

Other Work and Publications

Other materials studied

This thesis focuses on two projects undertaken within the duration of my PhD; the high field study of the vortex lattice in detwinned $YBa_2Cu_3O_7$ and the vortex lattice in $CeCu_2Si_2$. However, a considerable amount of time since September 2013 was also spent studying other superconducting and magnetic materials. I was involved in studying the vortex lattice in several other superconductors including:

- Ca-doped YBCO: The inclusion of calcium on yttrium sites increases the hole concentrations in the CuO_2 planes beyond that found in $YBa_2Cu_3O_7$, so the material is overdoped.
- $YBa_2Cu_4O_8$: Exhibits two CuO chains per unit cell compared to one in the structurally related $YBa_2Cu_3O_{7-\delta}$ compounds.
- $YBa_2Cu_3O_{0.45}$: The concentration of the doped holes in the CuO_2 layers is controlled by the oxygen content in the CuO chains, so this is an underdoped sample.
- Twinned $YBa_2Cu_3O_7$: A brief study of twinned YBCO as opposed to the detwinned YBCO described in this thesis.
- KFe_2As_2: Pnictide compound to elucidate the nature of the superconductivity in this compound.
- $(Ba_{0.5}K_{0.5})Fe_2As_2$: Similar to KFe_2As_2, but with barium doped at the potassium sites. This increased the superconducting transition temperature and the upper critical

field.

- BiPd: A non-centrosymmetric superconductor.
- $TlNi_2Se_2$: A heavy fermion superconductor with structural similarities to the FeAs superconductors.

I also studied (unsuccessfully) the possibility of valence transitions in the heavy fermion superconductor $YbAlB_4$ via an X-ray diffraction at the XMaS beamline at the ESRF, and (successfully) participated in the investigation of the magnetic phases in the pyrochlore Y_2CrSbO_7 via neutron diffraction experiments at the ILL.

Publications arising from work in this thesis

A. S. Cameron, J. S. White, A. T. Holmes, E. Blackburn, E. M. Forgan, **R. Riyat**, T. Loew, C. D. Dewhurst, A. Erb. "High Magnetic Field study of the Vortex Lattice Structure in $YBa_2Cu_3O_7$" Physical Review B. **90**, 054502 (2014).

R. Riyat, E. Blackburn, E. M. Forgan, A. S. Cameron, A. T. Holmes, O. Prokhnenko, M. Bartkowiak, W.-D. Stein, A. Erb. "Field-dependent superconducting anisotropy and Pauli paramagnetism in $YBa_2Cu_3O_7$" (In preparation).

A. S. Cameron, **R. Riyat**, A. T. Holmes, E. Blackburn, E. M. Forgan, C. D. Dewhurst, R. Cubitt, A. Erb. "High Field Study of the Vortex Lattice in Ca-doped YBCO" (In preparation).

R. Riyat, E. Blackburn, E. M. Forgan *et al.*, "Pauli-limited superconductivity in the heavy-fermion $CeCu_2Si_2$" (In preparation).

Other publications arising during this thesis

S. J, Kuhn, H. Kawano-Furukawa, E. Jellyman, **R. Riyat**, E. M. Forgan, M. Ono, K. Kihou, C. H. Lee, F. Hardy, P. Adelmann, Th. Wolf, C. Meingast, J. Gavilano, M. R. Eskildsen. "Simultaneous evidence for Pauli paramagnetic effects and multiband superconductivity in KFe_2As_2 by small-angle neutron scattering studies of the vortex lattice" Physical Review B, **93**, 104527 (2016).

L. Shen, C. Greaves, **R. Riyat**, T. C. Hansen, E. Blackburn. "Absence of magnetic long range order in Y_2CrSbO_7: bond-disorder induced magnetic frustration in a ferromagnetic pyrochlore" Physical Review B, **96**, 094438 (2017).

E. Jellyman, **R. Riyat**, E. Blackburn, E. M. Forgan *et al.* "The vortex lattice in $TlNi_2Se_2$" (In preparation).

E. Jellyman, H. Kawano-Furukawa, **R. Riyat**, E. Blackburn, E. M. Forgan *et al.* "The vortex lattice in $(Ba_{0.5}K_{0.5})Fe_2As_2$" (In preparation).

List of References

[1] A. A. Abrikosov. *Sov. Phys. JETP*, 5:1174, 1957.

[2] H. Adachi, M. Ichioka, and K. Machida. *J. Phys. Soc. Jpn.*, 74:2192, 2005.

[3] A. Aperis, G. Varelogiannis, and P. B. Littlewood. *Phys. Rev. Lett.*, 104:216403, 2010.

[4] A. Aperis, G. Varelogiannis, P. B. Littlewood, and B. D. Simons. *J. Phys.: Condens. Matter*, 20:434235, 2008.

[5] O. Arnold *et al. Nuclear Instruments and Methods in Physics Research A.*, 764:156–66, 2014.

[6] W. Baltensperger and V. Strassler. *Phys. Kondens. Mater*, 2:20, 1962.

[7] D. N. Basov and T. Timusk. *Rev. Mod. Phys.*, 77:721, 2005.

[8] K.A. Bednorz, J.G. & Mller. *Z. Physik B - Condensed Matter*, 64:189, 1986.

[9] A. D. Bianchi, M. Kenzelmann, L. DeBeer-Schmitt, J. S. White, E. M. Forgan, J. Mesot, M. Zolliker, J. Kohlbrecher, R. Movshovich, E. D. Bauer, J. L. Sarrao, Z. Fisk, C. Petrovic, and M. R. Eskildsen. *Science*, 319:177, 2008.

[10] G. Blatter, J. Rhyner, and V. M. Vinokur. *Phys. Rev. B.*, 43:7826, 1991.

[11] S. Blundell. Oxford University Press, 1st edition, 2001.

[12] S. P. Brown, D. Charalambous, E. C. Jones, E. M. Forgan, P. G. Kealey, A. Erb, and J. Kohlbrecher. *Phys. Rev. Lett.*, 92:067004, 2004.

[13] A. S. Cameron. PhD thesis, University of Birmingham, 2014.

[14] A. S. Cameron, R. Riyat, E. Blackburn, E. M. Forgan, C. D. Dewhurst, Cubitt. R., and A. Erb. *In preparation.*

[15] A. S. Cameron, J. S. White, A. T. Holmes, E. Blackburn, E. M. Forgan, R. Riyat, T. Loew, C. D. Dewhurst, and A. Erb. *Phys. Rev. B*, 90:054502, 2014.

[16] C. Caroli, P. G. De Gennes, and J. Matricon. *Phys. Lett.*, 9:307, 1964.

[17] A. Cavelleri *et al.* *Max Planck Institute for the Structure and Dynamics of Matter*, Accessed on 05 September 2017:http://qcmd.mpsd.mpg.de/index.php/research/research–science/Light–induced–SC–like–properties–in–cuprates.html, 2008-2017.

[18] R. Chevrel and M. Sergent. *Berlin: Springer*, pages 25–86, 1982.

[19] D. K. Christen, F. Tasset, S. Spooner, and H. A. Mook. *Phys. Rev. B*, 15:4506, 1977.

[20] A. M. Clogston. *Phys. Rev. Lett.*, 9:266, 1962.

[21] L. DeBeer-Schmitt, M. R. Eskildsen, M. Ichioka, K. Machida, N. Jenkins, C. D. Dewhurst, A. B. Abrahamsen, S. L. Bud'ko, and P. C. Canfield. *Phys. Rev. Lett.*, 99:167001, 2007.

[22] C. D. Dewhurst. *http://www.ill.eu/ instruments -support /instruments-groups /groups /lss /grasp /home/.*

[23] G. J. Dolan *et al.* *Phys. Rev. Lett.*, 62:827, 1989.

[24] G. J. Dolan *et al.* *Phys. Rev. Lett.*, 62:2184, 1989.

[25] N. A. Egetenmeyer. *PhD Thesis, ETH Zurich*, 2013.

[26] G. Eilenberger. *Z. Phys.*, 214:195, 1968.

[27] M. Enayat *et al.* *Phys. Rev. B.*, 93:045123, 2007.

[28] A. Erb, A. A. Manuel, M. Dhalle, F. Marti, J. Y. Genoud, B. Revaz, A. Junod, D. Vasumathi, S. Ishibashi, A. Shukla, E. Walker, Ø. Fischer, R. Flükiger, R. Pozzi, M. Mali, and D. Brinkmann. *Solid State Commun.*, 112:245, 1999.

[29] A. Erb, E. Walker, and R. Flükiger. *Physica (Amsterdam)*, 258C:9, 1996.

[30] I. Erimin *et al.* *Phys. Rev. Lett.*, 101:187001, 2008.

[31] M. R. Eskildsen. *PhD Thesis, Riso National Laboratory*, 1998.

[32] M. R. Eskildsen, E. M. Forgan, and H. Kawano-Furukawa. *Reports on Progress in Physics*, 74:124504, 2011.

[33] E. M. Forgan and S. L. Lee. *Phys. Rev. Lett.*, 75:1422, 1995.

[34] E. M. Forgan, D. McK. Paul, H. A. Mook, P. A. Timmins, H. Keller, S. Sutton, and J. S. Abell. *Nature (London)*, 343:735, 1990.

[35] E. Fradkin and S. A. Kivelson. *Nature Physics*, 8:864, 2012.

[36] P. Fulde and R. A. Ferrell. *Phys. Rev.*, 135:A550, 1964.

[37] P. L. Gammel, D. J. Bishop, G. J. Dolan, J. R. Kwo, C. A. Murray, L. F. Schneemeyer, and J. V. Waszczak. *Phys. Rev. Lett.*, 59:2592, 1987.

[38] P. Geganwart, C. Langhammer, C. Geibel, R. Helfrich, M. Lang, G. Sparn, F. Steglich, R. Horn, L. Donnevert, A. Link, and A. Assmus. *Phys. Rev. Lett.*, 81(7):1501, 1998.

[39] G. Goll. *Unconventional Superconductors: Experimental Investigation of the Order Parameter Symmetry, Springer*, 2006.

[40] V. Hinkov, P. Bourges, S. Pailhès, Y. Sidis, A. Ivanov, C. D. Frost, T. G. Perring, C. T. Lin, D. P. Chen, and B. Keimer. *Nature Phys.*, 3:780, 2007.

[41] A. T. Holmes. *Phys. Rev. B.*, 90:024514, 2014.

[42] A. T. Holmes, G. R. Walsh, E. Blackburn, E. M. Forgan, and M. Savey-Bennett. *Rev. Sci. Inst.*, 83:023904, 2012.

[43] A. D. Huxley. *Physica C*, 514:368–77, 2015.

[44] M. Ichioka, A. Hasegawa, and K. Machida. *Phys. Rev. B*, 59:8902, 1999.

[45] M. Ichioka and K. Machida. *Phys. Rev. B*, 76:064502, 2007.

[46] M. Ichioka and K. Machida. *Journal of Physics: Conference Series*, 150:052074, 2009.

[47] H. Ikeda, M. T. Suzuki, and R. Arita. *Phys. Rev. Lett.*, 114:147003, 2015.

[48] R. Ikeda, Y. Hatakeyama, and K. Aoyama. *Phys. Rev. B*, 82:060510, 2010.

[49] K. Izawa *et al.* *Phys. Rev. Lett.*, 87:057002, 2001.

[50] S. T. Johnson, E. M. Forgan, S. H. Lloyd, C. M. Aegerter, S. L. Lee, R. Cubitt, P. G. Kealey, C. Ager, S. Tajima, A. Rykov, and D. McK. Paul. *Phys. Rev. Lett.*, 82:2792, 1999.

[51] B. Keimer, F. Doğan, I. A. Aksay, R. W. Erwin, J. W. Lynn, and M. Sarikaya. *Science*, 83:262, 1993.

[52] B. Keimer, W. Y. Shih, R. W. Erwin, J. W. Lynn, F. Dogan, and I. A. Aksay. *Phys. Rev. Lett.*, 73:3459, 1994.

[53] M. Kenzelmann. *Rep. Prog. Phys.*, 80:034501, 2017.

[54] J. R. Kirtley *et al.* *Nature (Physics)*, 2:190, 2006.

[55] A. Kittaka *et al.* *Phys. Rev. Lett.*, 112:067002, 2014.

[56] R. N. Kleiman *et al.* *Phys. Rev. Lett.*, 69:3120, 1992.

[57] V. G. Kogan. *Phys. Rev. B*, 24:1572, 1981.

[58] V. G. Kogan, M. Bullock, B. Harmon, P. Miranović, Lj. Dobrosavljević-Grujić, P. L. Gammel, and D. J. Bishop. *Phys. Rev. B*, 55:R8693, 1997.

[59] V. G. Kogan, A. Gurevich, J. H. Cho, D. C. Johnston, Ming Xu, J. R. Thompson, and A. Martynovich. *Phys. Rev. B*, 54:12386, 1996.

[60] V. G. Kogan, P. Miranović, Lj. Dobrosavljević-Grujić, W. E. Pickett, and D. K. Christen. *Phys. Rev. Lett.*, 79:741, 1997.

[61] S. J. Kuhn, H. Kawano-Furukawa, E. Jellyman, R. Riyat, E. M. Forgan, M. Ono, K. Kihou, C. H. Lee, F. Hardy, P. Adelmann, Th. Wolf, C. Meingast, J. Gavilano, and M. R. Eskildsen. *Phys. Rev. B.*, 93:10452, 2016.

[62] A. I. Larkin and Y. N. Ovchinnikov. *Sov. Phys. JETP-USSR*, 20:762, 1965.

[63] A. G. Lebed. *Phys. Rev. Lett.*, 96:037002, 2006.

[64] P. Li, F. F. Balakirev, and R. L. Greene. *Phys. Rev. B*, 75:172508, 2007.

[65] C. T. Lin, W. Zhou, W. Y. Liang, E. Schönherr, and H. Bender. *Physica C*, 195:291, 1991.

[66] F. London and H. London. *Proc. Roy. Soc. Lond. A*, 149:7188, 1935.

[67] Y. Matsuda and H. Shimihara. *J. Phys. Soc. Japan*, 76:051005, 2007.

[68] W. Meissner and R. Ochsenfeld. *Naturwissenschaften*, 21:787, 1933.

[69] V. P. Michal and V. P. Mineev. *Phys. Rev. B.*, 84:052508, 2011.

[70] R. Movshovich *et al. Phys. Rev. Lett.*, 86:5152–5, 2001.

[71] H. K. Onnes. *Comm. Phys. Lab. Univ. Leiden*, 122 and 124:–, 1911.

[72] G. M. Pang *et al. arXiv.*, 1605:04786v1, 2016.

[73] A. Pautrat, A. Brulet, C. Simon, and P. Mathieu. *Phys. Rev. B*, 85:184504, 2012.

[74] C. Pfleiderer *et al.* *Rev. Mod. Phys.*, 81:1551, 2009.

[75] O. Prokhnenko, W-D. Stein, H-J. Bleif, M. Fromme, M. Bartkowiak, and T. Wilpert. *Rev. Sci. Instrum.*, 86:033102, 2015.

[76] G. C. Psaltakis and E. W. Fenton. *J. Phys. C: Solid State Phys.*, 16:3913–32, 1983.

[77] R. Riyat, E. Blackburn, E. M. Forgan, A. S. Cameron, A. T. Holmes, O. Prokhnenko, M. Bartkowiak, W. D. Stein, and A. Erb. *In Preparation*, 2017.

[78] S. Seiro, M. Deppe, H. Jeevan, U. Burkhardt, and C. Geibel. *Phys. Status Solidi*, 247:614–616, 2010.

[79] T. Sekitani, N. Miura, S. Ikeda, Y. H. Matsuda, and Y. Shiohara. *Physica B*, 346-7:319–24, 2004.

[80] T. P. Sheahen. Plenum Press, New York and London, 1994.

[81] H. Shimihara. *J. Phys. Soc. Japan*, 69:1966, 2000.

[82] J. Shiraishi, M. Kohmoto, and K. Maki. *Phys. Rev. B*, 59(6):4497–4503, Feb 1999.

[83] Ch. Simon, A. Pautrat, G. Poullain, C. Goupil, C. Leblond-Harnois, X. Chaud, and A. Brûlet. *Phys. Rev. B*, 70:024502, 2004.

[84] G. L. Squires. Dover, 2nd edition, 1978.

[85] F. Steglich, J. Aarts, C. D. Bredl, W. Lieke, D. Meschede, W. Franz, and H. Schfer. *Phys. Rev. Lett.*, 43:1892, 1979.

[86] C. Stock *et al.* *Phys. Rev. Lett.*, 100:087001, 2008.

[87] O. Stockert, E. Faulhaber, G. Zwicknagl, N. Stuber, H. S. Jeevan, M. Deppe, R. Borth, R. Kuchler, M. Loewenhaupt, C. Geibel, and F. Steglich. *Phys. Rev. Lett.*, 92(13):136401, 2004.

[88] O. Stockert *et al.* *Nature Physics*, 7:119, 2011.

[89] K. M. Suzuki, M. Ichioka, and K. Machida. *Phys. Rev. B.*, 83:140503, 2011.

[90] M. Tachiki *et al.* *Z. Phys. B.*, 100:369, 1996.

[91] An. K. Sakakibara *et al.* *Phys. Rev. Lett.*, 104:037002, 2010.

[92] Andrew Huxley *et al.* *Nature*, 406:160, 2000.

[93] H. A. Vieyra *et al.* *Phys. Rev. Lett.*, 106:207001, 2011.

[94] J-R. Wang *et al.* *Phys. Rev. B.*, 94:014501, 2016.

[95] S. I. Vedeneev *et al.* *Phys. Rev. B.*, 73:014528, 2006.

[96] Smeibidl *et al.* *IEEE Transactions on Applied Superconductivity*, 26:4301606, 2016.

[97] M. Tinkham. McGraw-Hill, New York, 1996.

[98] Y. Tsutsumi, K. Machida, and M. Ichioka. *Phys. Rev. B.*, 92:020502, 2015.

[99] B. O. Wells *et al.* *Phys. Rev.*, B46:11830, 1992.

[100] N.R. Werthamer, E. Helfand, and P.C. Hohenberg. *Phys. Rev.*, 147:295, 1966.

[101] B. D. White, J. D. Thompson, and M. B. Maple. *Physica C*, 514:279–89, 2015.

[102] B. D. White, J. D. Thompson, and M. B. Maple. *Physica C*, 514:246–278, 2015.

[103] J. S. White. *PhD Thesis. University of Birmingham*, 2009.

[104] J. S. White, S. P. Brown, E. M. Forgan, M. Laver, C. J. Bowell, R. J. Lycett, D. Charalambous, V. Hinkov, A. Erb, and J. Kohlbrecher. *Phys. Rev. B*, 78:174513, 2008.

[105] J. S. White, P. Das, M. R. Eskildsen, L. DeBeer-Schmitt, E. M. Forgan, A. D. Bianchi, M. Kenzelmann, M. Zolliker, S. Gerber, J. L. Gavilano, J. Mesot, R. Movshovich, E. D. Bauer, J. L. Sarrao, and C. Petrovic. *New J. Phys.*, 12:023026, 2010.

[106] J. S. White, R. W. Heslop, A. T. Holmes, E. M. Forgan, V. Hinkov, N. Egetenmeyer, J. L. Gavilano, M. Laver, C. D. Dewhurst, R. Cubitt, and A. Erb. *Phys. Rev. B*, 84:104519, 2011.

[107] J. S. White, V. Hinkov, R. W. Heslop, R. J. Lycett, E. M. Forgan, C. Bowell, S. Strässle, A. B. Abrahamsen, M. Laver, C. D. Dewhurst, J. Kohlbrecher, J. L. Gavilano, J. Mesot, B. Keimer, and A. Erb. *Phys. Rev. Lett.*, 102:097001, 2009.

[108] J. S. White, V. Hinkov, R. W. Heslop, R. J. Lycett, E. M. Forgan, C. Bowell, S. Strässle, A. B. Abrahamsen, M. Laver, C. D. Dewhurst, J. Kohlbrecher, J. L. Gavilano, J. Mesot, B. Keimer, and A. Erb. *Phys. Rev. Lett.*, 102(9):097001, Mar 2009.

[109] J. S. White *et al.* *New. J. Phys.*, 12:023026, 2009.

[110] H. Won and K. Maki. *Phys. Rev. B*, 53:5927, 1996.

[111] M. K. Wu *et al.* *Phys. Rev. Lett.*, 58(9):908–910, 1987.

[112] T. Yamashita *et al.* *ArXiv*, 1703:02800, 2017.

[113] K. Yano *et al.* *Phys. Rev. Lett.*, 99:167001, 2008.

[114] U. Yaron *et al.* *Phys. Rev. Lett.*, 78:3185, 1997.

[115] M. Yethiraj, H. A. Mook, G. D. Wignall, R. Cubitt, E. M. Forgan, S. L. Lee, D. M. Paul, and T. Armstrong. *Phys. Rev. Lett.*, 71:3019, 1993.

[116] M. Yethiraj, H. A. Mook, G. D. Wignall, R. Cubitt, E. M. Forgan, D. M. Paul, and T. Armstrong. *Phys. Rev. Lett.*, 70:857, 1993.